

From the atom to the material: The micromechanical model to convert atomic information to macroscopic phenomena

Joachim Vandewalle

Student number: 01702776

Supervisors: Dr. ir. Sven Rogge, Prof. dr. ir. Veronique Van Speybroeck

Counsellor: Ir. Juul De Vos

Master's dissertation submitted in order to obtain the academic degree of
Master of Science in Engineering Physics

Academic year 2021-2022



This work has been performed at the Center for Molecular Modeling.

Preface

Throughout my journey to becoming an engineer, my thesis work and the past year in general have been a highlight. I could never have learned so much, however, without the support of a few people, to whom I would like to offer my sincere gratitude: Juul De Vos, who acted as a counsellor, professor Veronique Van Speybroeck, who acted as a supervisor, and Sven Rogge, who took on a double role as a supervisor and a counsellor. Thank you, Juul, for your constructive feedback and for your technical support during the first few months of the academic year. I hope you're having a wonderful time with your family. Thank you, professor Van Speybroeck, for sharing your insight and your knowledge, for keeping all of us focused on the big picture and for offering your help in finding my career path. Thank you, Sven, for spotting and knowing how to fix so many mistakes in this text and for elucidating so many conceptual mysteries. I hope you are still as excited as I am about this brainchild of yours, the micromechanical model, and I hope this work proves to be useful in your research.

I would also like to thank everyone who has supported me in some non-academic way, including my fellow thesis students, for being good company, my roommate, for cooking many delicious meals, my family, for providing a calm oasis of homely comfort, and my friends, for being there when I needed you most. Lastly, to anyone reading this thesis, who I might not know personally: thank you for showing an interest in my work.

– Joachim

Copyright agreement

The author gives permission to make this master's dissertation available for consultation and to copy parts of this master's dissertation for personal use. In the case of any other use, the copyright terms have to be respected, in particular with regard to the obligation to state expressly the source when quoting results from this master's dissertation.

-July 3, 2022

A handwritten signature in black ink, appearing to read "Joachim J." or "J. Vandewalle".

Joachim Vandewalle

From the atom to the material: The micromechanical model to convert atomic information to macroscopic phenomena

by Joachim Vandewalle

Supervisors: dr. ir. Sven M. J. Rogge and prof. dr. ir. Veronique Van Speybroeck

Counsellor: ir. Juul S. De Vos

Master's dissertation submitted in order to obtain the academic degree of
MASTER OF SCIENCE IN ENGINEERING PHYSICS

Department of Applied Physics

Chair: prof. dr. ir. Christophe Leys

Faculty of Engineering and Architecture

Ghent University

Academic year 2021–2022

Overview

This work investigates the micromechanical model as a computationally efficient, coarse-grained approach to simulate the mechanical behaviour of metal-organic frameworks (MOFs). The methodology of the micromechanical model was implemented and validated first on a test system with simple and predictable properties. The potential energy and the analytical equations of motion of the micromechanical model were modified to account for non-periodic boundary conditions and checked for consistency. Using the test system, successful molecular dynamics (MD) simulations were performed in the (N, V, E) , (N, V, T) and (N, P, T) ensembles. Additionally, the micromechanical model was used in a case study of correlated defects in UiO-66. A number of micromechanical systems were constructed to represent different configurations of correlated defects, including line defects and planar defects. The mechanical behaviour of these configurations, captured by both static and dynamic elastic constants, was observed to vary predictably as a function of defect concentration and correlation.

Keywords

molecular modelling, coarse graining, metal-organic frameworks, elasticity

From the atom to the material: The micromechanical model to convert atomic information to macroscopic phenomena

Joachim Vandewalle

Supervisors: dr. ir. Sven M. J. Rogge, prof. dr. ir. Veronique Van Speybroeck

Counsellor: ir. Juul S. De Vos

Abstract—This work investigates the micromechanical model as a computationally efficient, coarse-grained approach to simulate the mechanical behaviour of metal-organic frameworks (MOFs). The methodology of the micromechanical model was implemented and validated first on a test system with simple and predictable properties. The potential energy and the analytical equations of motion of the micromechanical model were modified to account for non-periodic boundary conditions and checked for consistency. Using the test system, successful molecular dynamics (MD) simulations were performed in the (N, V, E) , (N, V, T) and (N, P, T) ensembles. Additionally, the micromechanical model was used in a case study of correlated defects in UiO-66. A number of micromechanical systems were constructed to represent different configurations of correlated defects, including line defects and planar defects. The mechanical behaviour of these configurations, captured by both static and dynamic elastic constants, was observed to vary predictably as a function of defect concentration and correlation.

Index Terms—molecular modelling, coarse graining, metal-organic frameworks, elasticity

I. INTRODUCTION

FOR THE PAST THREE DECADES, metal-organic frameworks (MOFs) have been an exceedingly important topic in materials research. A MOF is a nanoporous, often crystalline material, composed of metal ions or inorganic clusters connected by organic linkers. MOFs have grown to be an extensive class of materials with a considerable number of applications, often related to gas storage, selective adsorption or catalysis [1, 2].

The most fundamental methods in molecular modelling, such as density functional theory (DFT), are based on quantum mechanics (QM) [2, 3]. These *ab initio* methods provide highly accurate predictions of the chemical and physical behaviour of a MOF. Unfortunately, due to the current limitations of classical computing and the unfavourable scaling of these methods, it is infeasible to simulate molecular systems of more than a few thousand atoms, which restricts the length scale of the molecular system to only a few nanometers. Moreover, molecular dynamics (MD) simulations based on these *ab initio* methods are, typically, restricted to picosecond time scales [3].

With molecular mechanics (MM), simulating a MOF can be simplified and extended to longer time and length scales. Molecular mechanics is built on the foundation of force fields.

In a force field, the electronic coordinates of a molecular system are completely neglected in favour of an all-atom (AA) description, also known as an atomistic description. Atomistic force fields typically allow for MD simulations of large MOF systems up to nanosecond time scales [3].

Despite the computational advantage of atomistic force fields, they are not efficient enough to simulate phenomena with a large spatial extent, such as spatial disorder in MOFs [4]. Several examples of spatial disorder and cooperative phenomena in synthesised MOFs have been observed experimentally, including correlated defect nanoregions in UiO-66 [5, 6], mesopores in HKUST-1 [7], and phase coexistence in MIL-53 [8].

Fortunately, coarse graining offers a solution to surpass the computational limits of atomistic force field simulations, by mapping atoms onto coarse-grained beads (Section II). Coarse-grained force fields can reach length scales of several tens of nanometers [9, 10]. The micromechanical model, the main subject of this work, is a novel method to construct coarse-grained force fields (Section III). Whereas many coarse-grained force fields are based on atomic interactions [9, 10], the micromechanical model is based on the elastic properties of the unit cell of a MOF [4].

The goal of this work is twofold. Primarily, we want to prove the validity of the micromechanical model as a new coarse-grained approach to simulate MOFs. That includes (i) validating the analytical equations of motion for the coarse-grained nodes, (ii) testing our implementation and (iii) verifying the consistency and accuracy of the results (Section IV). Secondly, our aim is to demonstrate the effectiveness of the micromechanical model, by applying it to several configurations of correlated defects in UiO-66 (Section V).

II. COARSE GRAINING

Like many systems in physics, a molecular system possesses a hierarchy of features on different length scales [11]. In a broad, theoretical sense, coarse graining attempts to reconcile these different length scales. Coarse-grained force fields, specifically, attempt to construct a new force field, designed for large length scales, based on either experimental data (the top-down approach) or on *ab initio* data or atomistic force field simulations (the bottom-up approach).

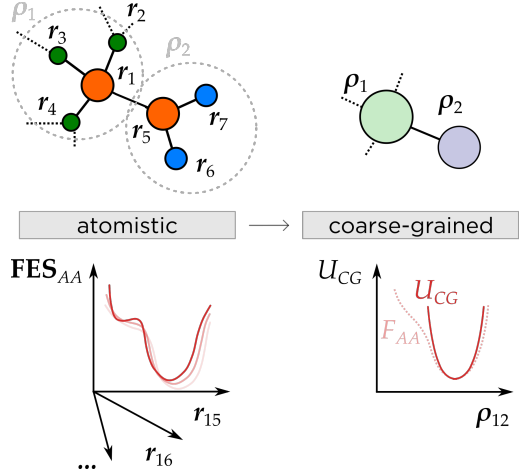


Fig. 1: Schematic illustration of an arbitrary atomistic force field being coarse-grained. Due to the reduction in the number of degrees of freedom, the dynamics of the coarse-grained (CG) representation can be smoother than those of the all-atom (AA) representation.

The construction of a coarse-grained force field and its subsequent application are typically performed in three steps, although most methods do not explicitly specify a mapping [11].

Firstly, the atoms of the molecular system are mapped onto the coarse-grained beads or sites. Starting from an all-atom (AA) description of the molecular system, a mapping usually results in a reduction of the number of variables by about one order of magnitude and a computational speed-up.

$$r \text{ (AA)} \rightarrow \rho \text{ (CG)} \quad (1)$$

An example of such a mapping is shown in Figure 1.

Secondly, the effective interactions between the coarse-grained beads are defined and extracted from a free energy surface (FES) of the atomistic system. The coarse-grained coordinates are introduced as collective variables in the atomistic system. The atomistic variables, *i.e.*, the coordinates of the atoms, are integrated out of the system in favour of the collective variables, which results in a smoother free energy surface $F_{AA}(\rho)$.

$$\text{FES}_{AA}(r)|_{T,V,\dots} \rightarrow F_{AA}(\rho)|_{T,V,\dots} \quad (2)$$

Then, the coarse-grained force field is fitted to $F_{AA}(\rho)$, possibly resulting in an even smoother function.

$$F_{AA}(\rho(r))|_{T,V,\dots} = U_{CG}(\rho)|_{T,V,\dots} \quad (3)$$

The coarse-grained force field acts as the potential energy of the coarse-grained system, but is inherently state-dependent because it was fitted, in general, to a free energy surface.

Thirdly, when the interactions between the coarse-grained beads have been established, MD simulations on the coarse-grained level can be performed. The results of these simu-

lations can be validated with *ab initio* data, with atomistic force field simulations or with experimental data.

Several methods exist that implement these steps, each focusing on different aspects of the coarse graining concept and different criteria to construct and optimise the coarse-grained force field. These methods include MARTINI force fields [12], iterative Boltzmann inversion [13], force matching [14] and relative entropy minimisation [15]. It must be noted that the application of coarse-grained force fields to MOFs is a rather new and unexplored concept. The coarse-grained force field proposed in Ref. 9 was able to reproduce the mechanical properties of HKUST-1 with semi-quantitative accuracy and Ref. 10 demonstrated the application of that same coarse-grained force field in a multiscale problem. These examples are still limited in scope, dealing with only one MOF and one specific multiscale application. Unlike these examples, the micromechanical model was developed for a broad spectrum of MOFs, including flexible MOFs, and aims to reach length scales beyond 10 nm, to accurately capture certain types of spatial disorder, *e.g.*, phase coexistence [4], and to further bridge the gap between molecular modelling and experimental data.

III. THE MICROMECHANICAL MODEL

A. Concept

The micromechanical procedure to construct a coarse-grained force field, as originally proposed in Ref. 4, can be described in four steps, as shown in Figure 2. In the first step of this procedure, a three-dimensional grid of nanocells is introduced, which represents the material being investigated. The grid of nanocells can have periodic boundaries, to represent an infinitely repeating structure, or not, to represent a finite crystal. In the grid, a *type* is assigned to each nanocell. The type of a nanocell, as we define it, is (i) determined by its atomic structure and (ii) uniquely represented by its equilibrium elastic properties. In theory, the layout of the grid can be matched to experimental observations of synthesised MOF crystals to achieve a more accurate, more realistic system than current simulation methods allow, given their spatial limitations. The appearance and behaviour of defect clusters, for instance, can be mimicked by including nanocells of a defective type. The presence of an internal or external surface can be mimicked by including nanocells of a surface type.

In the second step of the procedure, a mapping is performed from the old dynamical variables of the grid, the positions and momenta of atoms, to a new set of dynamical variables, the positions and momenta of massive, coarse-grained nodes. These micromechanical nodes are located on the vertices of each nanocell in the grid. They represent a mapping of as many atoms as possible onto as few beads as possible, a maximally coarse-grained system.

The micromechanical nodes are formally treated as classical particles, governed by their equations of motion (Section III-B). They are able to track local or long-range, potentially correlated, elastic deformations in a MOF. The mass of

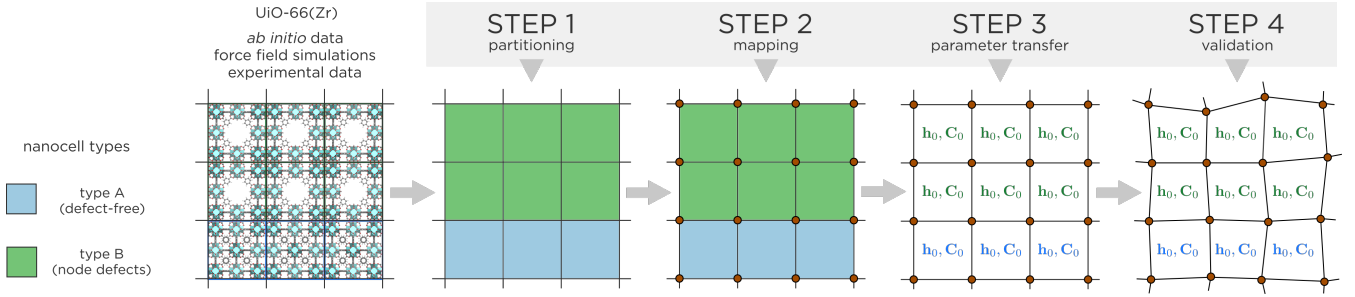


Fig. 2: Schematic overview of the micromechanical procedure.

a node is calculated by summing up one eighth of the mass of each adjacent nanocell, which is assumed to be homogeneous and distributed among its nodes. The positions and momenta of the nodes are conjugate pairs of dynamical variables. These are needed to fully describe the state of the micromechanical system.

The third step of the micromechanical procedure is the transfer of parameters between levels of theory. Simulations on a higher level of theory than the micromechanical model, either *ab initio* calculations or atomistic force field simulations, are performed to obtain the elastic properties of each nanocell type. In the micromechanical model, the nanocells act like an elastic coupling between the micromechanical nodes. The elastic deformation energy of a nanocell is estimated by means of a harmonic approximation in the strain tensor. This harmonic approximation is a second-order approximation in the strain tensor, fully parametrised by the elastic properties of the nanocell, *i.e.*, by the equilibrium cell matrix and the elasticity tensor of its nanocell type (\mathbf{h}_0 and \mathbf{C}_0). As parameters, these elastic properties fulfil the same roles as the rest length and the elastic constant of a classical spring, respectively, yet representing a three-dimensional material.

In the fourth and final step of the micromechanical procedure, a micromechanical MD simulation is performed. Despite not pertaining to molecules or atoms, a micromechanical MD simulation is identical to an atomistic MD simulation. The positions and momenta of the micromechanical nodes are updated at discrete, equidistant points in time with the velocity Verlet algorithm [16]. More details concerning the equations of motion are provided in Section III-B. Lastly, it is worth noting that a micromechanical MD simulation can be performed in different ensembles, including the isochoric-isothermal (N, V, T) and the isobaric-isothermal (N, P, T) ensembles, just like any other MD simulation. The results of the MD simulation can be compared to atomistic force field simulations, *ab initio* data or experimental data.

B. Equations of motion

In the following text, micromechanical nodes are indexed with Roman letters (k, l, m). Nanocells are indexed with Greek letters (κ, λ, μ). These indices refer to the location of a node or a nanocell in a three-dimensional grid, which represents

the MOF. The subscript zero indicates that a property of a nanocell is an equilibrium property, determined from a higher level of theory and remaining constant throughout any micromechanical simulation. Here, the term *equilibrium* is used to indicate the most stable, energetically most favourable, state of the nanocell if it could be surrounded by periodic images of itself. Finally, the superscript (s) denotes one of eight matrix representations of a nanocell, as defined in Figure 3. This is where our derivation of the micromechanical equations of motion differs from the original formulation, as proposed in Ref. 4. The concept of *representations* was introduced to take into account non-periodic boundary conditions, an essential component of the model if we wish to simulate finite crystals.

When a nanocell has been deformed, its eight representations, $\mathbf{h}_{\kappa\lambda\mu}^{(s)}$, differ from its equilibrium cell matrix, $\mathbf{h}_{\kappa\lambda\mu,0}$. The deformed nanocell wishes to relax to its equilibrium state, much like a stretched classical spring wishes to relax to its rest length.

The 3×3 finite Lagrangian strain tensor is a dimensionless measure of the nanocell's deviation from its equilibrium cell matrix. Like the cell matrix, the strain tensor is also not uniquely defined. Each nanocell has eight representations of its strain tensor, which are defined as

$$\mathbf{\epsilon}_{\kappa\lambda\mu}^{(s)} = \frac{1}{2} \left[\mathbf{h}_{\kappa\lambda\mu,0}^{-T} \left(\mathbf{h}_{\kappa\lambda\mu}^{(s)} \right)^T \left(\mathbf{h}_{\kappa\lambda\mu}^{(s)} \right) \mathbf{h}_{\kappa\lambda\mu,0}^{-1} - \mathbf{1} \right]. \quad (4)$$

We define the set $S_{\kappa\lambda\mu}$ as the set of eight micromechanical nodes surrounding nanocell (κ, λ, μ) , *i.e.*, the vertices of nanocell (κ, λ, μ) . As shown in Figure 3, an arbitrary nanocell representation $\mathbf{h}_{\kappa\lambda\mu}^{(s)}$ depends on the dynamical variables $\{\mathbf{r}_{klm}\}_{S_{\kappa\lambda\mu}}$. Therefore, the matrix representations of a nanocell and its strain tensor representations are also implicitly time-dependent.

$$\begin{aligned} \mathbf{h}_{\kappa\lambda\mu}^{(s)} &\equiv \mathbf{h}_{\kappa\lambda\mu}^{(s)} \left(\{\mathbf{r}_{klm}(t)\}_{S_{\kappa\lambda\mu}} \right) \\ \mathbf{\epsilon}_{\kappa\lambda\mu}^{(s)} &\equiv \mathbf{\epsilon}_{\kappa\lambda\mu}^{(s)} \left(\{\mathbf{r}_{klm}(t)\}_{S_{\kappa\lambda\mu}} \right) \end{aligned} \quad (5)$$

For the sake of compact notation, this dependence is not stated explicitly in the following derivations.

The elastic energy of a nanocell representation is expressed as a harmonic approximation. This is a function of its 3×3 strain tensor representation, its $3 \times 3 \times 3 \times 3$ elasticity tensor

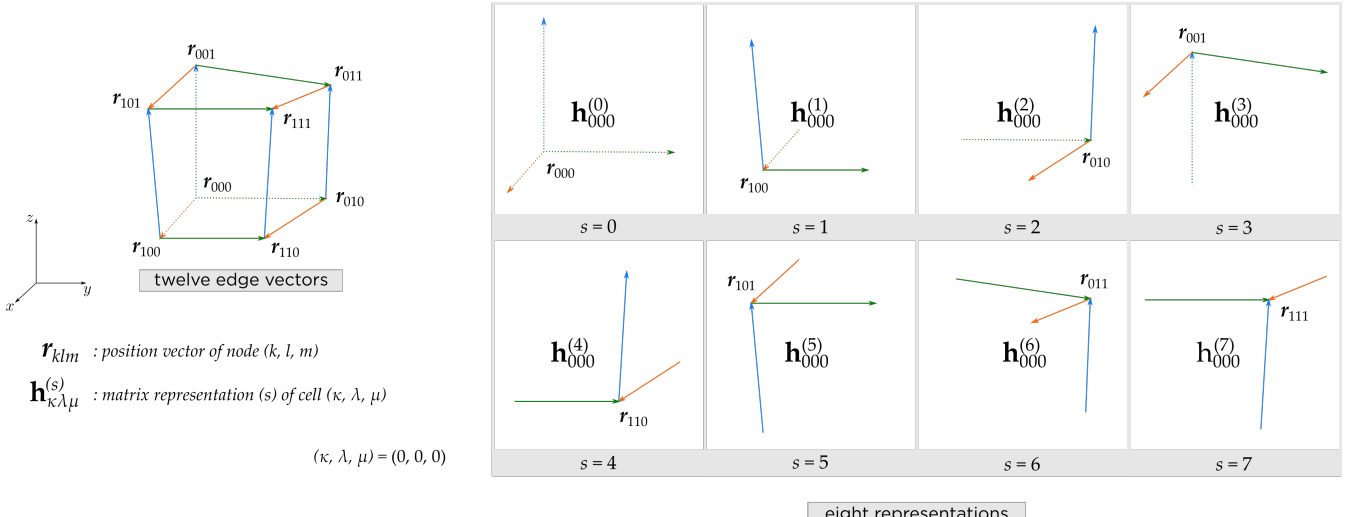


Fig. 3: Representations of an arbitrarily shaped nanocell in the micromechanical model. Each vertex of the nanocell is a micromechanical node. To describe the nanocell at any point in time, its twelve edge vectors are used to construct eight distinct cell matrices.

and the corresponding representation of its volume. Implicitly, this elastic energy is also a function of the coordinates of the surrounding nodes.

$$U_{\kappa\lambda\mu}^{(s)} = \frac{1}{2} \det(h_{\kappa\lambda\mu}^{(s)}) (\epsilon_{\kappa\lambda\mu}^{(s)})^T : C_{\kappa\lambda\mu,0} : (\epsilon_{\kappa\lambda\mu}^{(s)}) \quad (6)$$

The potential energy of a nanocell is the mean of the potential energies of its eight representations.

$$U_{\kappa\lambda\mu} = \frac{1}{8} \sum_{s=0}^7 U_{\kappa\lambda\mu}^{(s)} \quad (7)$$

Each nanocell contributes to the total potential energy of the system.

$$U_{sys} = \sum_{\kappa,\lambda,\mu} U_{\kappa\lambda\mu} = \sum_{\kappa,\lambda,\mu} \left(\frac{1}{8} \sum_{s=0}^7 U_{\kappa\lambda\mu}^{(s)} \right) \quad (8)$$

The Hamiltonian of the micromechanical system is then, simply, the sum of the kinetic energy of the nodes and the total potential energy.

$$H_{sys} = \sum_{k,l,m} \frac{\dot{p}_{klm}^2}{2m_{klm}} + U_{sys} \quad (9)$$

Using the Hamiltonian, a set of coupled equations of motion for the micromechanical nodes can be obtained.

$$\begin{aligned} \dot{p}_{klm} &= -\nabla_{r_{klm}} H_{sys} = -\nabla_{r_{klm}} U_{sys} \\ \dot{r}_{klm} &= \nabla_{p_{klm}} H_{sys} = \frac{\dot{p}_{klm}}{m_{klm}} \end{aligned} \quad (10)$$

These equations of motion can be numerically integrated using the second-order accurate velocity Verlet algorithm [16].

IV. IMPLEMENTING AND VALIDATING THE MICROMECHANICAL MODEL

Our implementation of the micromechanical model is publicly available as a Python package named MicMec [17]. In concrete terms, MicMec provides functionality to build micromechanical systems, to perform simulations and to analyse and visualise results. MicMec is intentionally similar to Yaff, a Python package used for atomistic force field simulations [18].

In order to validate both our implementation and the micromechanical model as a concept, several tests were performed with MicMec. The consistency of the analytical equations of motion was checked, by verifying whether the negative numerical derivative of the potential energy matched the force acting on a single node in a homogeneous $3 \times 3 \times 3$ test system. When this was confirmed, several MD simulations were performed with the same system. In the (N, V, E) ensemble, energy was conserved. In the (N, P, T) ensemble, pressure and temperature were controlled adequately. Both observations give confidence in the MicMec implementation.

The parameters of the homogeneous $3 \times 3 \times 3$ test system were chosen to be simple and should lead to predictable outcomes. Unfortunately, an MD simulation of the test system in the (N, P, T) ensemble does not produce a consistent, or reliable, elasticity tensor. The elasticity tensor of the homogeneous system does not match the elasticity tensor of an individual nanocell. While some deviation is expected between the dynamic elasticity tensor, calculated from the MD simulation, and the static elasticity tensor of an individual nanocell, which we chose as an input parameter, the deviation is too large to ignore. Therefore, the output of the model does not seem to match the input. We have not been

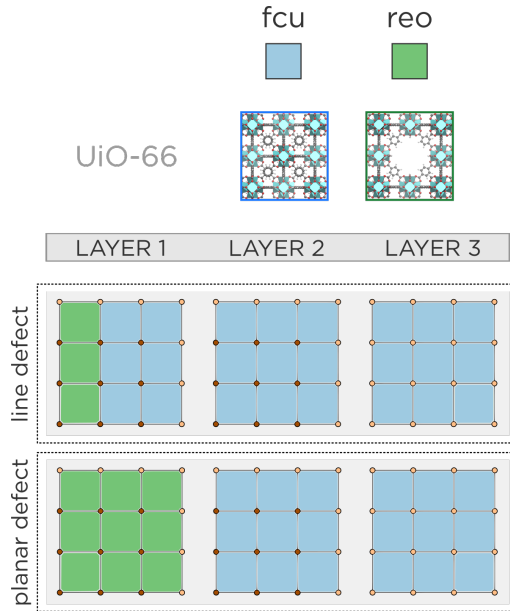


Fig. 4: Schematic overview of two different configurations of defective **reo** nanocells surrounded by defect-free **fcu** nanocells: a line defect and a planar defect. Each configuration is a $3 \times 3 \times 3$ system with periodic boundary conditions.

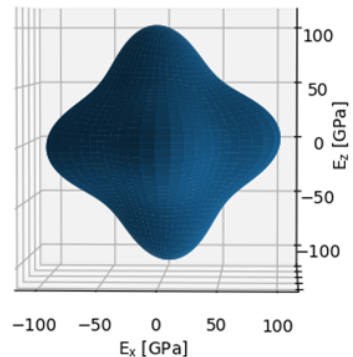
able to pinpoint the cause of this convergence issue. We were able to determine, however, that a relaxed potential energy scan of the test system produces a consistent and accurate value for the bulk modulus, in line with the bulk modulus we chose for the individual nanocells. So, the static calculations are correct and consistent, but the dynamic calculations are unreliable.

V. CORRELATED DEFECTS IN UiO-66

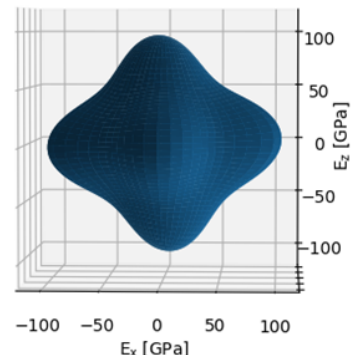
Having validated a test system, we proceed to investigate a practical micromechanical system, based on an atomistic reference of UiO-66. The rigid MOF UiO-66 is modelled as a solid mixture of defect-free nanocells that adopt the **fcu** topology and cluster-defective nanocells that adopt the **reo** topology. Here, we mention two different configurations of **reo** nanocells, surrounded by **fcu** nanocells, that were simulated with MicMec and were compared to a completely homogeneous **fcu** system. Both configurations are shown in Figure 4. The aim of these experiments is to qualitatively, or semi-quantitatively, predict the mechanical behaviour of UiO-66.

A micromechanical MD simulation of the UiO-66 system in the (N, P, T) ensemble does not yield an accurate dynamic elasticity tensor. The (dynamic) elasticity tensor of a homogeneous system of exclusively **fcu** nanocells, for instance, does not match the (static) elasticity tensor of the **fcu** nanocell type. This issue has been previously reported in Section IV. Nevertheless, the bulk modulus and the eigenvalues and eigenvectors derived from the elasticity tensor provide use-

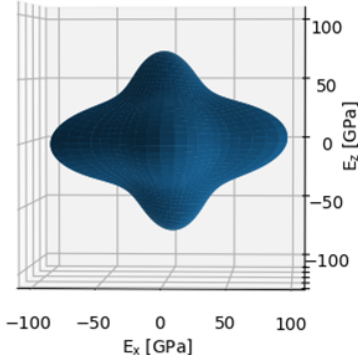
ful, albeit qualitative, information. The eigenvectors of the elasticity tensor are the elastic deformation modes of the micromechanical system. The stress tensors of these deformation modes can be further decomposed into their own eigenvalues, the principal stresses, and their own eigenvectors, the principal planes. The directional Young modulus can be derived from the elasticity tensor, as well [19]. A three-dimensional visualisation of the directional Young modulus



(a) Homogeneous.



(b) Line defect.



(c) Planar defect.

Fig. 5: Directional Young modulus of a homogeneous $3 \times 3 \times 3$ UiO-66 system and of the two configurations of Figure 4.

reveals the directions for which a nanocell is most flexible and most rigid under a tensile deformation. In Figure 5, the directional Young moduli of the homogeneous system, the line defect and the planar defect have been plotted. For all three configurations, a uniaxial deformation along the x -axis yields a similar result. Along the z -axis, the line defect is slightly more flexible than the homogeneous system. The planar defect is the most flexible of the three configurations along the z -axis.

The bulk modulus of a micromechanical system can also be calculated by means of a relaxed scan, which does yield accurate and consistent results. For quantitative conclusions about UiO-66, we turn to these results, as they lie closer to the bulk modulus of the atomistic **fcu** nanocell. For instance, a significant concentration of **reo** nanocells, e.g., one third of the total amount of nanocells, can lower the bulk modulus of the system by more than 20%. Future simulations could provide valuable insight into the limits of mechanical stability when engineered defects, e.g., for the purpose of adsorption, are introduced in a MOF like UiO-66.

VI. CONCLUSIONS

We can summarise the four main achievements of this work as follows.

- 1) The micromechanical model has been implemented and is available as a Python package named MicMec. The micromechanical equations of motion were modified from their original formulation in Ref. 4 and have been derived correctly.
- 2) A micromechanical MD simulation in the (N, V, E) ensemble conserves the total energy of the system, as it should. In the (N, P, T) ensemble, pressure and temperature are controlled adequately.
- 3) A relaxed potential energy scan of a micromechanical system is able to produce a reliable estimate of the static bulk modulus of the system.
- 4) Semi-quantitative and qualitative results of the micromechanical model have been reported for a case study of defective nanocells in UiO-66. The static and dynamic bulk modulus, the directional Young modulus and the principal stresses of the first deformation mode of a micromechanical UiO-66 system were all observed to vary as a function of defect concentration and correlation.

Despite these achievements, the current implementation of the micromechanical model can still be improved. The dynamic elasticity tensor, calculated from a micromechanical MD simulation, does not converge to its intended value. We have not been able to fix this issue. Additionally, many more experiments can be performed with the micromechanical model. MicMec supports the inclusion of nanocells with more than one metastable state and, thus, more than one set of elastic properties. Therefore, it is possible to simulate phase coexistence in a MOF, e.g., MIL-53. It is also possible to perform a simulation of a MOF with mesopores, e.g., HKUST-1. Mesoporosity can be mimicked by the inclusion of

empty nanocells in the grid of the micromechanical system, which MicMec also supports. Eventually, the model should be compared directly to other coarse-grained force fields, as those are the only methods, besides experiments on synthesised MOFs, that reach the same length scales as the micromechanical model.

REFERENCES

- [1] H.-C. Zhou, J. R. Long, and O. M. Yaghi, "Introduction to metal-organic frameworks," *Chem. Rev.*, vol. 112, pp. 673–674, 2012.
- [2] S. M. J. Rogge, A. Bavykina, J. Hajek, H. Garcia, A. I. Olivos-Suarez, A. Sepúlveda-Escribano, A. Vimont, G. Clet, P. Bazin, F. Kapteijn, M. Daturi, E. V. Ramos-Fernandez, F. X. Llabrés i Xamena, V. Van Speybroeck, and J. Gascon, "Metal-organic and covalent organic frameworks as single-site catalysts," *Chem. Soc. Rev.*, vol. 46, pp. 3134–3184, 2017.
- [3] V. Van Speybroeck, S. Vandenhaute, A. E. Hoffman, and S. M. J. Rogge, "Towards modeling spatiotemporal processes in metal-organic frameworks," *Trends Chem.*, vol. 3, pp. 605–619, 2021.
- [4] S. M. J. Rogge, "The micromechanical model to computationally investigate cooperative and correlated phenomena in metal-organic frameworks," *Faraday Discuss.*, vol. 225, pp. 271–285, 2020.
- [5] M. J. Cliffe, W. Wan, X. Zou, P. A. Chater, A. K. Kleppe, M. G. Tucker, H. Wilhelm, N. P. Funnell, F.-X. Coudert, and A. L. Goodwin, "Correlated defect nano-regions in a metal-organic framework," *Nat. Commun.*, vol. 5, p. 4176, 2014.
- [6] L. Liu, D. Zhang, Y. Zhu, and Y. Han, "Bulk and local structures of metal-organic frameworks unravelled by high-resolution electron microscopy," *Commun. Chem.*, vol. 3, pp. 1–14, 2020.
- [7] L. Guo, J. Du, C. Li, G. He, and Y. Xiao, "Facile synthesis of hierarchical micro-mesoporous HKUST-1 by a mixed-linker defect strategy for enhanced adsorptive removal of benzothiophene from fuel," *Fuel*, vol. 300, p. 120955, 2021.
- [8] S. M. J. Rogge, M. Warquier, and V. Van Speybroeck, "Unraveling the thermodynamic criteria for size-dependent spontaneous phase separation in soft porous crystals," *Nat. Commun.*, vol. 10, p. 4842, 2019.
- [9] J. Dürholt, R. Galvelis, and R. Schmid, "Coarse graining of force fields for metal-organic frameworks," *Dalton Trans.*, vol. 45, p. 4370–4379, 2015.
- [10] R. Semino, J. Dürholt, R. Schmid, and G. Maurin, "Multiscale modeling of the HKUST-1/poly(vinyl alcohol) interface: From an atomistic to a coarse graining approach," *J. Phys. Chem.*, vol. 121, pp. 21491–21496, 2017.
- [11] S. Cranford and M. Buehler, "Coarse-graining parameterization and multiscale simulation of hierarchical systems," in *Multiscale modeling: From atoms to devices*, 1st ed., P. Derosa and T. Cagin, Eds. Boca Raton: CRC Press, 2010, ch. 2, pp. 13–34.
- [12] S. J. Marrink, H. J. Risselada, S. Yefimov, D. P. Tieleman, and A. H. de Vries, "The MARTINI force field: Coarse grained model for biomolecular simulations," *J. Phys. Chem. B*, vol. 111, pp. 7812–7824, 2007.
- [13] T. Moore, C. Iacovella, and C. McCabe, "Derivation of coarse-grained potentials via multistate iterative Boltzmann inversion," *J. Chem. Phys.*, vol. 140, p. 224104, 2014.
- [14] W. Noid, J.-W. Chu, G. Ayton, S. Izvekov, G. Voth, A. Das, and H. Andersen, "The multiscale coarse-graining method. I. A rigorous bridge between atomistic and coarse-grained models," *J. Chem. Phys.*, vol. 128, p. 244114, 2008.
- [15] M. Shell, "The relative entropy is fundamental to multiscale and inverse thermodynamic problems," *J. Chem. Phys.*, vol. 129, p. 144108, 2008.
- [16] D. Frenkel and B. Smit, *Understanding Molecular Simulation: From algorithms to applications*, 2nd ed. San Diego: Academic Press, 2002.
- [17] J. Vandewalle, "MicMec, the micromechanical model." [Online]. Available: <https://github.com/JIvdwall/micmec>
- [18] T. Verstraelen, L. Vanduyfhuys, S. Vandenbrande, and S. M. J. Rogge, "Yaff, yet another force field." [Online]. Available: <http://molmod.ugent.be/software/>
- [19] A. Ortiz, A. Boutin, A. Fuchs, and F.-X. Coudert, "Anisotropic elastic properties of flexible metal-organic frameworks: How soft are soft porous crystals?" *Phys. Rev. Lett.*, vol. 109, p. 195502, 2012.

Contents

Preface	i
Copyright agreement	ii
Summary	iii
Extended abstract	iv
Contents	x
List of abbreviations	xii
List of symbols	xiii
1 Introduction	1
1.1 Metal-organic frameworks	1
1.2 Correlated spatial disorder	3
1.2.1 UiO-66	4
1.2.2 HKUST-1	7
1.2.3 MIL-53 and other pillared-layered MOFs	8
1.3 Molecular modelling	10
1.3.1 Quantum mechanics	10
1.3.2 Molecular mechanics	12
1.4 Goal	13
1.5 Outline	14
2 Coarse graining	16
2.1 Introduction	16
2.2 Coarse-grained force fields	18
2.2.1 MARTINI force fields	19
2.2.2 Iterative Boltzmann inversion	19
2.2.3 Force matching	20
2.2.4 Relative entropy minimisation	21
2.3 Coarse graining MOFs	21

2.4	Conclusions	25
3	The micromechanical model	26
3.1	Concept	26
3.2	Advantages	30
3.3	Parameters	32
3.4	Limitations	36
3.5	Equations of motion for unistable nanocells	39
3.6	Equations of motion for bistable nanocells	42
4	Implementing and validating the micromechanical model	46
4.1	MicMec	46
4.1.1	Preprocessing	46
4.1.2	Core routines	47
4.1.3	Temperature and pressure control	50
4.1.4	Postprocessing	52
4.2	Validation	52
4.2.1	Testing the micromechanical model	52
4.2.2	Testing geometry optimisations	58
4.2.3	Testing molecular dynamics simulations	58
4.3	Conclusions	64
5	Correlated defects in UiO-66	65
5.1	Introduction	65
5.2	Methods	66
5.3	Results	68
5.4	Conclusions	73
6	Conclusions and outlook	74
References		77

List of abbreviations

AA	all-atom
AIMD	ab initio molecular dynamics
CG	coarse-grained
DFT	density functional theory
FES	free energy surface
FF	force field
HF	Hartree-Fock
HRTEM	high-resolution transmission electron microscopy
MD	molecular dynamics
MM	molecular mechanics
MOF	metal-organic framework
MS-CG	multiscale coarse graining
PES	potential energy surface
PXRD	powder X-ray diffraction
QM	quantum mechanics
RDF	radial distribution function
SED	scanning electron diffraction

List of symbols

SCALARS

t	time
m	mass
N	number of particles
P	pressure
T	temperature
V	volume
E	energy
F	free energy
U	potential energy
K	bulk modulus
$E(\mathbf{u})$	directional Young modulus
$G(\mathbf{u}, \mathbf{v})$	directional shear modulus

VECTORS

$\mathbf{r}; \rho$	position
\mathbf{v}	velocity
\mathbf{p}	momentum
\mathbf{f}	force
$\mathbf{a}, \mathbf{b}, \mathbf{c}$	cell vectors

MATRICES AND TENSORS

\mathbf{h}	cell matrix (3×3)
\mathbf{h}_0	equilibrium cell matrix (3×3)
$\mathbf{C}_0; \mathbf{C}$	elasticity tensor ($3 \times 3 \times 3 \times 3$)
\mathbf{S}	compliance tensor ($3 \times 3 \times 3 \times 3$)
\mathbf{W}	virial tensor (3×3)
$\boldsymbol{\epsilon}$	strain tensor (3×3)
$\boldsymbol{\sigma}$	stress tensor (3×3)

1

Introduction

1.1 Metal-organic frameworks

For the past three decades, metal-organic frameworks or MOFs have been an exceedingly important topic in materials research. In general, a MOF is composed of inorganic clusters or metal ions connected by organic linkers [1, 2]. The organic linkers of the MOF create a sparse framework between the metal ions or inorganic clusters, resulting in a porous, often flexible, atomic structure.

A typical MOF is a crystalline material. A micrometer-sized MOF crystallite contains trillions of atoms, but the main building block of its atomic structure is often a single, periodically repeating, unit cell that consists of only a few hundred atoms. Throughout this work, we will refer to the unit cell of a MOF as a *nanocell* on account of its nanometer-scale dimensions. In Figure 1.1, an example of a MOF, UiO-66, is shown.

At face value, much of the interest in MOFs can be attributed to the variability of their chemical composition and atomic structure [1, 4]. The number of possible combinations of inorganic clusters and organic linkers, each combination representing a different, albeit hypothetical, material, is nearly infinite. Fortunately, the structural features of this full set of MOFs can be classified based on a smaller set of well-known topological networks [5]. The nanocell of UiO-66, for instance, belongs to the face-centred cubic (*fcu*) topology.

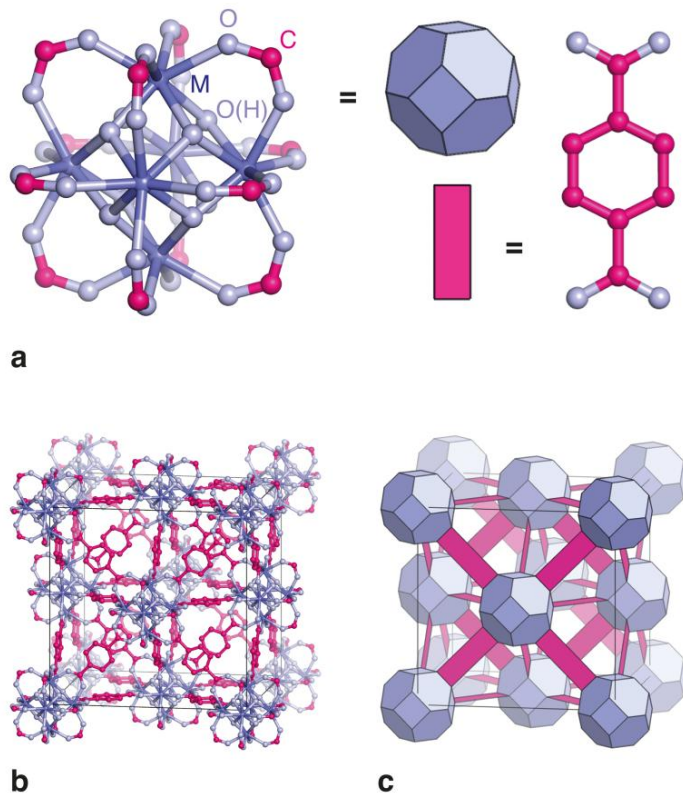


Figure 1.1: A typical metal-organic framework: UiO-66. As shown in (a), the inorganic clusters of the framework are often represented as octahedra and the organic linkers as planar sheets. In (b), the complete atomic structure of the UiO-66 nanocell is shown and in (c) its simplified representation. Figure reproduced from Ref. 3.

In the full set of MOFs, researchers have discovered materials with diverse chemical, thermal, mechanical, electronic and optical properties [1, 2]. As a result, the list of potential and actual applications of MOFs continues to grow. A significant number of these applications are related to gas storage, selective adsorption and catalysis [6, 7, 8, 9, 10]. A MOF is ideally suited for these tasks by virtue of its ultrahigh porosity and its enormous internal surface area, which offers many adsorption sites for molecules passing through the material. The free volume fraction in a MOF can be as high as 90% and the internal surface area can extend beyond $6000\text{ m}^2/\text{g}$ [1].

The versatility of MOFs has been fuelled by the need for advanced materials in many, if not all, high-tech industries. Currently, the scope of MOF research covers many different fields, such as clean energy, thin films, shock absorption, sensing and drug delivery [1, 7, 11]. A considerable portion of clean energy research is dedicated to carbon dioxide capture, a promising venture to reduce emissions from the combustion of fossil fuels in power plants. A well-designed MOF can separate carbon dioxide from other gases passing through its pores, by allowing only carbon dioxide to adsorb on its internal surfaces [7].

Another significant part of the popularity of MOFs in scientific literature and in industrial applications can be attributed to their extraordinary tunability [1, 12]. Aside from economic concerns and technological barriers, the tunability of a MOF in a practical design context is only limited by stability constraints. Usually, the thermal, chemical and mechanical stability of the MOF, as well as its stability in the presence of water (hydrostability), have to be imposed [13]. Despite these constraints, the properties of a MOF can be controlled to a large extent by varying the chemical composition of the inorganic cluster and by choosing an appropriate organic linker. For the purpose of catalysis, the chemical properties of the inorganic cluster can be especially important, as evidenced by, for instance, the large differences in catalytic activity of isostructural UiO-66(Zr), UiO-66(Hf) and UiO-66(Ce) materials [9].

Additionally, the adsorption and catalytic performance of a MOF can be enhanced by optimising the structure of its pores, taking into account the size and shape of the adsorbed molecule [12, 14]. Moreover, it has been shown that the synthesis of a MOF can be controlled to induce vacancy defects or compositional disorder in the material, adding yet another layer of opportunities and engineering challenges to MOF design [15, 16].

As the number of applications of MOFs grows, so does the demand for computational studies related to MOFs. In the past, machine learning algorithms have been applied to filter through vast numbers of hypothetical MOFs to find the optimal design for any given application [4]. On a deeper level, computer simulations may serve either as a design tool, offering valuable predictions regarding the stability and performance of the material, or as an analysis tool, offering explanations for failed experiments and physical insight into unexpected phenomena [2, 11, 13].

1.2 Correlated spatial disorder

MOFs blur the line between soft and solid matter, often being more flexible than solid, inorganic crystals and more rigid than liquid crystals or polymers [13, 17]. Despite not exhibiting the same degree of short-range or long-range order as a typical inorganic crystal, a MOF is often still treated as a perfect crystal in computer simulations, represented by a defect-free nanocell with periodic boundary conditions. For a synthesised MOF closely resembling a perfect crystal, the predictions made by these simulations are expected to be accurate.

However, spatial disorder is inevitable for nearly all materials, especially on a macroscopic scale [15]. The two main types of spatial disorder in inorganic crystals, namely structural disorder, such as dislocations or vacancies, and compositional disorder, such as inhomogeneities, are also encountered in MOFs [3]. Vacancy defects are especially important in MOFs, including both missing linker and missing cluster defects [15, 3, 18]. The incorporation of any type of defect in a material gives rise to a local perturbation of its material properties [3]. This local perturbation may appear as an electrostatic field, as a mechanical strain field, or as a chemical potential. If the strength and range of the perturbation

are limited, the defect may be isolated, not interacting at all with other defects and not influencing the formation of new defects during the synthesis and growth of the material. Without external influence, isolated defects are randomly distributed throughout the material. When the concentration of a defect increases, or when its local perturbation is sufficiently strong, it may interact with other defects, no longer being isolated. These types of defects are spatially correlated, in the sense that the presence of one defect affects the likelihood of finding another defect nearby [3, 19]. In MOFs specifically, the creation of correlated defects involves kinetic effects during the growth of the crystal [16, 19].

1.2.1 UiO-66

In many computational and experimental studies, UiO-66 is considered to be a prime example of a MOF containing correlated defects [14, 3, 18, 19]. The inorganic cluster of UiO-66 usually contains zirconium (UiO-66(Zr)), but hafnium-based and cesium-based variants (UiO-66(Hf) and UiO-66(Ce)) have been synthesised as well [9]. In general, UiO-66 is a rigid MOF, known for its excellent thermal, chemical and mechanical stability. In the absence of vacancy defects, it adopts the face-centred cubic (**fcu**) topology, wherein each inorganic cluster is connected to twelve other clusters by organic terephthalate linkers [3]. The pores of UiO-66 are zero-dimensional cavities, shaped like tetrahedra or octahedra and connected through triangular windows.

The highly-connected, regular structure of UiO-66 can be disrupted by missing linker defects and missing cluster defects. The concentration of both of these defects can be controlled in a systematic manner by varying the concentration of acid modulator and terephthalate linker during the synthesis of the MOF [16]. Tuning the duration and temperature of the synthesis provides additional control [10, 19].

The existence of vacancy defects in UiO-66 was never assumed. A history of research has been built up to prove their existence. Early evidence, obtained from neutron diffraction experiments, showed that in UiO-66(Zr), about 10% of all terephthalate linkers could be missing [10]. Powder X-ray diffraction (PXRD) experiments provided further proof of these missing linker defects, in UiO-66(Hf) [3].

In the PXRD spectrum, however, diffuse scattering peaks were observed which could not be attributed to the **fcu** topology of the crystal, nor to the ordering of solvent molecules in the pores of the crystal, nor to the presence of missing linker defects alone. Instead, these diffuse scattering peaks indicated the presence of short-range ordered, correlated, missing cluster defects. With anomalous X-ray scattering, it was established that these missing clusters were missing in their entirety, instead of being broken up. From electron diffraction experiments, it became clear that the cubic symmetry of the crystal was preserved by the missing cluster defects. All of these results pointed to one conclusion: the existence of correlated defect nanoregions in UiO-66(Hf).

Recent experimental evidence has shown that correlated defect nanoregions appear in both UiO-66(Zr) and UiO-66(Hf) [3, 18]. These nanoregions are dispersed throughout the material and contain groups

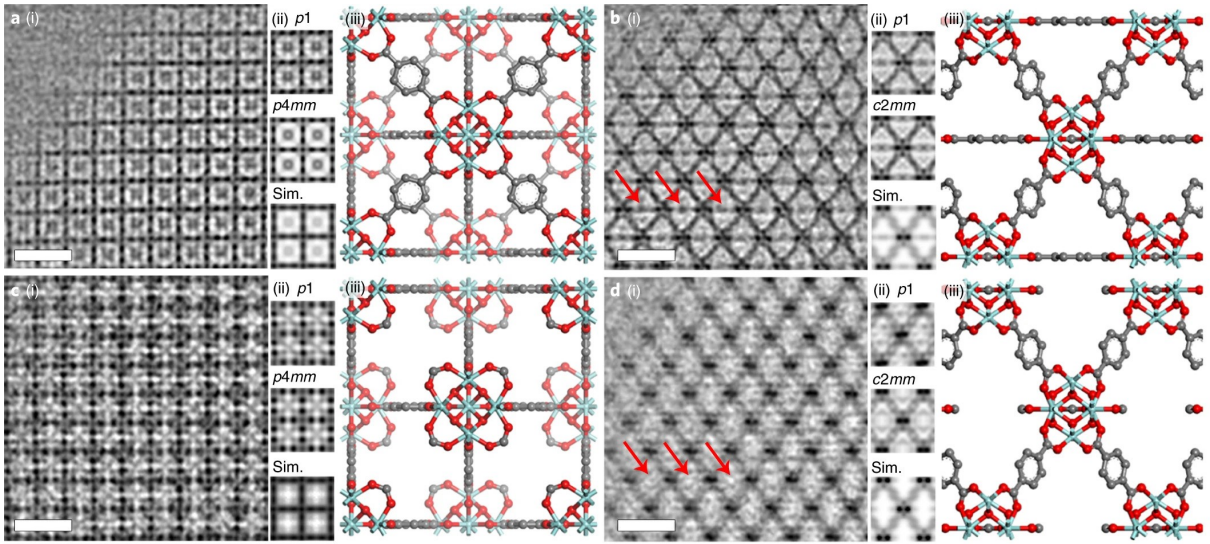


Figure 1.2: Top row: processed high-resolution transmission electron microscopy (HRTEM) images and structural models of perfect UiO-66(Zr) along the [001] and [110] zone axes, in (a) and (b) respectively. Bottom row: processed HRTEM images and structural models of a missing linker defect in UiO-66(Zr) along the [001] and [110] zone axes, in (c) and (d) respectively. The red arrows indicate the location of the missing linkers in the bottom-right panel. Figure reproduced from Ref. 18.

of missing cluster defects. Within these nanoregions, UiO-66 adopts the **reo** topology instead of the **fcu** topology. Due to the absence of one cluster in each nanocell, the remaining clusters in the **reo** topology are connected to only eight clusters each, instead of the usual twelve. These defective nanoregions can coexist with their non-defective surroundings because the **reo** topology of UiO-66 is mechanically stable in the regular **fcu** topology, hinted at by the fact that their equilibrium nanocell dimensions are very similar. During crystal growth, the defective nanocells can survive large shear forces precisely because of their mechanical stability [19].

In later research, the diffuse scattering peaks in the PXRD experiment were observed to become weaker when the crystallisation time of the MOF was increased from one day to three days [18]. In the samples that were grown for three days, many unstable missing cluster defects had disappeared due to the shear forces induced by the growth of the crystal. Real-space direct imaging of the samples confirmed these findings. Specifically, the researchers were able to view individual **fcu** and **reo** nanocells in the samples with low-dose high-resolution transmission electron microscopy (HRTEM) [18, 20]. These images also revealed the presence of many nanocells with the body-centred cubic (**bcc**) topology and occasionally, a nanocell with the simple cubic (**scu**) topology. Density functional theory (DFT) calculations were then employed to classify these defective nanocells. The defect-free **fcu** topology was clearly the most stable configuration, followed by the **bcc** topology, representing missing linker defects, the **reo** topology, representing missing cluster defects, and the **scu** topology, representing a combination of missing linker

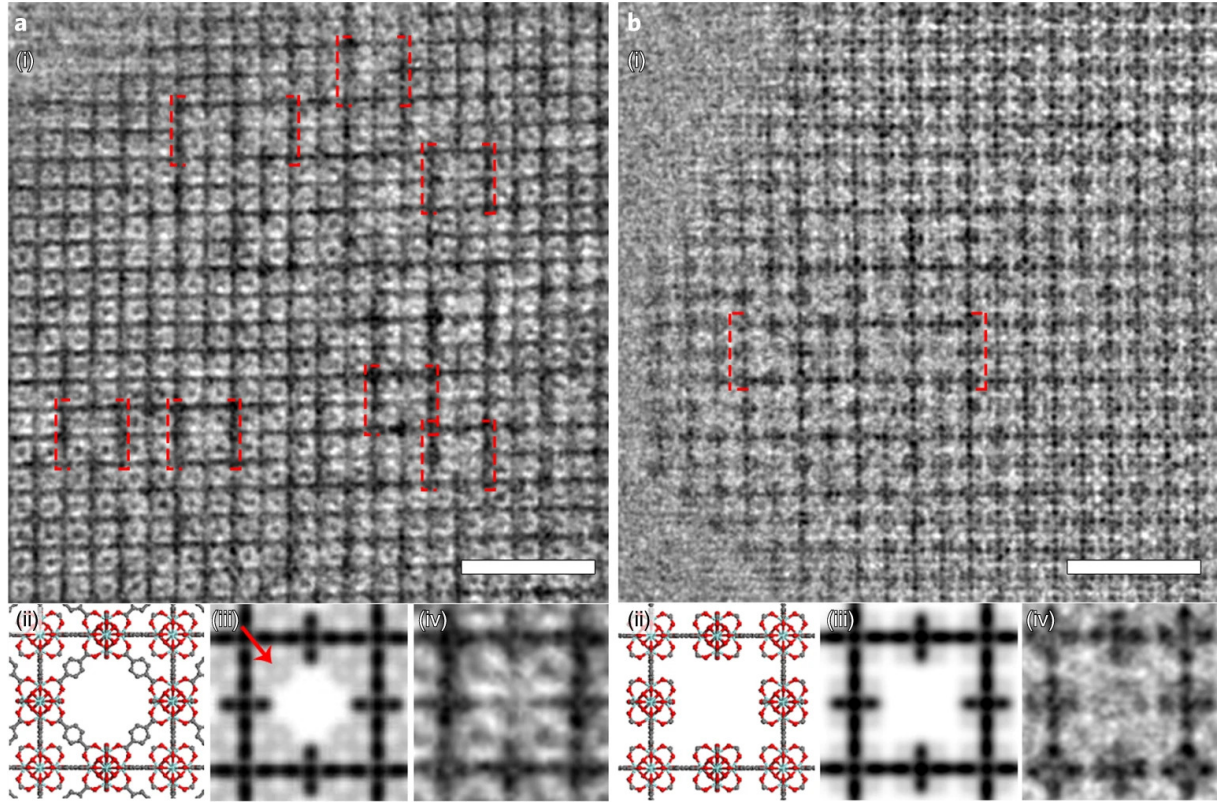


Figure 1.3: Processed HRTEM images of the [001] direction in UiO-66(Zr), showing different types of missing-cluster defects, adopting the **reo** topology in (a) and the **scu** topology in (b). The white scale bars represent a length of 5 nm. The nanocells in the image panels, shown by red dashed boxes, are extracted as individual images, aligned with each other, and merged to generate an averaged image. Figure reproduced from Ref. 18.

and missing cluster defects. These four types of defective nanocells are shown in Figure 1.4. Beyond direct imaging, scanning electron diffraction (SED) has been used to investigate the orientation and growth of the correlated defect nanoregions [16]. These measurements found that the defect nanoregions exhibit a blocky, lamellar morphology. Interfaces between the **fcu** and **reo** domains are parallel to the {211} crystallographic planes.

In general, vacancy defects have a significant effect on the properties of UiO-66. On a molecular level, they affect the localisation of frontier orbitals, influencing the electronic and catalytic behaviour of the MOF [19]. On a macroscopic level, they affect the mechanical properties of the MOF, including the thermal expansion coefficient and the bulk modulus [3, 14]. Anomalous behaviour, such as negative thermal expansion or pressure-induced amorphisation, is more likely to occur in UiO-66 when it contains defective nanocells with different mechanical properties than the ideal, defect-free nanocell. Removing even one linker from a $2 \times 2 \times 2$ supercell of UiO-66 decreases the loss-of-crystallinity pressure from 1.8 GPa to 1.5 GPa [14]. The bulk modulus drops from 22 GPa to 20 GPa. Removing more

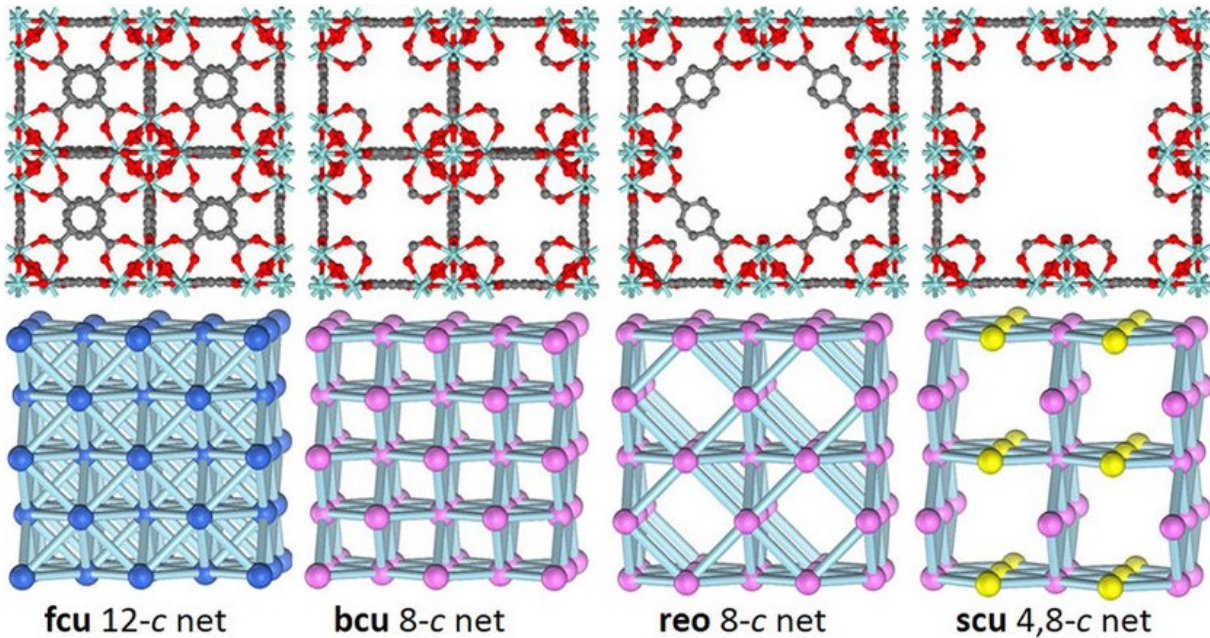


Figure 1.4: Four types of nanocells encountered in UiO-66(Zr), from most stable (**fcu**) to least stable (**scu**). Top row: the structural models of these four types. Bottom row: their topological networks. Figure reproduced from Ref. 20.

than one linker, potentially orienting the vacancies in the same direction, has an even stronger effect.

It stands to reason that these correlated defects can be exploited as a source of very useful functionalities. The philosophy of defect engineering, which has been a staple of solid-state physics for decades, can be applied to MOF research as well [15]. The most obvious property that can be modulated by controlling the concentration of missing cluster defects, is the sorption behaviour of the MOF [15, 18]. The defects of the **reo** topology are responsible for introducing pores with a diameter of approximately 1.7 nm in the crystal, significantly larger than the pores in the **fcu** topology. Furthermore, the spatial correlation of the missing cluster defects significantly increases the connectivity of the new pores, providing more and faster pathways for the diffusion of gases. Nitrogen gas adsorption isotherms show an increased uptake because of this mechanism [10, 18].

1.2.2 HKUST-1

The topic of spatial disorder in MOFs comprises more than the existence of correlated defect nanoregions in UiO-66. For instance, HKUST-1, a copper paddle-wheel based MOF, can be designed to contain mesopores in addition to its ever-present micropores [8]. These mesopores can be as large as 3.8 nm, much larger than a nanocell, and they are intentionally introduced to facilitate the diffusion of gases through the material. This hierarchical combination of micropores and mesopores, whereby gases are transported through the mesopores to the micropores, improves the adsorption performance of the

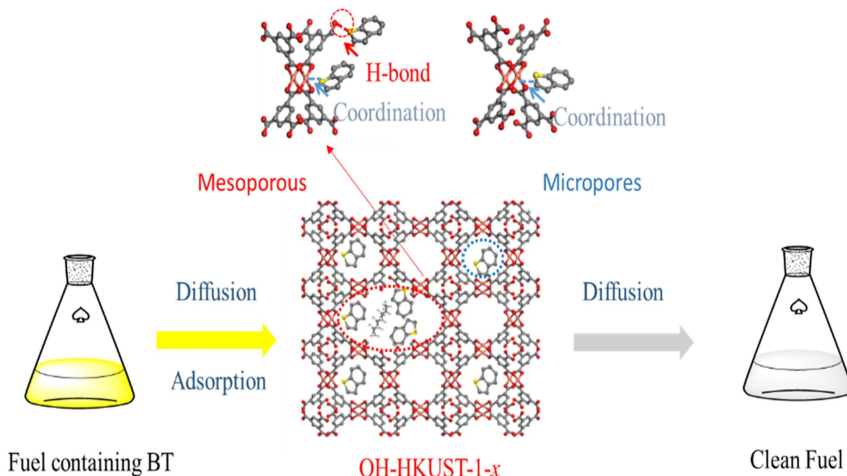


Figure 1.5: Illustration of the improved adsorption and removal of benzothiophene (BT) from fuel, owing to an engineered combination of mesopores and micropores in HKUST-1. Fuel diffuses easily through the mesopores of the MOF. Benzothiophene adsorbs on the internal surfaces of the MOF by means of coordination bonds and is effectively separated from the fuel. Figure reproduced from Ref. 8.

MOF significantly, as Figure 1.5 implies.

Aside from mesopores, HKUST-1 may contain other defects as well. Confocal fluorescence microscopy has been successfully applied to create three-dimensional images of defect planes in a HKUST-1 crystal. These defect planes originate as fractures on the outer {111} facets of the crystal and propagate through the bulk along the same family of {111} crystallographic planes [21].

1.2.3 MIL-53 and other pillared-layered MOFs

The phenomenon of phase coexistence is yet another example of correlated spatial disorder. Crystalline phases occupy entirely separate spatial domains, which is, inherently, a strongly correlated, long-range effect. MIL-53, among other flexible, pillared-layered MOFs such as MIL-47, DMOF-1(Zn) and CoBDP, can exhibit phase coexistence because of its unique winerack-structure [17, 22]. The inorganic clusters of MIL-53, which are often aluminium-based or chromium-based, are connected by benzenedicarboxylate (BDC) organic linkers [23]. The pores of MIL-53 are one-dimensional channels which can open or close depending on external thermodynamic stimuli, including pressure, temperature and guest adsorption. This large-amplitude structural transition between open pores and closed pores is often called *breathing* [22]. The breathing behaviour of MIL-53 implies that its atomic structure has two metastable states, corresponding to the phases of the crystal: a large or open pore state and a closed pore state. In other words, the atomic structure of MIL-53, captured in a single nanocell, is bistable. When the atomic structure transitions from the closed pore state to the open pore state, which is its most stable state at room temperature, it has to cross a free energy barrier.

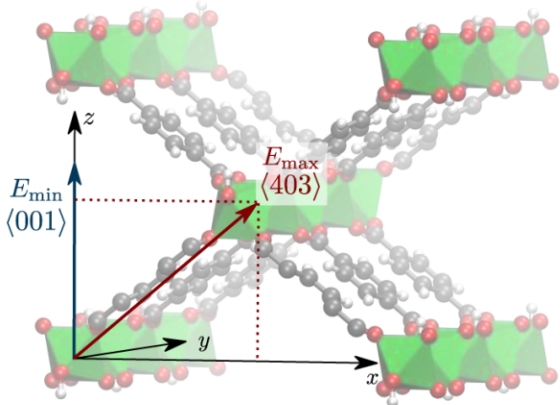


Figure 1.6: Atomic structure of MIL-53, a flexible MOF. The directions of the maximal and minimal anisotropic Young modulus are indicated. Figure adapted from Ref. 13.

In MIL-53, breathing was first observed in guest adsorption experiments, but it was later found that temperature, instead of guest adsorption, could be a driving factor for the transition as well [23]. Using inelastic neutron scattering to probe the low-energy phonons of the MIL-53 crystal, researchers were able to conclude that the temperature-driven transition between the open pore phase and the closed pore phase is reversible. Hysteretic behaviour was also observed in the results. An increase of the temperature to about 330 K was required to let the closed pores open, whereas a decrease to about 200 K was required to let the open pores close again.

In MIL-53 and in any of the other bistable, flexible, pillared-layered MOFs, a region of mechanical instability can be found between the two metastable states. In this region of mechanical instability, calculations of the material's compressibility or bulk modulus result in negative values [17, 22]. The closed pore phase and the open pore phase can coexist in this region, as depicted in Figure 1.7. Initially, this coexistence has to be triggered by a sudden change in the external conditions, such as a pressure quench in DMOF-1(Zn) or a temperature quench in MIL-53(Al) [22].

The mechanical description of a MIL-53 crystal where phase coexistence appears, is severely complicated by the fact that the elastic properties of the nanocell have to be defined in both of its metastable states separately. On top of that, these elastic properties are highly anisotropic due to the one-dimensional pores of the nanocell [17, 13]. It is worth noting that, besides a mechanical description, modelling the full spatiotemporal behaviour of a flexible MOF such as MIL-53 is very challenging [2]. Firstly, the simulation methods have to be adapted to the flexible nature of the MOF. Secondly, an accurate simulation has to take into account the size-dependent flexibility of the MOF [22]. Small, alternating domains of the open pore phase and the closed pore phase require a high free energy cost and suppress the MOF's flexibility, due to the interfacial defects they introduce. Larger domains require a lower free energy cost and preserve the MOF's flexibility.

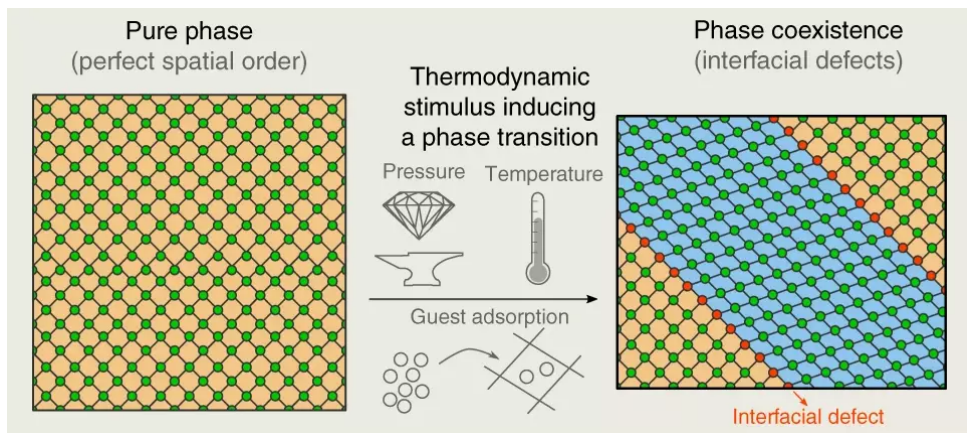


Figure 1.7: Schematic depiction of phase coexistence in MIL-53 and other pillared-layered MOFs, triggered by external thermodynamic stimuli. Figure adapted from Ref. 22.

1.3 Molecular modelling

1.3.1 Quantum mechanics

The physical behaviour of a molecular system is dictated by quantum mechanics, the highest level of theory in molecular modelling. Quantum mechanical (QM) methods, also known as *ab initio* methods, attempt to solve the Schrödinger equation. Density functional theory (DFT) and wavefunction-based methods, such as Hartree-Fock (HF), are the most common quantum mechanical methods. Figure 1.8 provides a general overview of molecular modelling methods [6].

The wavefunction of a molecular system depends on the Cartesian coordinates and spin coordinates of its constituent nuclei and electrons. The nuclear spin coordinates can often be neglected. Additional simplifications can be introduced by neglecting all relativistic effects and by assuming a time-independent potential energy function. The wavefunction is then the solution of the time-independent Schrödinger equation.

For nearly all systems, the time-independent Schrödinger equation has to be solved numerically to obtain the wavefunction, or at least an approximation thereof. The ideal strategy to prepare this partial differential equation is a separation of variables, namely a separation of the nuclear coordinates and the electronic coordinates. By applying this separation of variables, the wavefunction can be split into an electronic part and a nuclear part. With the assumption of infinitely heavy, clamped nuclei, the Schrödinger equation decouples into an electronic eigenvalue problem and a nuclear eigenvalue problem, from which, respectively, the electronic and nuclear energy levels can be extracted. If the electronic energy levels are well-separated and if their dependence on the nuclear coordinates varies slowly (adiabatically), then it is possible to calculate the electronic energy levels for each configuration of the nuclei. This is the Born-Oppenheimer approximation [2, 24].

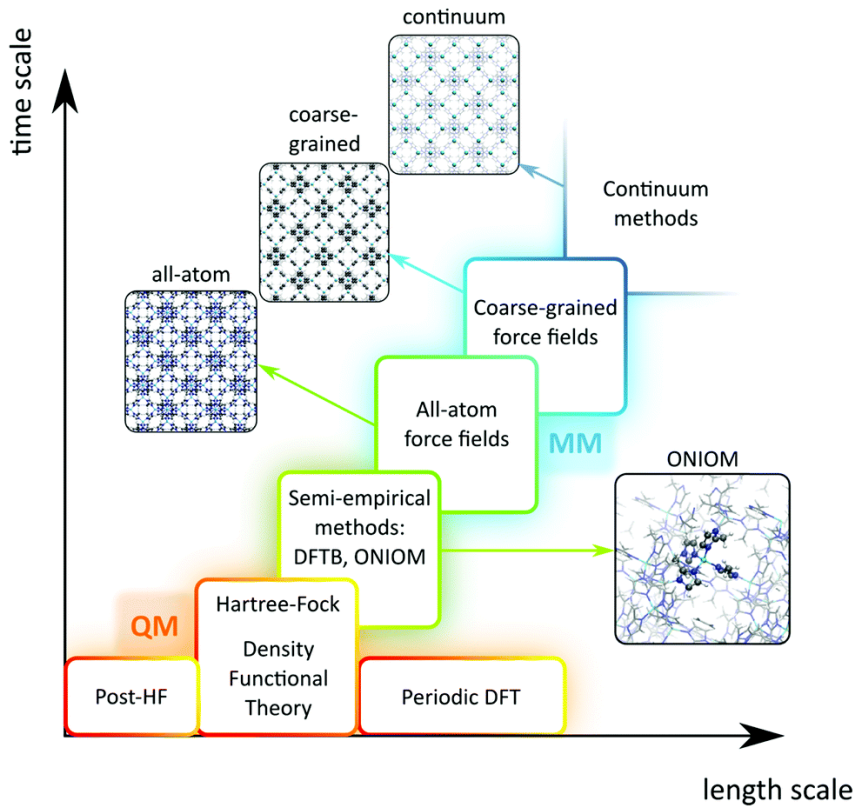


Figure 1.8: Schematic overview of molecular modelling methods, going from a high level of theory (quantum mechanics) to lower levels of theory (molecular mechanics and coarse-grained methods). Figure reproduced from Ref. 6.

As implied in the Born-Oppenheimer approximation, the ground state electronic energy is a function of the nuclear coordinates. Here, the concept of the potential energy surface (PES) is introduced. The PES is the sum of the ground state electronic energy and the electrostatic potential energy of the nuclei [2]. At a temperature of nearly 0 K, a molecular system typically has negligible kinetic energy and is therefore stuck in its ground state. The PES is then, fundamentally, the only tool needed to describe every configuration of the molecular system. The free energy surface (FES), which is often used to derive thermodynamic properties, is, conceptually, the extension of the PES to finite values of temperature and pressure. At finite temperatures, vibrational, rotational and possibly electronic excited states are unlocked. The availability of many new energy levels and the increasing number of degrees of freedom start to play a role in the behaviour of the molecular system. Due to the increase of the internal energy and the increasingly important contribution of entropy, the FES at finite temperatures no longer coincides with the PES.

Aside from thermodynamic properties, the PES can also be used to derive the time evolution of the molecular system. A molecular dynamics (MD) simulation is able to track the molecular system in time by treating its constituent atoms, or atoms that have been grouped into beads, like classical particles

that obey Newton's equations of motion. In the absence of external fields, such a particle is subject to a force, equal to the negative gradient of the PES with respect to the particle's Cartesian coordinates. The equations of motion are then numerically integrated, usually with the second-order accurate velocity Verlet algorithm, to obtain the trajectory of each particle [25]. If the molecular system satisfies the ergodic hypothesis, then its macroscopic properties, such as its bulk modulus or its heat capacity, can be estimated by time averaging the appropriate quantities derived from the particles' trajectories.

For an MD simulation, it does not matter how the PES is derived, as long as it is a function of the particle's coordinates and differentiable. If the PES is evaluated by calculating the electronic ground state energy and the electrostatic potential energy of the nuclei at each point in time, then the method is called *ab initio* molecular dynamics (AIMD) [24]. Unfortunately, the PES of a large system, such as a MOF or a large protein, has to be evaluated in a high-dimensional space of nuclear coordinates. Sampling in this space is very computationally demanding. For each configuration of nuclei, the ground state energy level has to be calculated. However, calculating the ground state energy is already complicated due to the large number of electrons in the system and the unfavourable scaling of the self-consistent field cycles and matrix operations involved in the *ab initio* calculations [26]. These computational limitations restrict AIMD simulations of large systems to picosecond time scales.

1.3.2 Molecular mechanics

With molecular mechanics (MM), simulating a MOF can be simplified and extended to longer time and length scales. Molecular mechanics is built on the foundation of force fields. In a force field, the electronic coordinates are completely neglected in favour of an all-atom (AA) description of the molecular system, also known as an atomistic description [6]. The PES of a force field, sometimes simply called 'the force field', is approximated as a sum of parametrised analytical functions, representing bonded interactions and non-bonded interactions. The bonded interactions are modelled as a sum of two-body, three-body, four-body and potentially even more complicated many-body interactions between atoms. Instead of Cartesian coordinates, internal coordinates such as bond lengths, angles, dihedral angles and out-of-plane distances are introduced as variables in this expansion. Thanks to these intuitive internal coordinates, the functional form of a force field is very interpretable. The individual terms of the bonded interactions are usually harmonic potentials with respect to the internal coordinates. The non-bonded interactions comprise van der Waals interactions and electrostatic interactions. In the QuickFF methodology, the van der Waals interactions are modelled with a Lennard-Jones potential or a Buckingham potential [27]. The electrostatic interactions are Coulomb potentials between point charges or charge densities. Many extensions of these functional forms exist, including reactive potentials and multipole electrostatic interactions.

Atomistic force fields do not start from first principles, so they have to be fitted. There exist a bottom-up approach to fitting a force field and a top-down approach [2]. In the bottom-up approach, the force field is fitted to *ab initio* results. The parameters of the bonded interactions are tuned such that the PES of

the force field matches the PES of the *ab initio* calculations as closely as possible. The distances between atoms in the atomic structure or the frequencies of normal modes can be used as fitting criteria [27]. In MOFs, even the elasticity tensor of the nanocell can be used as a fitting criterion [28]. In the top-down approach, the force field is fitted to experimental results. It is worth noting here that some force fields do not require fitting and can be used just as they are, as they are intended to be transferable and their parameters are tabulated.

In the bottom-up approach, the PES of the force field and the PES of the *ab initio* calculations should coincide up to an unimportant constant, but the PES of the force field is much faster to evaluate because of its analytical or tabulated nature. Ultimately, that is the advantage of force fields. If the electronic structure of the molecular system does not matter explicitly and if accuracy is not a priority, then force fields are the best way to model large atomic systems. They typically allow for MD simulations of large systems up to nanosecond time scales [2].

Despite their computational advantages, force fields are still not efficient enough to accurately model correlated spatial disorder and cooperative phenomena in MOFs or other large systems [29]. A defect, for instance, may be contained within a large simulation domain and it may be computationally feasible to run this simulation, but the effect of periodic boundary conditions has to be considered. The influence of the defect may reach very far beyond the edges of the simulation domain. In practice, there is often no way to isolate the defect from its periodic images with conventional methods [11].

Fortunately, there exist other methods in the realm of molecular mechanics that push the limits of molecular modelling even further. These are very low levels of theory, located in the top right-hand corner of Figure 1.8. Coarse-grained force fields attempt to reach length scales of several tens of nanometers. In Chapter 2, they will be discussed in detail. The micromechanical model, the subject of Chapter 3, is also a coarse-grained force field. The micromechanical model can be based on atomistic force field simulations as well as *ab initio* data and experimental observations. Additionally, there are continuum methods. These methods view a MOF as a continuous medium on a length scale of hundreds of nanometers, up to macroscopic length scales, but will not be discussed in this thesis.

1.4 Goal

The goal of this work is twofold. Primarily, we want to prove the validity of the micromechanical model as a new coarse-grained method in the modelling of metal-organic frameworks. That includes (i) validating the proposed equations of motion for the coarse-grained nodes, (ii) testing our implementation using optimisations and MD simulations in different ensembles and (iii) verifying the consistency and accuracy of the results. The first two objectives are technical in nature. They can be met by only considering a test system, which we can also use to investigate the computational complexity of the model and the efficiency of our implementation. The third objective, however, depends on each practical system

we attempt to simulate.

As part of our validation strategy, we consider a small homogeneous system, for instance a $2 \times 2 \times 2$ or $3 \times 3 \times 3$ grid of nanocells with identical elastic properties. From an MD simulation, the equilibrium cell matrix and the elasticity tensor of this micromechanical system can be determined. The elastic properties of the system can then be compared to the results of *ab initio* methods or atomistic force fields, applied to either a single nanocell or to a $2 \times 2 \times 2$ or $3 \times 3 \times 3$ supercell. Considering that the micromechanical model is based on the elastic properties of individual nanocells, it should at least provide a consistent prediction for the elastic properties of a homogeneous system, which only contains one type of nanocells. Whether this prediction is accurate, however, depends on the system and must be investigated. In other words, we must attempt to keep track of the information that is lost due to coarse graining, as detailed in Section 3.4.

Secondly, our aim is to demonstrate the effectiveness of the micromechanical model. As we will discuss in Chapter 3, the model presents many opportunities to investigate cooperative and correlated phenomena in metal-organic frameworks, such as the existence of correlated missing cluster defects in UiO-66 [3] or the coexistence of a large-pore phase and a closed-pore phase in MIL-53 [13]. The case study of UiO-66 is an opportunity to demonstrate the effectiveness of the model, in several different ways.

In concrete terms, we want to calculate the bulk modulus and other elastic properties, potentially even the thermal expansion coefficient, of MOFs such as UiO-66 and MIL-53 on a length scale of tens or hundreds of nanometers. The increased length and time scale of the model could allow for efficient MD simulations of finite or periodic crystals consisting of tens, hundreds or thousands of nanocells. Ultimately, we want to attain length scales that are comparable with experiments. In the future, we hope to use experimental data as an additional validation strategy for the model, effectively bridging the gap between the atomic and macroscopic level. Perhaps most importantly, macroscopic properties such as the bulk modulus and the elastic properties can be calculated as a function of varying concentrations and configurations of spatial disorder. By varying, for instance, the concentration and connectivity of defective **re**o nanocells in UiO-66, the bulk modulus of the MOF could change significantly. Similarly, these simulations can provide valuable insight into the limits of mechanical stability when engineered defects, perhaps for the purpose of adsorption, are introduced in a rigid MOF like UiO-66.

1.5 Outline

This introduction, Chapter 1, serves to provide the reader with a clear understanding of the context of this work. Metal-organic frameworks are introduced as the subject of our simulations. Examples of spatial disorder in MOFs are listed: defect nanoregions in UiO-66, mesopores in HKUST-1, and phase coexistence in MIL-53. Further experimental evidence is cited for the presence of defects in UiO-66. It is explained why common techniques in molecular modelling do not reach the scale of these cooperative

and correlated phenomena, potentially failing to accurately predict the macroscopic properties of the material.

In Chapter 2, we will discuss in detail the need for coarse graining in molecular modelling and materials design. Coarse graining offers a solution to surpass the computational limits of atomistic force field simulations. Several strategies to construct coarse-grained force fields are listed and briefly explained. Finally, one example of a coarse-grained MOF from scientific literature is analysed.

Chapter 3 deals with the micromechanical model. The reader will be acquainted with our novel coarse-grained approach as we explain the core concept of the model. First and foremost, that includes the introduction of nanocell types and of coarse-grained nodes located on the vertices of a nanocell. The strength of the interaction between two nodes is determined by the elastic properties of the nanocells between the nodes. Following a short description of these elastic properties and notes on how to obtain them, we proceed to derive the equations of motion of the coarse-grained nodes. An important distinction is made between unistable and bistable nanocells. Bistable nanocells require an extension of the equations of motion, whereby both metastable states of the nanocell provide a weighted contribution to the force acting on its nodes.

Chapter 4 is a natural extension of Chapter 3 and explains the important features of our implementation of the micromechanical model, which we have named MicMec. Additionally, we perform several tests of the implementation and of the model in general with a test system.

The main topic of Chapter 5 is UiO-66, a MOF which may contain cluster and linker defects as discussed previously. The goal of this case study is to calculate and study the elastic properties of a micromechanical system containing UiO-66 nanocells, some of which contain defects. In a set of eight simulations, the defective nanocells are grouped according to different configurations. Lastly, this case study also provides a comparison between the results of an atomistic force field simulation and the results of a micromechanical simulation.

The results of this work are briefly summarised in the final chapter, Chapter 6. A final verdict is cast on the micromechanical model, based on its performance in the validation procedure and the case study of UiO-66. Some suggestions for further research and use of the model are offered.

2

Coarse graining

Reality is governed by the laws of physics on all time and length scales. Our descriptions of reality, however, often fail to bridge the gaps between length scales. Coarse graining attempts to bridge these gaps, to reconcile models based on different length scales and to accurately and efficiently incorporate small, well-defined systems into larger systems.

2.1 Introduction

One of the primary reasons to apply coarse graining is the inherent multiscale nature of many problems in physics. Nanoelectronic devices, materials complexes and even biological systems possess a hierarchy of features on different length scales [30]. More often than not, it is redundant and even computationally infeasible to include all small-scale features in a simulation or in an analytical model. Bottom-up coarse graining offers a solution, by averaging the effects of the small features and upscaling them to match the large features. In the context of coarse-grained force fields, the bottom-up approach starts by sampling an atomistic free energy surface, *i.e.*, by determining the effect of small features (atoms) on the molecular system [2, 11]. A top-down approach relies on the tuning of model parameters to match experimental observations. In this thesis, only bottom-up coarse graining methods will be discussed.

Another reason to apply coarse graining, aside from our scientific curiosity, is the existence of long-

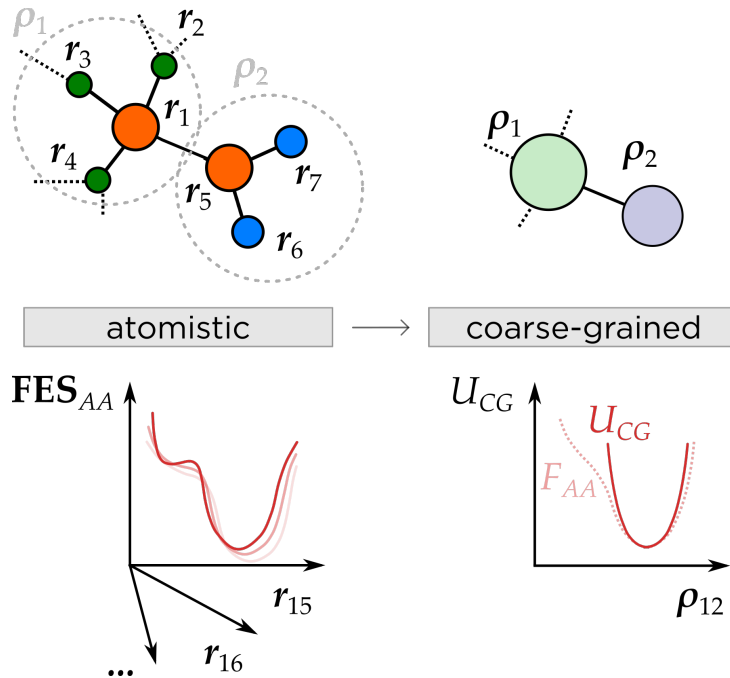


Figure 2.1: Schematic illustration of an arbitrary atomistic force field being coarse-grained. Due to the reduction in the number of degrees of freedom, the dynamics of the coarse-grained representation can be smoother than those of the all-atom representation.

range correlated spatial disorder [11, 15]. Spatial disorder in itself, regardless of long-range correlation effects, is enough to warrant the use of coarse graining. In fact, most materials contain some measure of spatial disorder or some type of heterogeneity, due to their large number of internal degrees of freedom. Even if the local behaviour of a material is well-known and its structure on a small scale exhibits perfect order, spatial disorder may still appear on a larger scale in the form of defects, impurities, pores, surfaces or phase boundaries. The material may retain its functionality despite this spatial disorder, but in many cases its macroscopic properties, especially its mechanical stability, will be affected [13, 14]. Therefore, it is necessary to include all types of spatial disorder in the simulation domain, if an accurate prediction of the macroscopic properties of the material has to be achieved. In a finite crystal, the simulation domain may have to cover the entire crystal to account for finite-size effects.

Expanding the simulation domain comes at a computational cost, which quickly becomes unacceptable in the case of *ab initio* methods. Doubling the sides of a three-dimensional simulation domain with periodic boundaries, for instance, leads to an eightfold increase in the number of atoms. The computational complexity of Hartree-Fock and DFT scales with the number of atoms raised to the power four, resulting in a calculation that is about four thousand times more demanding than the original calculation [26]. Atomistic force fields are less problematic, but are still insufficient to efficiently model molecular systems with a spatial extent of tens of nanometers, *i.e.*, containing hundreds or thousands of atoms [2]. In this situation, coarse-grained force fields can significantly reduce the complexity of the simulation,

at the cost of a loss of structural information and a loss of resolution in the free energy surface, both of which are demonstrated schematically in Figure 2.1.

2.2 Coarse-grained force fields

Due to the current limits of classical computing and the unfavourable scaling of higher levels of theory, coarse-grained force fields have become increasingly useful for large systems, especially for nanoporous materials, such as metal-organic frameworks, and large organic molecules, such as proteins, polymers and membranes. The construction of a coarse-grained force field and its subsequent application are typically performed in three steps, although most methods do not explicitly specify a mapping [30].

1. Mapping the atoms to coarse-grained beads or sites.

Starting from an all-atom (AA) description of the molecular system, a mapping usually results in a reduction of the number of variables by about one order of magnitude and a computational speed-up.

$$\mathbf{r}(\text{AA}) \rightarrow \rho(\text{CG}) \quad (2.1)$$

An example of such a mapping is shown in Figure 2.1. Naturally, any mapping from a high-dimensional space to a low-dimensional space comes with a trade-off. The spatial resolution of the coarse-grained system is notably lower than the spatial resolution of the atomistic system. Any single configuration of the coarse-grained system can correspond to many different configurations of the atomistic system.

2. Defining the interactions between the coarse-grained beads.

If we assume the previous mapping to coarse-grained coordinates to be consistent in configuration and momentum space [31], then the effective interactions between the beads are determined by the free energy surface of the atomistic system. The effective interactions between the beads are the result of the collective interactions between atoms in many different configurations. In other words, the coarse-grained coordinates are introduced as collective variables in the atomistic system. A single value of the collective variable ρ can correspond to many different configurations \mathbf{r} of the atomistic system.

$$\text{FES}_{\text{AA}}(\mathbf{r})|_{T,V,\dots} \rightarrow F_{\text{AA}}(\rho)|_{T,V,\dots} \quad (2.2)$$

All of the atomistic variables, *i.e.*, the coordinates of the atoms, are integrated out of the system in favour of the collective variables, which results in a smoother free energy surface $F_{\text{AA}}(\rho)$. Then, the coarse-grained force field is fitted to $F_{\text{AA}}(\rho)$, potentially resulting in an even smoother function.

$$F_{\text{AA}}(\rho(\mathbf{r}))|_{T,V,\dots} = U_{\text{CG}}(\rho)|_{T,V,\dots} \quad (2.3)$$

The coarse-grained force field acts as the potential energy of the coarse-grained system, but it is not necessarily defined at 0 K because it was fitted, in general, to a free energy surface. It is inherently state-dependent. Therefore, the term ‘potential energy surface’ should not be used for $U_{CG}(\rho)$, simply to avoid confusion with the PES of an atomic structure, which is always defined at 0 K. As a side note, it is unlikely that the FES of the atomistic system can be fully determined. Depending on the number of coarse-grained coordinates, even the smooth free energy surface still exists in a high-dimensional space that is computationally demanding to sample and possibly not even fully accessible due to high free energy barriers.

3. Performing a simulation with the coarse-grained beads.

As soon as an approximation for the exact interactions between the beads has been established, MD simulations on the coarse-grained level can be performed. The results can be validated with *ab initio* data, with atomistic force field simulations or with experimental data.

Several methods exist that implement these steps, each focusing on different aspects of the coarse graining concept and different criteria to construct and optimise the coarse-grained force field. We provide a short overview of a few methods, including MARTINI force fields, iterative Boltzmann inversion, force matching and relative entropy minimisation.

2.2.1 MARTINI force fields

MARTINI force fields are the prototypical example of coarse-grained force fields. They were initially developed to study lipid membranes and were later applied to other bio-molecules and polymers. In the MARTINI methodology, a 4 : 1 mapping of heavy (or non-hydrogen) atoms to beads is proposed, as shown in Figure 2.2, although there exist variations on this theme [32]. Hydrogen atoms are always neglected. The bonded interactions of the coarse-grained beads are determined by proposing an *ad hoc* analytical form. This is essentially a new force field with beads instead of atoms. The parameters of the force field are fitted to the results of the all-atom force field simulations, typically by matching optimised geometries or by attempting to reproduce experimental free energies. The non-bonded interactions between the beads are represented with a Lennard-Jones potential of variable strength depending on the type of the beads (charged, polar, non-polar or apolar). Charged beads interact with each other through a shifted Coulomb potential, taking into account the relative permittivity of the medium.

2.2.2 Iterative Boltzmann inversion

Iterative Boltzmann inversion, or reverse Monte Carlo, was initially developed to calculate accurate pair potentials in solutions [34]. The goal of Boltzmann inversion is to reconstruct the interaction potentials of a molecular system from radial distribution functions (RDFs). This is the reverse problem of statistical mechanics: to approximate the Hamiltonian of the system (the interaction potentials) from an available

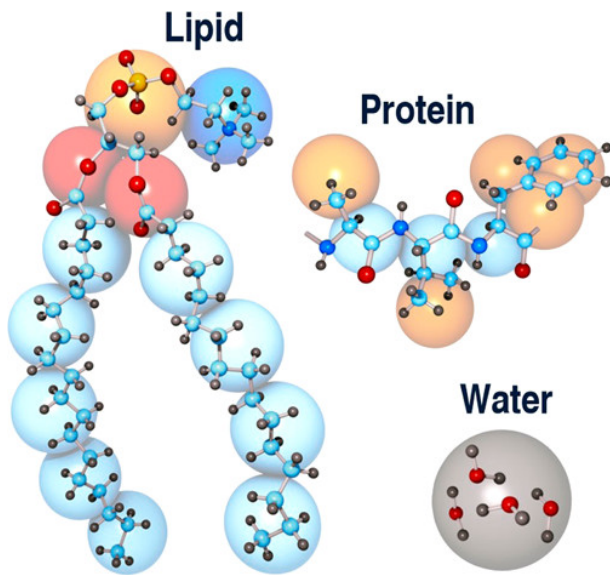


Figure 2.2: Illustration of the 4 : 1 MARTINI approach to coarse-grained mapping. Light atoms, like hydrogen atoms, are neglected, in the assumption that the remaining heavy atoms dominate the dynamics of the molecule. Figure reproduced from Ref. 33.

set of canonical averages (the RDFs). In each iteration of the Boltzmann inversion procedure, the non-bonded interactions of the coarse-grained force field are updated with a correction from the RDFs. The bonded interactions are updated with a correction from the distributions of bond lengths, bending angles and dihedral angles. This process is continued until the corrections are negligible. The iterative Boltzmann inversion procedure does not specify a mapping or an analytical form for the interaction potentials.

The inversion algorithm, as originally proposed, does not take into account multiple target thermodynamic states. Like other coarse-grained force fields, the algorithm constructs an inherently state-dependent potential, which is only truly valid at one point in the thermodynamic state-space. However, more recent developments have been successful in extending the algorithm such that it allows for multi-state optimisation [35]. The extended algorithm constructs a self-consistent potential that converges for multiple target states simultaneously, covering a wider region of the thermodynamic state-space.

2.2.3 Force matching

Force matching is also known as the multiscale coarse graining (MS-CG) approach [31]. It relies on a least-squares fitting to minimise the differences between the all-atom forces and the coarse-grained forces [36]. The force matching procedure does not specify a mapping, but it does impose consistency restrictions on the mapping.

2.2.4 Relative entropy minimisation

The relative entropy is a powerful statistical measure for how closely a model system (the coarse-grained force field) resembles a target system (the atomistic force field) [37]. Once more, the analytical form of the coarse-grained force field is unspecified, yet assumed to be parametrised. By minimising the relative entropy between the coarse-grained force field and the atomistic force field, with respect to the parameters of the coarse-grained force field, optimal values for these parameters can be found. As a final consequence of the minimisation, the probability distribution of the ensemble of coarse-grained configurations, either in the coarse-grained description, or in the all-atom description, is preserved.

2.3 Coarse graining MOFs

At the time of writing, scientific literature on the development or application of coarse-grained force fields for MOFs is rare and often limited in scope. We can cite several reasons why this area of research is so unexplored. Firstly, it is a rather new concept to apply coarse graining to MOFs, enabled only now by the continued growth of academic and industrial interest in MOFs. The past decade has seen only a few computational studies exploring coarse-grained force fields for MOFs, notably Ref. 11 and Ref. 38.

Secondly, much of the interest in MOFs is related to their chemical composition and their atomic structure on the scale of a single nanocell, both of which do not require coarse graining techniques. However, we have demonstrated several cases, such as multiscale problems or molecular systems containing disorder of a large spatial extent, where it is necessary, at least within the current computational limits, to perform some type of coarse graining.

Thirdly, MOFs present unique challenges to model. Most atomistic force fields for MOFs are system specific instead of transferable. Generic, rule-based force fields are transferable, but often cannot reproduce the anomalous behaviour of MOFs, such as negative thermal expansion and the previously mentioned breathing effect [11]. System specific force fields attempt to emulate the atomic interactions which, on a quantum mechanical level, give rise to the MOF's anomalous behaviour. Including all necessary atomic interactions in the force field and finding the best criteria for its fitting procedure can be a difficult process, especially for a flexible MOF with a large unit cell and a high degree of diversity in its atomic structure and chemical composition. The difficulty in constructing atomistic force fields for MOFs translates to coarse-grained force fields, especially if the coarse-grained model has to preserve the anomalous behaviour of the MOF as well. Coarse-grained force fields are often even more application-driven and system specific than atomistic force fields, because of their use in materials complexes and multiscale problems.

The authors of Ref. 11 have investigated a general methodology to construct coarse-grained force fields for MOFs. Within this methodology, the MOF is represented as a framework of connected coarse-

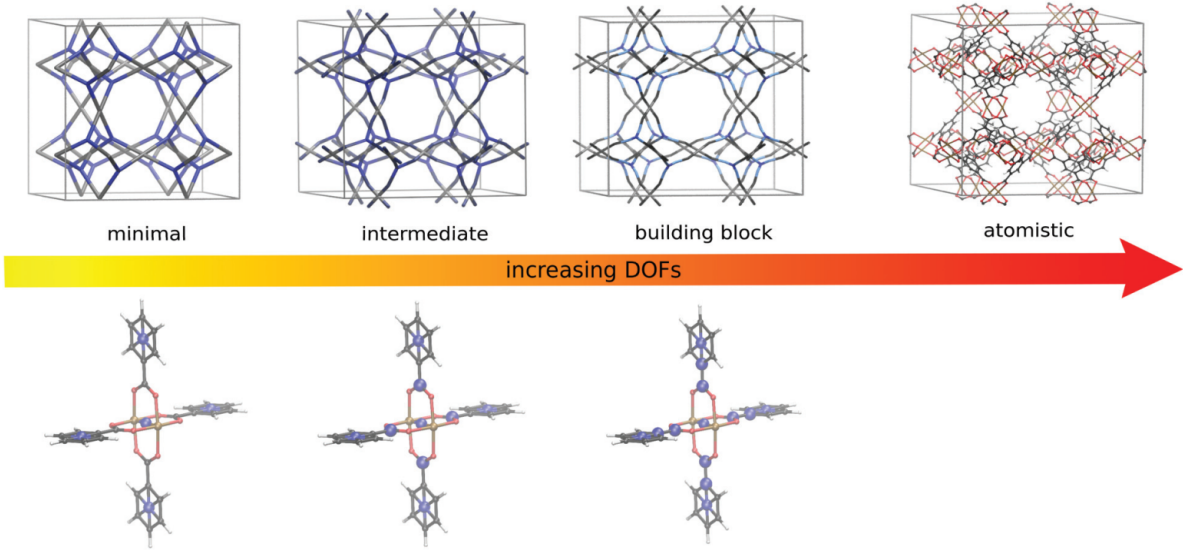


Figure 2.3: Levels of coarse graining of HKUST-1, from the minimal model with only fifty-six beads (few degrees of freedom) to the fully atomistic representation (many degrees of freedom). HKUST-1 contains paddle-wheel structures, which are shown repeatedly below the coarse-grained models. Each paddle-wheel consists of a different mapping of coarse-grained beads. These coarse-grained beads, coloured blue, are defined as centres of mass of several atoms in their vicinity. Figure reproduced from Ref. 11.

grained beads, similar to how steel beams connect the nodes of a mechanical truss. The prototypical system under investigation is HKUST-1, a copper paddle-wheel based MOF which has been discussed in Section 1.2.2.

The concept of a mechanical truss leaves a significant amount of freedom in choosing the best representation of the MOF. Depending on the number of remaining beads, the HKUST-1 nanocell can be more or less coarse-grained. The reverse topological approach (RTA) prescribes that it is best to start from the most coarse-grained representation, also called the minimal model, to construct more detailed coarse-grained models. The minimal model corresponds exactly to the underlying topology of HKUST-1, the **tbo** net, and consists of only fifty-six beads per unit cell. It is shown, along with other less coarse models, in Figure 2.3.

We must note here that the minimal model is not necessarily the most coarse representation of the HKUST-1 nanocell. Our coarse-grained approach, the micromechanical model, can represent the nanocell with only eight shared beads in a simulation with periodic boundary conditions.

The authors proceeded to fit their minimal model to a reference atomistic force field, although it is in principle possible to fit the coarse-grained model to *ab initio* data as well. The optimisation of the coarse-grained parameters was performed by means of a genetic algorithm, using a single objective function based on mean square deviations of structure and curvature information. This is entirely

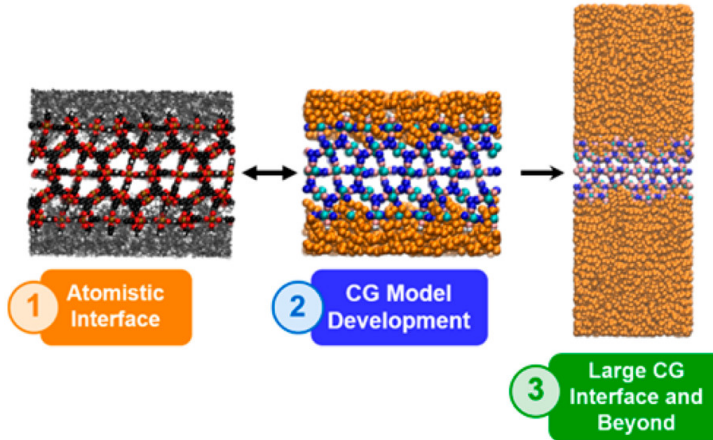


Figure 2.4: Schematic overview of a coarse graining strategy developed for an interface between HKUST-1 and polyvinyl alcohol. Figure reproduced from Ref. 38.

similar to conventional bottom-up approaches to determine atomistic force field parameters, whereby both the structure of the molecular system and its normal mode frequencies play a role. We must note that the coarse-grained force field was fitted and validated locally, not considering the entire nanocell. The MOF's building blocks, including the paddle-wheel structure shown in Figure 2.3, were used as reference structures. This has the obvious advantage that other MOFs containing the same building blocks can use the same coarse-grained force field as HKUST-1, adding a small degree of transferability to the otherwise system specific coarse-grained force field.

The minimal model employed many of the same potential energy expressions as the reference force field, however some expressions had to be adapted in order to reproduce the correct bending modes. In addition, the non-bonding terms had to be adapted as well. Dispersive attraction can be modelled as the summed effect of all atoms mapped to a single bead, but repulsive interactions are mainly determined by the outermost atom of a bead. This immediately demonstrates the need to choose coarse-grained interactions carefully.

The minimal model of HKUST-1 was able to reproduce its mechanical properties, such as its directional Young moduli and its bulk modulus, within a semi-quantitative accuracy of 10%. However, its negative thermal expansion was not reproduced. In HKUST-1, the translation and libration motion of the benzyl rings of its organic linkers and the local twisting of the paddle-wheel units are the main cause of its negative thermal expansion. In the minimal model, a benzyl ring is represented by only one bead and as such, it cannot reproduce these modes.

An important advantage of the bottom-up coarse graining strategy of Ref. 11 lies in its flexibility. While the result of the coarse graining procedure is undoubtedly a coarse-grained force field, its reference does not need to be an atomistic force field. If a higher accuracy is required, then its reference can be the *ab initio* data of the MOF, at the cost of a more demanding fitting procedure. Moreover, the level of

coarse-graining can be chosen freely through the mapping, as shown in Figure 2.3.

An example of the coarse-grained force field for HKUST-1 being used in practice, is discussed in Ref. 38. This computational study revolves around a multiscale interface between a MOF, HKUST-1, and a polymer, polyvinyl alcohol. Such a system is also known as a mixed matrix membrane. In the reference atomistic system the MOF layer is sandwiched between two sufficiently thick polymer layers to avoid interactions of the MOF layer with its periodic images, as shown in the first step of Figure 2.4.

Whether these polymer layers can adhere to the MOF layer is of special interest to researchers. In the worst case scenario, the polymer molecules are not compatible with the MOF and small voids appear at the interface, leading to a deterioration of the membrane's mechanical stability and its gas separation performance. A compatible polymer tends to penetrate into the open pores of the MOF layer and causes no voids. Additionally, the presence of the MOF layer influences the density profile of the polymer molecules. Inside the MOF layer, the density profile should vanish. Far away from the MOF layer, the density profile should tend to its bulk value. Near the MOF layer, the density profile should oscillate as a function of distance to the interface. That result, however, can only be determined from a coarse-grained model, as the density profile spans several nanometers, requiring a large simulation domain that contains thousands of atoms. A coarse-grained model can reach these longer length scales efficiently, while more detailed effects in the immediate vicinity of the interface can be observed using an atomistic force field or even using *ab initio* calculations. Hence, this is a multiscale problem.

The main steps to construct the coarse-grained model of Ref. 38 are listed in Figure 2.4. At first, a reference atomistic system was constructed. In this development stage, microscopic features such as the interaction sites between the polymer molecules and the MOF, or the surface coverage of the polymer layers, were investigated. Then, an equally sized coarse-grained system was constructed. The atoms of both the MOF and the polymer were mapped to beads, but not with the same level of coarse graining. Several radial distribution functions, as well as the density profile of polymer molecules inside the MOF were used as additional fitting criteria to optimise the strength of the interactions between the MOF and the polymer molecules. The other coarse-grained force field parameters, pertaining to interactions within the MOF or within the polymer, were optimised separately and combined in the end result. In the final step, the model was used in the previously mentioned, larger simulation to obtain a full density profile of the polymer molecules. The expected, oscillating behaviour was demonstrated. It was concluded that polyvinyl alcohol, the polymer being investigated, was indeed compatible with HKUST-1, the MOF being investigated.

2.4 Conclusions

Despite the rarity of computational studies regarding coarse-grained force fields for MOFs, a few investigations have been promising. Notably, the coarse-grained force field proposed in Ref. 11 was able to reproduce the mechanical properties of HKUST-1 with semi-quantitative accuracy and Ref. 38 was able to demonstrate the application of that coarse-grained force field to a multiscale problem. Both examples are still limited in scope however, dealing only with one MOF or one specific multiscale application. Research into coarse-grained force fields for MOFs needs to keep pace with the development of MOF design, by branching out to, for instance, flexible MOFs or interfaces between MOFs and other materials. Furthermore, future research should attempt to reach length scales beyond 10 nm, to accurately capture certain types of spatial disorder, *e.g.*, phase coexistence [29], and to further bridge the gap between molecular modelling and experimental data.

3

The micromechanical model

The micromechanical model is a novel approach to construct coarse-grained force fields in MOFs [29]. Starting from a grid of nanocells, we introduce massive, coarse-grained nodes on the vertices of each nanocell in the grid. The result of this mapping procedure is a network of interacting, coarse-grained nodes, governed by a set of analytical equations of motion. Motions in the network represent local or long-range elastic deformations in the MOF. Using this unique representation of elastic deformation, we attempt to simulate the mechanical behaviour of the MOF, investigating in particular the effect of correlated spatial disorder on its macroscopic properties.

3.1 Concept

The micromechanical model is based on the prerequisite that a metal-organic framework, or any similarly structured material, can be divided into nanometer-scale building blocks. We refer to these building blocks as nanocells. A defect-free, infinitely extending MOF is defined by only one type of nanocell, a periodically repeating unit cell which contains the MOF's entire atomic structure. The *type* of a nanocell, as we define it, is (i) determined by its atomic structure and (ii) uniquely represented by its equilibrium elastic properties. MOFs contain different types of nanocells as a consequence of (potentially correlated) spatial disorder. If a structural defect causes a nanocell to have different elastic properties than the ideal, defect-free unit cell of the MOF, then that nanocell should be classified as

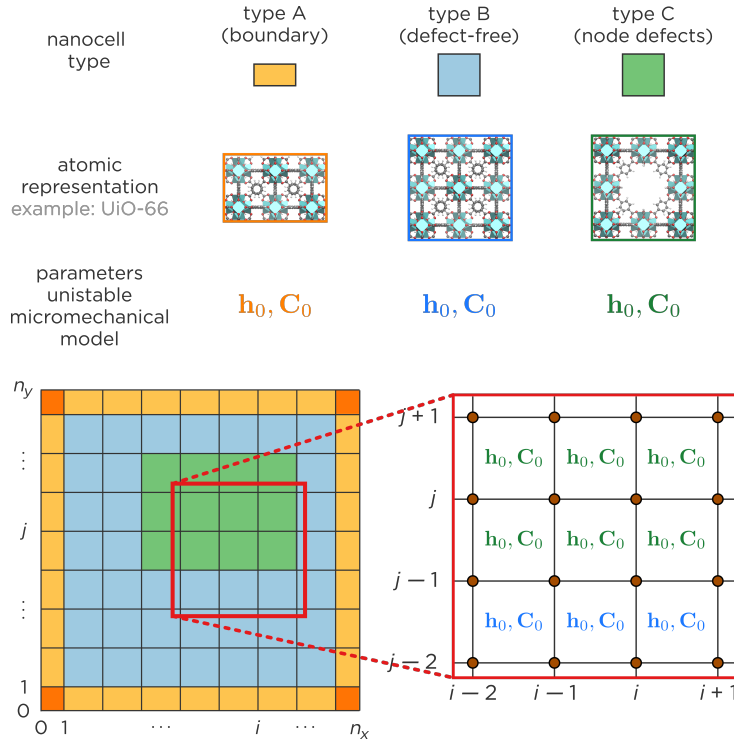


Figure 3.1: Schematic overview of a finite micromechanical system, applied to UiO-66. The grid of nanocells contains three different types of nanocells. In the zoomed-in window, the micromechanical nodes are shown. The micromechanical parameters \mathbf{h}_0 and \mathbf{C}_0 are the equilibrium cell matrix and elasticity tensor, respectively. These are coloured differently for different nanocell types and adopt different values, accordingly. Figure adapted from Ref. 29.

a different type than the ideal, defect-free unit cell. Similarly, a nanocell located at a surface or at an interface could have sufficiently distinct elastic properties to be defined as its own type.

Importantly, the elastic properties of a nanocell are determined from its equilibrium atomic structure, *i.e.*, its most stable, energetically most favourable, state for a certain set of thermodynamic conditions. However, some nanocells have two metastable states, separated by a free energy barrier. These metastable states are local minima of the free energy surface. Hence, these *bistable* nanocells also have two different sets of elastic properties, one for each local minimum. A bistable nanocell should therefore be regarded as two types in one nanocell, each type corresponding to one of its metastable states and one set of elastic properties.

Our discussion of spatial disorder in MOFs (Section 1.2) has provided ample proof for the existence of several different types of nanocells. UiO-66, for instance, contains one defect-free type, which adopts the **fcu** topology, but may contain other types as well, with structural defects. The other types can be classified using the **bcu**, **reo** and **scu** topologies. At a surface or at an interface, the nanocells of UiO-66 may also belong to a different type, as illustrated in Figure 3.1.

Having established the concept of nanocell types, we can outline the micromechanical model in further detail. There are four main steps in the micromechanical procedure, as shown in Figure 3.2. In the first step of this procedure, a grid of nanocells is introduced. In this grid, a type and a location are assigned to each nanocell. In theory, the layout of the grid can be matched to experimental observations of synthesised MOF crystals to achieve a more accurate, more realistic system than current simulation methods allow, given their spatial limitations. The appearance and behaviour of defect clusters, for instance, can be mimicked by including nanocells of a defective type. The presence of an internal or external surface can be mimicked by including nanocells of a surface type.

If a nanocell deviates significantly from the ideal, defect-free unit cell of the MOF on the atomic level, then it should be assigned a different type. After all, the type of the nanocell is linked to a set of fixed elastic properties that need to be representative of its response to deformation. Not only does the equilibrium atomic structure of the nanocell matter in that context, its atomic structure in the grid, our newly defined environment, matters as well. The elastic properties of the nanocell must account for defects in its atomic structure and for severe distortions of its shape due to the presence of a surface or due to amorphisation.

Up to now, a grid of nanocells has been defined and a type has been assigned to each nanocell. As mentioned in the previous chapter, it is difficult to calculate the mechanical and elastic properties of such a large system. That is why, in the second step of the procedure, a mapping is performed from the old dynamical variables of the grid, the positions and momenta of atoms, to a new set of dynamical variables, the positions and momenta of massive, coarse-grained nodes. These micromechanical nodes are located on the vertices of each nanocell in the grid. For all intents and purposes, they *are* the vertices of the nanocells. They represent a mapping of as many atoms as possible onto as few beads as possible, a maximally coarse-grained system. Perhaps most importantly, each nanocell in the grid acts like an elastic coupling between the nodes on its own vertices. As such, the micromechanical nodes can interact with each other, along the connections of a network that spans the entire grid.

When a node deviates from its mechanical equilibrium position in the network, it causes an elastic deformation of the grid by distorting the shape of its surrounding nanocells. The elastic properties of the nanocells determine the response of the grid to the elastic deformation, affecting how far the deviation of one node travels through the network and how strongly the nanocells attempt to restore the node to its equilibrium position. An environment of rigid nanocells does not allow the node to deviate far from its equilibrium position, but an environment of flexible nanocells is more susceptible.

Despite not representing any specific atomic structure, the micromechanical nodes are formally treated as classical particles, governed by their equations of motion (Section 3.5). They are able to track local or long-range, potentially correlated, elastic deformations in a MOF. The mass of a node is calculated by summing up one eighth of the mass of each adjacent nanocell, which is assumed to be homogeneous and distributed among its nodes. The positions and momenta of the nodes are conjugate pairs of dynamical variables. These are needed to fully describe the state of the micromechanical system.

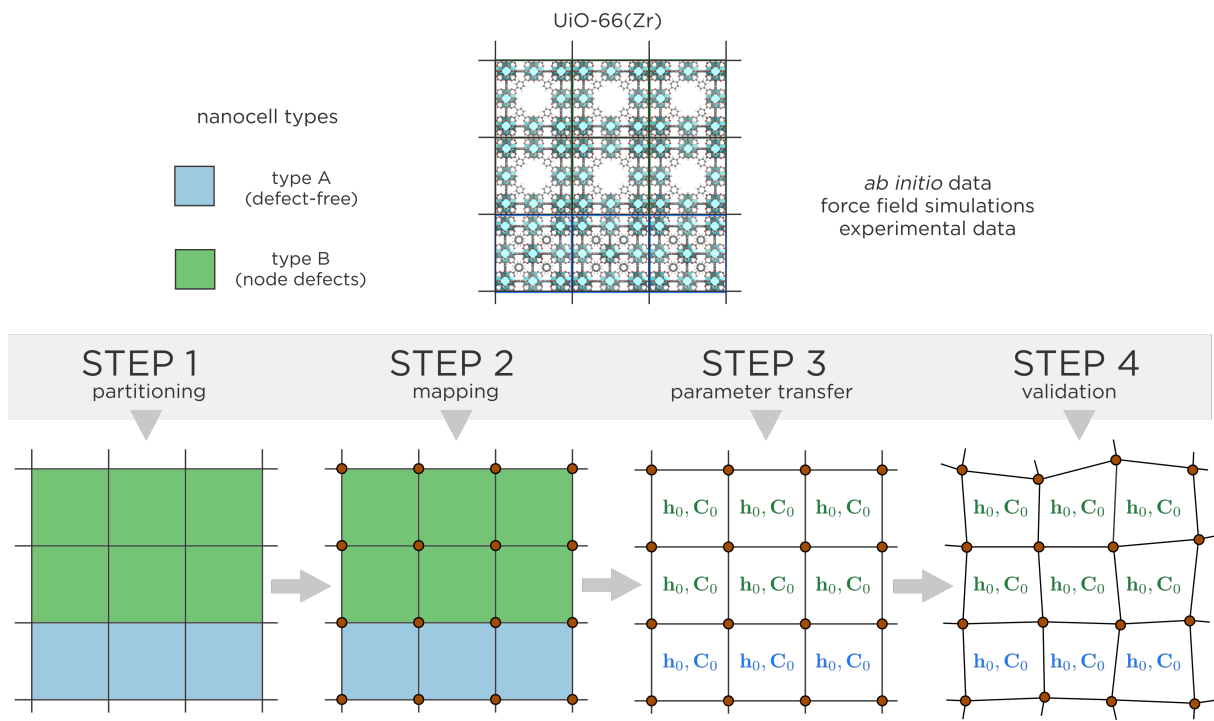


Figure 3.2: Schematic overview of the four steps in constructing, simulating and validating a micromechanical system. The example shown is a two-dimensional 3×3 domain of UiO-66 , containing three perfect nanocells and six defective nanocells. In the first step, the domain is represented as a grid containing different types of nanocells based on its atomic structure. In the second step, massive, coarse-grained nodes are introduced on the vertices of the grid, thereby replacing the previous all-atom description of the domain. In the third step, each type of nanocell is assigned a unique set of elastic properties, namely an equilibrium cell matrix \mathbf{h}_0 and an elasticity tensor \mathbf{C}_0 . These are derived from a higher level of theory (force field simulations or *ab initio* calculations). In the fourth step, a micromechanical MD simulation is performed. The motion of the coarse-grained nodes is sampled from a coarse-grained force field, which is fully determined by the elastic properties of the nanocells. For a small system such as this domain, it is possible to validate the results of the MD simulation by comparing them to the results of an atomistic force field simulation or *ab initio* data.

The third step of the micromechanical procedure is the transfer of parameters between levels of theory. Simulations on a higher level of theory than the micromechanical model, either *ab initio* calculations or atomistic force field simulations, are performed to obtain the elastic properties of each nanocell type. The elastic deformation energy of a nanocell is estimated by means of a harmonic approximation in the strain tensor. The harmonic approximation is a second-order approximation in the strain tensor, fully parametrised by the equilibrium cell matrix and the elasticity tensor of the nanocell type (\mathbf{h}_0 and \mathbf{C}_0). As parameters, these elastic properties fulfil the same roles as the rest length and the elastic constant of a classical spring, respectively, yet representing a three-dimensional material. The parameters \mathbf{h}_0 and

C_0 of a nanocell type are fixed during a micromechanical simulation and determine the strength of the coupling between nodes, featuring prominently in the equations of motion.

In the fourth and final step of the micromechanical procedure, a micromechanical simulation is performed. Despite not pertaining to molecules or atoms, a micromechanical simulation is identical to an atomistic MD simulation. The positions and momenta of the micromechanical nodes are updated at discrete, equidistant points in time with the velocity Verlet algorithm [25]. More details concerning the equations of motion are provided in Section 3.5. Lastly, it is worth noting that a micromechanical simulation can be performed in different ensembles, including the isochoric-isothermal (N, V, T) and the isobaric-isothermal (N, P, T) ensemble, just like any other MD simulation.

3.2 Advantages

A micromechanical system requires at least the following input: (i) the types of nanocells in the MOF, (ii) their locations in the grid and (iii) their elastic properties. The atomic structure of the MOF and all of the atomic interactions within the MOF are compressed into the elastic properties of its nanocell types. Moreover, the elastic properties, namely the elasticity tensor and the equilibrium cell matrix, only need to be calculated once for each type. This efficient compression of molecular information lies at the heart of the micromechanical model. Additionally, the hundreds or even thousands of atoms per nanocell are completely discarded in favour of only one node per nanocell in a micromechanical system with periodic boundary conditions. This reduction in the number of variables per unit length is the main advantage of the micromechanical model, even in comparison with other coarse-grained force fields. On top of that advantage, the elastic deformation energy of the nanocells and the equations of motion of the nodes can be expressed analytically.

Our ultimate goal is to simulate metal-organic frameworks on a larger length scale and on a longer time scale than force field simulations currently allow. Potentially thousands of nanocells can be included in one grid, reaching a length scale of tens or hundreds of nanometers. This unlocks many potential applications of the micromechanical model, some of which are displayed in Figure 3.3. Provided there is enough computing power, time scales of tens or hundreds of nanoseconds, even up to a microsecond, are attainable.

Atomistic force field simulations of most MOFs are limited to a maximum timestep of 0.5 fs or 1.0 fs, restricted by the need to accurately sample the fast vibrations of light atoms. The fastest vibrations of the micromechanical nodes, however, are decidedly slower than the fastest vibrations of atoms in a force field simulation. The dynamics of the system as a whole are smoothed because of our coarse-grained approach, which has been shown schematically in Figure 2.1. As such, the maximal timestep of a simulation can be increased to tens or even hundreds of femtoseconds.

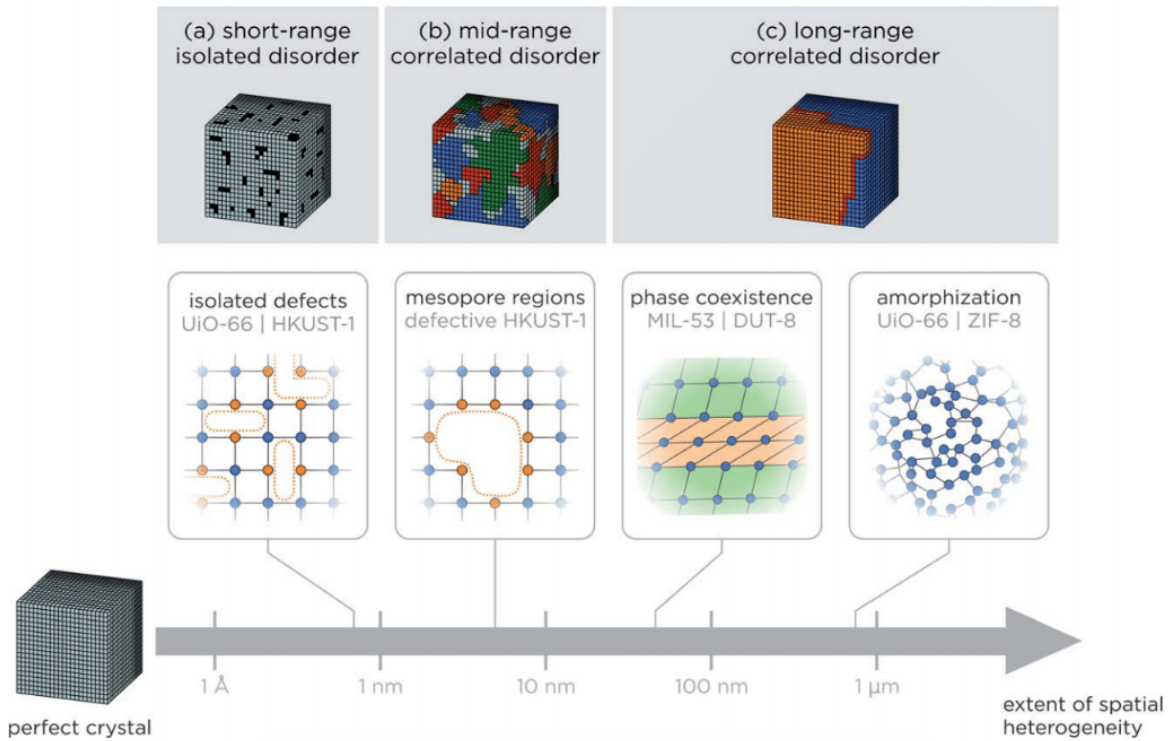


Figure 3.3: Classification of the different types of spatial disorder observed in MOFs, varying from (a) short-range isolated disorder ($< 1 \text{ nm}$), over (b) mid-range correlated disorder ($1\text{--}20 \text{ nm}$), to (c) long-range correlated disorder ($> 20 \text{ nm}$) with selected examples for each of the different types. These are potential applications of the micromechanical model. Figure reproduced from Ref. 29.

With respect to other coarse-grained force fields, the micromechanical model pushes its coarse graining to the limit. The nodes we introduce do not depend on the structural details of the MOF. As such, the micromechanical model stands in contrast to methods such as MARTINI coarse graining, where atoms are grouped into beads and these beads are used to mimic the original atomic structure of the MOF. Instead, the structural and topological information of each nanocell type is stored in its elastic properties. The elastic properties of the nanocell types are the parameters of the coarse-grained force field. Most importantly, the elasticity tensor predicts the response of a nanocell to elastic deformation and preserves the symmetry of the nanocell.

Each nanocell which cannot be represented as an elastic deformation of an existing type, should be defined as a new type. If the elastic properties of a certain type are found to deviate from their expected values, then that variance can be reflected in the system by adding more types with slightly different elastic properties. Similarly, if a type is dependent on its orientation with respect to the other types, then each orientation should be added as a new type. Thus, the spatial resolution of a micromechanical system can be controlled, to some extent, by deciding how many different types of nanocells are

included.

Lastly, the micromechanical model is not limited to periodic boundary conditions. Voids, surfaces, defects and interfaces can all be a part of a micromechanical system. If there exists experimental proof that two types of nanocells can coexist in a MOF, perhaps even next to each other, then those two types can be used in a micromechanical system. The model is therefore adaptable to many situations and highly transferable, requiring no complex fitting procedures or variational optimisation.

3.3 Parameters

Like any coarse-grained force field, the micromechanical model requires parameters. The parameters of the model, namely the elastic properties of its nanocells, have to be either fitted to experimental observations (the top-down approach) or extracted from a higher level of theory (the bottom-up approach). The transfer of parameters between levels of theory is included as the third step in the micromechanical procedure (Figure 3.2), but in a practical implementation, it is the first step.

We have defined the type of a nanocell as being (i) determined by its atomic structure and (ii) uniquely represented by its equilibrium elastic properties. These equilibrium elastic properties should be calculated and stored before any other calculations. Specifically, to calculate the elasticity tensor of a nanocell starting from its atomic structure, several methods exist.

An atomistic force field can simulate the elastic deformation behaviour of the atomic structure. The atomistic force field then acts as a reference for the coarse-grained, micromechanical force field, on the scale of a single nanocell. For additional accuracy, *ab initio* calculations can also act as a reference. Formally, the model does not depend on the level of theory of its reference. The coarse-grained force field applied to HKUST-1 in Section 2.3 is similar to a micromechanical force field in that regard.

However, the micromechanical model is also scale invariant, unlike the example in Section 2.3. The micromechanical model does not take the characteristics or specifics of atomic interactions into account if these do not have an impact on the elastic properties of a nanocell. As a consequence, a ‘nanocell’ does not need to be defined on a nanometer scale, or even as an atomic structure. Therefore, a ‘nanocell’ can be a much larger atomic structure than the unit cell of a typical MOF.

To understand how to extract the elasticity tensor from calculations on a higher level of theory, we must properly explain the concept of elastic deformation. In the elastic regime, a deformed nanocell is represented as a parallelepiped, regardless of its atomic structure. The shape of the parallelepiped is captured in a 3×3 cell matrix. This cell matrix contains the \mathbf{a} , \mathbf{b} and \mathbf{c} cell vectors [29], which span the

nanocell.

$$\mathbf{h} = \begin{bmatrix} a_x & a_y & a_z \\ b_x & b_y & b_z \\ c_x & c_y & c_z \end{bmatrix} \quad (3.1)$$

Here, it is important to note that the \mathbf{a} , \mathbf{b} and \mathbf{c} vectors are stored as rows in the cell matrix, by convention. The volume of the nanocell is the determinant of the cell matrix.

$$V = \det \mathbf{h} \quad (3.2)$$

To quantify the deformation of the nanocell, the concept of strain is introduced. In a general linear anisotropic material, stress and strain are 3×3 tensors. In Voigt notation, they become 6×1 column vectors [29]. The Lagrangian strain tensor $\boldsymbol{\varepsilon}$ can be calculated with the cell matrix \mathbf{h} and the equilibrium cell matrix \mathbf{h}_0 .

$$\boldsymbol{\varepsilon} = \frac{1}{2} [\mathbf{h}_0^{-1} \mathbf{h} \mathbf{h}^T \mathbf{h}_0^{-T} - \mathbf{1}] \quad (3.3)$$

The Lagrangian strain tensor is a symmetric 3×3 tensor.

$$\boldsymbol{\varepsilon} = \begin{bmatrix} \varepsilon_{11} & \varepsilon_{12} & \varepsilon_{13} \\ \varepsilon_{12} & \varepsilon_{22} & \varepsilon_{23} \\ \varepsilon_{13} & \varepsilon_{23} & \varepsilon_{33} \end{bmatrix} \quad (3.4)$$

The potential energy of a deformed nanocell, with respect to its equilibrium atomic structure, can be approximated as a function of the Lagrangian strain tensor. This is the harmonic, or elastic, approximation. It is derived from a Taylor expansion of the nanocell's Helmholtz free energy around its unstressed, equilibrium atomic structure.

$$F(\boldsymbol{\varepsilon}) - F_0 = \frac{1}{2} V_0 \boldsymbol{\varepsilon} : \mathbf{C} : \boldsymbol{\varepsilon} \quad (3.5)$$

The colon represents a double contraction over the last two indices of the first tensor and the first two indices of the second tensor, an operation which is often called the double contraction or the double inner product. Using the Einstein summation convention, the double contraction is defined as follows.

$$[\mathbf{C} : \boldsymbol{\varepsilon}]_{ij} = C_{ijkl} \varepsilon_{kl} \quad (3.6)$$

In the elastic regime, Hooke's law states that the stress tensor $\boldsymbol{\sigma}$ is proportional to the strain tensor $\boldsymbol{\varepsilon}$.

$$\sigma_{ij} = C_{ijkl} \varepsilon_{kl} \quad (3.7)$$

$$\varepsilon_{ij} = S_{ijkl} \sigma_{kl} \quad (3.8)$$

The elasticity (or stiffness) tensor \mathbf{C} is the inverse of the compliance tensor \mathbf{S} . The unit tensor in this case has a particular form [39].

$$C_{ijmn} S_{mnkl} = S_{ijmn} C_{mnkl} = \frac{1}{2}(\delta_{ik}\delta_{jl} + \delta_{il}\delta_{jk}) \quad (3.9)$$

Both $3 \times 3 \times 3 \times 3$ tensors can be written as 6×6 matrices using Voigt notation [29]. As matrices, they can be inverted easily.

Throughout this thesis, we will often add a subscript zero to the elasticity tensor, to signify that it is a fixed equilibrium property: \mathbf{C}_0 . This is technically redundant, because the elasticity tensor is only defined at equilibrium, but it is consistent with the notation of \mathbf{h}_0 , the equilibrium cell matrix.

For a general anisotropic material, the elasticity and compliance tensors are $3 \times 3 \times 3 \times 3$ tensors with minor and major symmetries. The number of independent components in the elasticity tensor decreases as the internal symmetry of the atomic structure increases. For orthorhombic crystal systems, the elasticity tensor only contains nine independent components, as seen here in Voigt notation [13].

$$\mathbf{C}(\text{ortho}) = \begin{bmatrix} C_{11} & C_{12} & C_{13} & 0 & 0 & 0 \\ C_{12} & C_{22} & C_{23} & 0 & 0 & 0 \\ C_{13} & C_{23} & C_{33} & 0 & 0 & 0 \\ 0 & 0 & 0 & C_{44} & 0 & 0 \\ 0 & 0 & 0 & 0 & C_{55} & 0 \\ 0 & 0 & 0 & 0 & 0 & C_{66} \end{bmatrix} \quad (3.10)$$

For cubic crystal systems, only three independent elastic constants remain [13].

$$\mathbf{C}(\text{cubic}) = \begin{bmatrix} C_{11} & C_{12} & C_{12} & 0 & 0 & 0 \\ C_{12} & C_{11} & C_{12} & 0 & 0 & 0 \\ C_{12} & C_{12} & C_{11} & 0 & 0 & 0 \\ 0 & 0 & 0 & C_{44} & 0 & 0 \\ 0 & 0 & 0 & 0 & C_{44} & 0 \\ 0 & 0 & 0 & 0 & 0 & C_{44} \end{bmatrix} \quad (3.11)$$

It is then trivial to calculate the eigenvalues of this matrix.

$$\lambda_1 = C_{11} + 2C_{12} \quad (3.12)$$

$$\lambda_2 = C_{11} - C_{12} \quad (3.13)$$

$$\lambda_3 = C_{44} \quad (3.14)$$

The eigenvalue λ_2 is twofold degenerate and the eigenvalue λ_3 is threefold degenerate. The first, non-degenerate, eigenvalue corresponds to an isotropic compression of the cubic crystal, the second eigenvalue corresponds to tensile deformations and the third eigenvalue corresponds to shear deformations.

In general, the eigenvalues of the elasticity tensor must be strictly positive. In other words, the elasticity tensor must be positive definite to guarantee the stability of the atomic structure [13].

From the elasticity tensor and the compliance tensor, several properties of the material can be derived, such as the bulk modulus, the directional Young modulus and the directional shear modulus. These properties are a useful measure to compare, analyse and visualise the elastic behaviour of different nanocells. In the following formulas, the Einstein summation convention is assumed. The bulk modulus can be derived from the elasticity tensor.

$$K = \frac{1}{9} C_{iikk} \quad (3.15)$$

The directional Young modulus and the directional shear modulus are derived from the compliance tensor [17].

$$E(\mathbf{u}) = \frac{1}{u_i u_j u_k u_l S_{ijkl}} \quad (3.16)$$

$$G(\mathbf{u}, \mathbf{v}) = \frac{1}{u_i v_j u_k v_l S_{ijkl}} \quad (3.17)$$

The vectors \mathbf{u} and \mathbf{v} are unit vectors. The Young modulus characterises the uniaxial stiffness of the material in the \mathbf{u} direction. The shear modulus characterises the resistance to shearing of the plane normal to \mathbf{v} in the \mathbf{u} direction.

Equipped with this theory of elastic deformation, we can explain a variety of methods to calculate the elasticity tensor of a nanocell. In general, the elastic constants of a nanocell can be completely defined using six independent deformation modes of the atomic structure, corresponding to the six independent elements of the symmetric strain tensor. After a full optimisation, the energy or strain resulting from each deformation mode can be used to estimate the corresponding elastic constants, such that Eq. 3.5 is satisfied in the least-squares sense.

At 0 K, the free energy of the nanocell is approximately equal to its potential energy. The bulk modulus is therefore easy to calculate. By increasing or decreasing the volume of the nanocell by small increments, it is possible to construct an energy-versus-volume equation of state. For each volume increment, a full optimisation of the atomic structure and the shape of the nanocell is performed. Such a procedure is called a relaxed scan. The bulk modulus is closely related to the curvature of the energy-versus-volume equation of state near equilibrium.

$$K = V_0 \left. \frac{\partial^2 E}{\partial V^2} \right|_{V_0} \quad (3.18)$$

Importantly, we can make a distinction between static calculations of the elastic constants, like the one above, and dynamic calculations. Dynamic calculations rely on ensemble averages. As an example, the

following expression is used to calculate the $3 \times 3 \times 3 \times 3$ compliance tensor \mathbf{S} in the (N, P, T) ensemble.

$$S_{ijkl} = \frac{\langle V \rangle}{k_B T} \left\langle (\varepsilon_{ij} - \langle \varepsilon_{ij} \rangle)(\varepsilon_{kl} - \langle \varepsilon_{kl} \rangle) \right\rangle \quad (3.19)$$

Afterwards, the compliance tensor is converted to Voigt notation. The inverse of the compliance tensor, now in Voigt notation, is the elasticity tensor, in Voigt notation. This procedure will prove to be a crucial part of the validation strategy of the micromechanical model, as will be explained in Chapter 4 and Chapter 5.

The ensemble averages of Eq. 3.19 can be extracted from a well-converged MD simulation using an atomistic force field. The properties of the nanocell, averaged over a long period of time during the MD simulation, should converge to their ensemble averages. This assumption is known as the ergodic hypothesis [25].

3.4 Limitations

Although the micromechanical model has many advantages, it is limited by its reliance on simulations of a higher level of theory, like all bottom-up coarse graining methods. These simulations impose major restrictions on the kinds of nanocells that can be included in a grid. Firstly, these nanocells have to be periodically repeating and they have to converge to a (meta)stable state. Otherwise, the equilibrium cell matrix and elasticity tensor are ill-defined. Secondly, there are computational limits to both *ab initio* and atomistic force field simulations. A supercell containing a defect can be too large for *ab initio* MD simulations, especially if the system has to equilibrate and reach a reasonable time scale. Atomistic force field MD simulations, for example in the (N, P, T) ensemble, are more broadly applicable, but the force fields themselves are fitted to *ab initio* calculations and prone to fitting errors. Thirdly, the elastic properties of a nanocell depend on thermodynamic conditions such as pressure, temperature and guest adsorption. The coarse-grained force field is derived from the elastic properties and is therefore, essentially, a free energy. Strictly speaking, the elastic properties should be recalculated for each configuration in the thermodynamic state space.

Therefore, the micromechanical model is not necessarily as transferable in practice as it is in concept. The method in itself is very simple and transferable, because nearly all MOFs can be divided into nanocells and simulated in order to calculate their elastic properties. The results of these simulations are also recyclable: a nanocell type that has been characterised and used in one simulation, can be reused in any other system, with only a minimal amount of data storage. The mapping procedure of the micromechanical model doesn't require a complex scheme, but therein lies an unavoidable flaw as well. The reason why classical, atomistic force fields are sometimes transferable, is because they define generic atom types and derive parameters that are generally applicable to many systems. In the micromechanical model, there is currently no way to predict the elastic properties of a nanocell, based

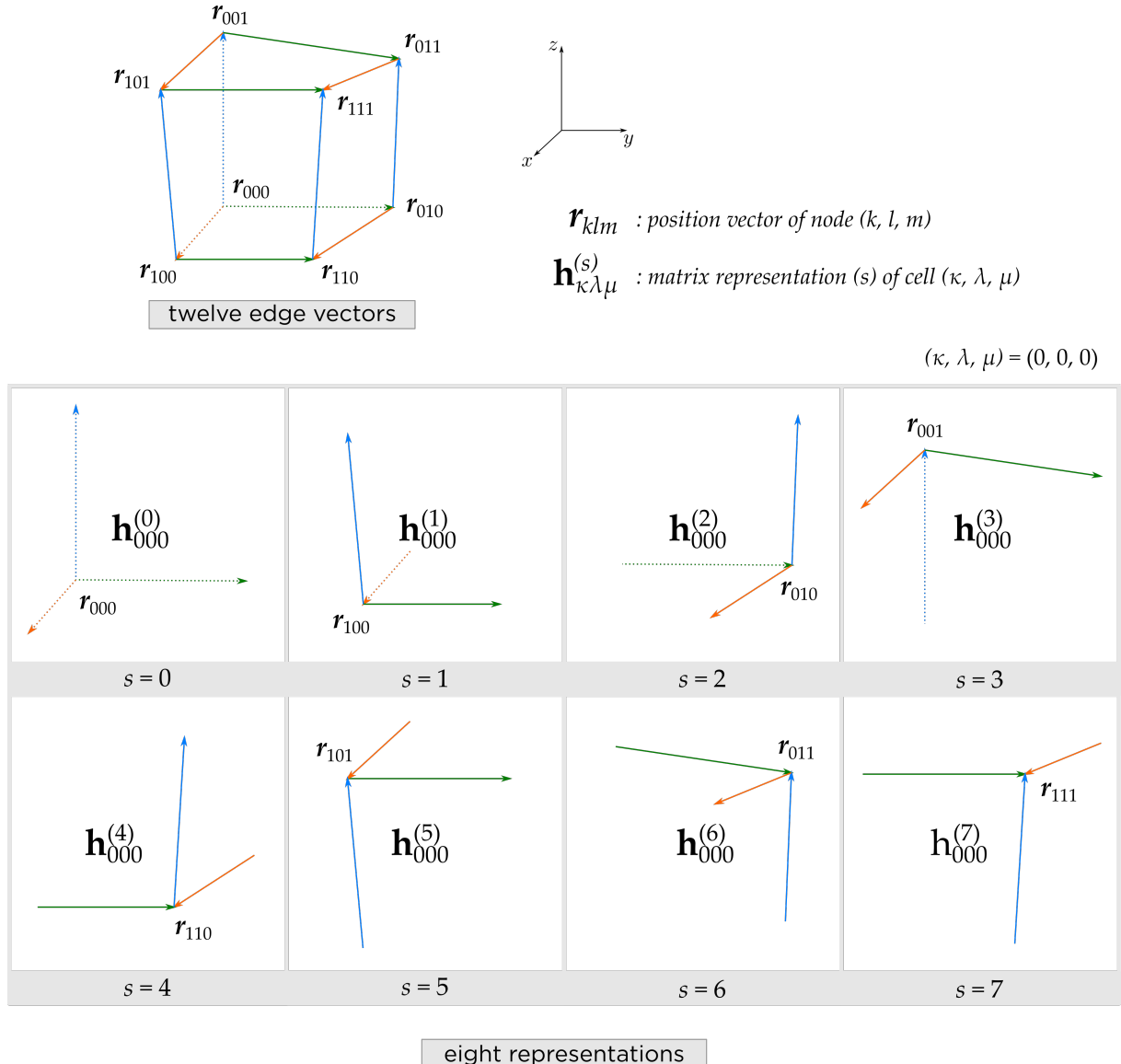


Figure 3.4: Representations of an arbitrarily shaped nanocell in the micromechanical model. Each vertex of the nanocell is a micromechanical node. To describe the nanocell at any point in time, its twelve edge vectors are used to construct eight distinct cell matrices.

on its atomic structure, without experimental data, atomistic force field simulations, or *ab initio* calculations. Only the symmetry of the elasticity tensor is known upfront. In other words, the parameters of the model are always an unknown *a priori* and we cannot propose any generally applicable parameters. For each new system, the elastic properties have to be calculated explicitly. In time, perhaps a database of elastic properties could provide general predictions, but, for now, there is no such option.

Aside from these limitations, three main issues can affect the accuracy and effectiveness of the micromechanical model. All three issues stem from the coarse-grained nature of the model and in all three cases,

we assume they can be circumvented or safely ignored.

The first issue is the fact that an elasticity tensor can only describe the deformation of a parallelepiped nanocell into another parallelepiped nanocell. The three vectors which span the nanocell are stored in a cell matrix. With three independent vectors, the most general shape a cell matrix can describe is indeed a parallelepiped. When the micromechanical nodes are moving around, they do not necessarily span a parallelepiped. Instead, they can span an arbitrary shape at any point in time.

In the original version of the micromechanical model, a compromise was made to solve this issue [29]. The twelve edge vectors of the arbitrarily shaped nanocell were reduced to three cell vectors by applying the vectorial mean. The averaged cell vectors could then span a parallelepiped whose shape resembled the shape of the distorted nanocell as closely as possible. However, this approach was hindered by one potentially fatal flaw: the vectorial mean of the edge vectors does not represent a one-to-one mapping between the micromechanical nodes and the cell matrix. As such, there are infinitely many, impossible, *i.e.*, absurd configurations of nodes surrounding a nanocell that nonetheless do correspond to a possible, *i.e.*, reasonable cell matrix. This presented an immediate issue for any system with non-periodic boundary conditions. An MD simulation of a system with non-periodic boundary conditions, in the (N, V, E) ensemble, revealed that the nodes of the system could diverge, unrestricted, from their initial positions to impossible positions. While the nodes were diverging, however, the potential energy of the system could remain bounded and the simulation could continue as if nothing out of the ordinary was happening. To avoid this exact situation, a new version of the micromechanical model, a version that takes both periodic and non-periodic boundary conditions into account, was proposed by us.

In this new version of the micromechanical model, the arbitrary shape of the nanocell is split into eight distinct *representations*, as shown in Figure 3.4. Though there is no longer a unified representation for the entire cell, each corner of the cell is now accurately represented. Furthermore, this strategy does provide a one-to-one mapping between the eight nodes of the cell and the eight representations of the cell matrix. Writing down each representation for the example of Figure 3.4 results in Eq. 3.20.

$$\begin{aligned} \mathbf{h}_{000}^{(0)} &= \left[\begin{array}{c|c|c} \mathbf{r}_{100} - \mathbf{r}_{000} & \mathbf{r}_{010} - \mathbf{r}_{000} & \mathbf{r}_{001} - \mathbf{r}_{000} \end{array} \right] \\ \mathbf{h}_{000}^{(1)} &= \left[\begin{array}{c|c|c} \mathbf{r}_{100} - \mathbf{r}_{000} & \mathbf{r}_{110} - \mathbf{r}_{100} & \mathbf{r}_{101} - \mathbf{r}_{100} \end{array} \right] \\ \mathbf{h}_{000}^{(2)} &= \left[\begin{array}{c|c|c} \mathbf{r}_{110} - \mathbf{r}_{010} & \mathbf{r}_{010} - \mathbf{r}_{000} & \mathbf{r}_{011} - \mathbf{r}_{010} \end{array} \right] \\ \mathbf{h}_{000}^{(3)} &= \left[\begin{array}{c|c|c} \mathbf{r}_{101} - \mathbf{r}_{001} & \mathbf{r}_{011} - \mathbf{r}_{001} & \mathbf{r}_{001} - \mathbf{r}_{000} \end{array} \right] \\ \mathbf{h}_{000}^{(4)} &= \left[\begin{array}{c|c|c} \mathbf{r}_{110} - \mathbf{r}_{010} & \mathbf{r}_{110} - \mathbf{r}_{100} & \mathbf{r}_{111} - \mathbf{r}_{110} \end{array} \right] \\ \mathbf{h}_{000}^{(5)} &= \left[\begin{array}{c|c|c} \mathbf{r}_{101} - \mathbf{r}_{001} & \mathbf{r}_{111} - \mathbf{r}_{101} & \mathbf{r}_{101} - \mathbf{r}_{100} \end{array} \right] \\ \mathbf{h}_{000}^{(6)} &= \left[\begin{array}{c|c|c} \mathbf{r}_{111} - \mathbf{r}_{011} & \mathbf{r}_{011} - \mathbf{r}_{001} & \mathbf{r}_{011} - \mathbf{r}_{010} \end{array} \right] \\ \mathbf{h}_{000}^{(7)} &= \left[\begin{array}{c|c|c} \mathbf{r}_{111} - \mathbf{r}_{011} & \mathbf{r}_{111} - \mathbf{r}_{101} & \mathbf{r}_{111} - \mathbf{r}_{110} \end{array} \right] \end{aligned} \tag{3.20}$$

The nanocell of Eq. 3.20 and Figure 3.4 is identified with the integer values $(\kappa, \lambda, \mu) = (0, 0, 0)$, indicating

its location in the grid of nanocells. The eight representations of the nanocell at (κ, λ, μ) are identified with a superscript (s) . Thus, an arbitrary nanocell representation in the grid of nanocells is written as

$$\mathbf{h}_{\kappa\lambda\mu}^{(s)} \quad \text{with } s \in \{0, 1, 2, 3, 4, 5, 6, 7\}. \quad (3.21)$$

The reader should understand that the introduction of these nanocell representations leads to separate representations of the strain tensor of the nanocell, defined as follows.

$$\boldsymbol{\varepsilon}_{\kappa\lambda\mu}^{(s)} = \frac{1}{2} \left[\mathbf{h}_{\kappa\lambda\mu,0}^{-T} \left(\mathbf{h}_{\kappa\lambda\mu}^{(s)} \right)^T \left(\mathbf{h}_{\kappa\lambda\mu}^{(s)} \right) \mathbf{h}_{\kappa\lambda\mu,0}^{-1} - \mathbf{1} \right] \quad (3.22)$$

Here, it must also be noted that the cell vectors of each representation in Eq. 3.20 are stored in their cell matrix as columns, contrary to convention. This is why Eq. 3.22 differs from Eq. 3.3.

The second issue is unavoidable for any coarse-grained approach. Any high-frequency motion on the atomic level is discarded by only considering deformations of the entire nanocell on the micromechanical level. Small structures in a nanocell are invisible on the coarse-grained level if they do not have an impact on the end result of the calculation to determine the elastic properties. Although these small structures do not contribute to the elasticity tensor or to the equilibrium cell matrix of the nanocell, their high-frequency motion can, in theory, still have a measurable effect on the properties of the material. The issue is typical for any coarse-grained system, as its free energy landscape is smoothed and most of the fast dynamics disappear.

In theory, the third issue is avoidable. It is assumed that the elasticity tensor of a nanocell does not change when its shape is severely distorted. The elasticity tensor defines the harmonic approximation of the elastic potential energy around the equilibrium cell matrix. Assuming the elasticity tensor is constant, is analogous to assuming that the classical force constant of a spring does not change whenever the spring is stretched or compressed and analogous to assuming that the elastic potential energy does not deviate from perfect harmonicity. The micromechanical model can be extended with anharmonicity, at least in theory, but that lies beyond the scope of this work. Currently, the only deviation from harmonicity is found in the equations of motion for bistable nanocells.

3.5 Equations of motion for unstable nanocells

The following conventions should be clarified. Micromechanical nodes are indexed with Roman letters (k, l, m) . Nanocells are indexed with Greek letters (κ, λ, μ) . These indices refer to the location of a node or a nanocell in a three-dimensional grid. Each nanocell in the three-dimensional grid has eight surrounding nodes, but not all nodes have eight surrounding nanocells, as some nodes can be located at an internal or external surface. The subscript zero indicates that a property of a nanocell is an equilibrium property, determined from a higher level of theory and constant throughout any micromechanical simulation. Here, the term *equilibrium* is used to indicate the most stable, energetically most favourable,

state of the nanocell if it could be surrounded by periodic images of itself. Finally, the superscript (s) denotes one of eight representations of a nanocell, as defined in Eq. 3.20 and Eq. 3.21.

When a nanocell has been deformed, its eight representations, $\mathbf{h}_{\kappa\lambda\mu}^{(s)}$, differ from its equilibrium cell matrix, $\mathbf{h}_{\kappa\lambda\mu,0}$. The deformed nanocell wishes to relax to its equilibrium state, much like a stretched classical spring wishes to relax to its rest length. The 3×3 finite Lagrangian strain tensor is a dimensionless measure of the nanocell's deviation from its equilibrium cell matrix. Like the cell matrix, the strain tensor is also not uniquely defined. Each nanocell has eight representations of its strain tensor, which are defined as

$$\boldsymbol{\epsilon}_{\kappa\lambda\mu}^{(s)} = \frac{1}{2} \left[\mathbf{h}_{\kappa\lambda\mu,0}^{-T} \left(\mathbf{h}_{\kappa\lambda\mu}^{(s)} \right)^T \left(\mathbf{h}_{\kappa\lambda\mu}^{(s)} \right) \mathbf{h}_{\kappa\lambda\mu,0}^{-1} - \mathbf{1} \right]. \quad (3.23)$$

We define the set $S_{\kappa\lambda\mu}$ as the set of eight micromechanical nodes surrounding nanocell (κ, λ, μ) , *i.e.*, the vertices of nanocell (κ, λ, μ) . As shown in Eq. 3.20, an arbitrary nanocell representation $\mathbf{h}_{\kappa\lambda\mu}^{(s)}$ depends on the dynamical variables $\{\mathbf{r}_{klm}\}_{S_{\kappa\lambda\mu}}$. Therefore, the nanocell representations and the strain tensor representations are implicitly time-dependent. For the sake of compact notation, we will not state this time-dependence explicitly or otherwise in the following derivations. Instead, we write it here as a reminder.

$$\begin{aligned} \mathbf{h}_{\kappa\lambda\mu}^{(s)} &\equiv \mathbf{h}_{\kappa\lambda\mu}^{(s)}(\{\mathbf{r}_{klm}(t)\}_{S_{\kappa\lambda\mu}}) \\ \boldsymbol{\epsilon}_{\kappa\lambda\mu}^{(s)} &\equiv \boldsymbol{\epsilon}_{\kappa\lambda\mu}^{(s)}(\{\mathbf{r}_{klm}(t)\}_{S_{\kappa\lambda\mu}}) \end{aligned} \quad (3.24)$$

The elastic energy of a nanocell representation is expressed as a harmonic approximation, as a function of its 3×3 strain tensor representation, its $3 \times 3 \times 3 \times 3$ elasticity tensor and the corresponding representation of its volume. Implicitly, it is also a function of the coordinates of the surrounding nodes.

$$U_{\kappa\lambda\mu}^{(s)} = \frac{1}{2} \det(\mathbf{h}_{\kappa\lambda\mu}^{(s)}) \left(\boldsymbol{\epsilon}_{\kappa\lambda\mu}^{(s)} \right)^T : \mathbf{C}_{\kappa\lambda\mu,0} : \left(\boldsymbol{\epsilon}_{\kappa\lambda\mu}^{(s)} \right) \quad (3.25)$$

The potential energy of a nanocell is the mean of the potential energies of its eight representations.

$$U_{\kappa\lambda\mu} = \frac{1}{8} \sum_{s=0}^7 U_{\kappa\lambda\mu}^{(s)} \quad (3.26)$$

Each nanocell contributes to the total potential energy of the system.

$$U_{sys} = \sum_{\kappa,\lambda,\mu} U_{\kappa\lambda\mu} = \sum_{\kappa,\lambda,\mu} \left(\frac{1}{8} \sum_{s=0}^7 U_{\kappa\lambda\mu}^{(s)} \right) \quad (3.27)$$

Now, the force acting on node (k, l, m) is simply the negative gradient of the total potential energy of the system with respect to the dynamical variable \mathbf{r}_{klm} . However, only the nanocells surrounding node (k, l, m) depend on \mathbf{r}_{klm} , which means that the force acting on node (k, l, m) can be expressed as a sum of contributions from, at most, eight surrounding nanocells. The set of nanocells surrounding node

(k, l, m) is written as S_{klm} . Additionally, it is worth mentioning that only four of eight representations of any surrounding nanocell contribute to the force acting on the node.

$$\begin{aligned} f_{klm} &= -\nabla_{r_{klm}} U_{sys} = \sum_{\substack{\kappa, \lambda, \mu \\ \in S_{klm}}} -\nabla_{r_{klm}} U_{\kappa\lambda\mu} = \sum_{\substack{\kappa, \lambda, \mu \\ \in S_{klm}}} \left(\frac{1}{8} \sum_{s=0}^7 -\nabla_{r_{klm}} U_{\kappa\lambda\mu}^{(s)} \right) \\ &= \sum_{\substack{\kappa, \lambda, \mu \\ \in S_{klm}}} f_{klm}|_{\kappa\lambda\mu} = \sum_{\substack{\kappa, \lambda, \mu \\ \in S_{klm}}} \left(\frac{1}{8} \sum_{s=0}^7 f_{klm}|_{\kappa\lambda\mu}^{(s)} \right) \end{aligned} \quad (3.28)$$

The contribution to the force acting on node (k, l, m) due to representation (s) of nanocell (κ, λ, μ) can be expanded by plugging in Eq. 3.25, applying the gradient and using the product rule.

$$\begin{aligned} f_{klm}|_{\kappa\lambda\mu}^{(s)} &= -\frac{1}{2} \left(\nabla_{r_{klm}} \det(\mathbf{h}_{\kappa\lambda\mu}^{(s)}) \right) (\boldsymbol{\epsilon}_{\kappa\lambda\mu}^{(s)})^T : \mathbf{C}_{\kappa\lambda\mu, 0} : (\boldsymbol{\epsilon}_{\kappa\lambda\mu}^{(s)}) \\ &\quad - \frac{1}{2} \det(\mathbf{h}_{\kappa\lambda\mu}^{(s)}) \left(\nabla_{r_{klm}} \boldsymbol{\epsilon}_{\kappa\lambda\mu}^{(s)} \right)^T : \mathbf{C}_{\kappa\lambda\mu, 0} : (\boldsymbol{\epsilon}_{\kappa\lambda\mu}^{(s)}) \\ &\quad - \frac{1}{2} \det(\mathbf{h}_{\kappa\lambda\mu}^{(s)}) (\boldsymbol{\epsilon}_{\kappa\lambda\mu}^{(s)})^T : \mathbf{C}_{\kappa\lambda\mu, 0} : \left(\nabla_{r_{klm}} \boldsymbol{\epsilon}_{\kappa\lambda\mu}^{(s)} \right) \end{aligned} \quad (3.29)$$

A representation of the volume of nanocell (κ, λ, μ) , which is the determinant of a nanocell representation, can be split off as a prefactor after calculating the gradient of the determinant. Three terms remain. The coefficient of the first term contains the trace of the inverse cell matrix multiplied with the gradient of the cell matrix.

$$\begin{aligned} f_{klm}|_{\kappa\lambda\mu}^{(s)} &= -\frac{1}{2} \det(\mathbf{h}_{\kappa\lambda\mu}^{(s)}) \left[\text{trace} \left(\left(\mathbf{h}_{\kappa\lambda\mu}^{(s)} \right)^{-1} \nabla_{r_{klm}} \mathbf{h}_{\kappa\lambda\mu}^{(s)} \right) (\boldsymbol{\epsilon}_{\kappa\lambda\mu}^{(s)})^T : \mathbf{C}_{\kappa\lambda\mu, 0} : (\boldsymbol{\epsilon}_{\kappa\lambda\mu}^{(s)}) \right. \\ &\quad + \left(\nabla_{r_{klm}} \boldsymbol{\epsilon}_{\kappa\lambda\mu}^{(s)} \right)^T : \mathbf{C}_{\kappa\lambda\mu, 0} : (\boldsymbol{\epsilon}_{\kappa\lambda\mu}^{(s)}) \\ &\quad \left. + (\boldsymbol{\epsilon}_{\kappa\lambda\mu}^{(s)})^T : \mathbf{C}_{\kappa\lambda\mu, 0} : \left(\nabla_{r_{klm}} \boldsymbol{\epsilon}_{\kappa\lambda\mu}^{(s)} \right) \right] \end{aligned} \quad (3.30)$$

The gradient of each strain tensor representation can be rewritten as a function of its corresponding nanocell representation by applying the gradient operator to Eq. 3.22.

$$\nabla_{r_{klm}} (\boldsymbol{\epsilon}_{\kappa\lambda\mu}^{(s)})^T = \nabla_{r_{klm}} \boldsymbol{\epsilon}_{\kappa\lambda\mu}^{(s)} = \frac{1}{2} \mathbf{h}_{\kappa\lambda\mu, 0}^{-T} \left[\nabla_{r_{klm}} \left(\mathbf{h}_{\kappa\lambda\mu}^{(s)} \right)^T \mathbf{h}_{\kappa\lambda\mu}^{(s)} + \left(\mathbf{h}_{\kappa\lambda\mu}^{(s)} \right)^T \nabla_{r_{klm}} \mathbf{h}_{\kappa\lambda\mu}^{(s)} \right] \mathbf{h}_{\kappa\lambda\mu, 0}^{-1} \quad (3.31)$$

We define the gradient of a cell matrix as follows.

$$\nabla_{r_{klm}} \mathbf{h}_{\kappa\lambda\mu}^{(s)} = \mathbf{u}_x \frac{\partial}{\partial x_{klm}} \mathbf{h}_{\kappa\lambda\mu}^{(s)} + \mathbf{u}_y \frac{\partial}{\partial y_{klm}} \mathbf{h}_{\kappa\lambda\mu}^{(s)} + \mathbf{u}_z \frac{\partial}{\partial z_{klm}} \mathbf{h}_{\kappa\lambda\mu}^{(s)} \quad (3.32)$$

The partial derivative operators act element-wise on the cell matrix and the vectors \mathbf{u}_x , \mathbf{u}_y , \mathbf{u}_z are Cartesian unit vectors. The partial derivatives can be calculated easily starting from Eq. 3.20.

Finally, Newton's second law or Hamilton's equations can be used to obtain an equation of motion for each node.

Newtonian formalism:

$$\begin{aligned}\dot{\mathbf{p}}_{klm} &= \mathbf{f}_{klm} \\ \dot{\mathbf{r}}_{klm} &= \frac{\mathbf{p}_{klm}}{m_{klm}}\end{aligned}$$

Hamiltonian formalism:

$$\begin{aligned}H_{sys} &= \sum_{k,l,m} \frac{\mathbf{p}_{klm}^2}{2m_{klm}} + U_{sys} \\ \dot{\mathbf{p}}_{klm} &= -\nabla_{\mathbf{r}_{klm}} H_{sys} \\ \dot{\mathbf{r}}_{klm} &= \nabla_{\mathbf{p}_{klm}} H_{sys}\end{aligned}\tag{3.33}$$

The Newtonian and Hamiltonian formalisms lead to the same equations of motion.

$$\begin{aligned}\dot{\mathbf{p}}_{klm} &= \mathbf{f}_{klm} = \sum_{\substack{\kappa,\lambda,\mu \\ \in S_{klm}}} f_{klm}|_{\kappa\lambda\mu} = (\text{Eq. 3.28}) \\ \dot{\mathbf{r}}_{klm} &= \frac{\mathbf{p}_{klm}}{m_{klm}} = \mathbf{v}_{klm}\end{aligned}\tag{3.34}$$

The mass of node (k, l, m) is calculated by summing one eighth of the mass of each surrounding nanocell.

$$m_{klm} = \frac{1}{8} \sum_{\substack{\kappa,\lambda,\mu \\ \in S_{klm}}} m_{\kappa\lambda\mu}\tag{3.35}$$

3.6 Equations of motion for bistable nanocells

As in the unistable case, each bistable nanocell (κ, λ, μ) contributes to the total potential energy of the system.

$$U_{sys} = \sum_{\kappa,\lambda,\mu} U_{\kappa\lambda\mu}\tag{3.36}$$

The biggest difference between the unistable case and the bistable case lies in the description of the potential energy of the nanocell. Depending on the deformation of the nanocell, its configuration is more similar to one or the other metastable state. In other words, its elastic potential energy is not simply a harmonic approximation of a single state. Instead, it is a thermodynamic interpolation between the harmonic approximations of both states [29, 40].

$$U_{\kappa\lambda\mu} = -k_B T_{\kappa\lambda\mu}^* \ln \left[\exp \left(-\frac{U_{\kappa\lambda\mu}^{(I)}}{k_B T_{\kappa\lambda\mu}^*} \right) + \exp \left(-\frac{U_{\kappa\lambda\mu}^{(II)} + \Delta F_{\kappa\lambda\mu}^{(I) \rightarrow (II)}}{k_B T_{\kappa\lambda\mu}^*} \right) \right]\tag{3.37}$$

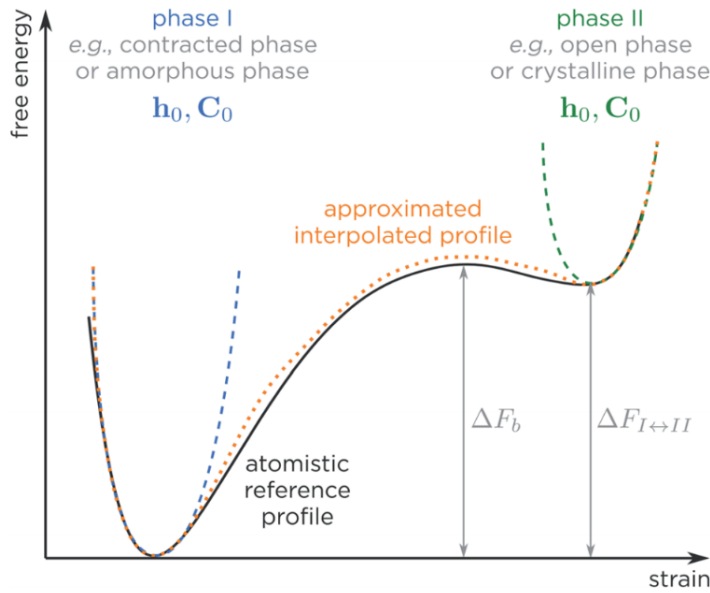


Figure 3.5: Visual representation of the thermodynamic interpolation of Eq. 3.37, used to approximate the free energy surface of an atomistic, bistable nanocell. Each metastable state has its own type and hence, its own harmonic approximation as a function of strain. Figure reproduced from Ref. 29.

Figure 3.5 provides a visual clarification of this approach. Essentially, Eq. 3.37 is an approximation of the free energy surface of the atomistic nanocell, as an implicit function of the micromechanical nodes. As explained in Section 2.2, this free energy surface of the atomistic nanocell becomes the force field of the coarse-grained nanocell. Aside from the two types present in this formula and their associated elastic properties, two new parameters appear: the atomistic free energy difference between metastable states, $\Delta F_{\kappa\lambda\mu}^{(I)\rightarrow(II)}$, and a tunable temperature, $T_{\kappa\lambda\mu}^*$, which is used to accurately reproduce the free energy barrier between the metastable states.

As before, the potential energy contribution of each metastable state is the mean of the potential energies of its eight representations.

$$\begin{aligned} U_{\kappa\lambda\mu}^{(I)} &= \frac{1}{8} \sum_{s=0}^7 U_{\kappa\lambda\mu}^{(I)(s)} \\ U_{\kappa\lambda\mu}^{(II)} &= \frac{1}{8} \sum_{s=0}^7 U_{\kappa\lambda\mu}^{(II)(s)} \end{aligned} \quad (3.38)$$

Each representation is, once again, a harmonic approximation. Both the strain tensor and the elasticity

tensor are different for both metastable states.

$$\begin{aligned} U_{\kappa\lambda\mu}^{(I)(s)} &= \frac{1}{2} \det(\mathbf{h}_{\kappa\lambda\mu}^{(s)}) \left(\boldsymbol{\epsilon}_{\kappa\lambda\mu}^{(I)(s)} \right)^T : \mathbf{C}_{\kappa\lambda\mu,0}^{(I)} : \left(\boldsymbol{\epsilon}_{\kappa\lambda\mu}^{(I)(s)} \right) \\ U_{\kappa\lambda\mu}^{(II)(s)} &= \frac{1}{2} \det(\mathbf{h}_{\kappa\lambda\mu}^{(s)}) \left(\boldsymbol{\epsilon}_{\kappa\lambda\mu}^{(II)(s)} \right)^T : \mathbf{C}_{\kappa\lambda\mu,0}^{(II)} : \left(\boldsymbol{\epsilon}_{\kappa\lambda\mu}^{(II)(s)} \right) \end{aligned} \quad (3.39)$$

To proceed, one simply has to calculate the gradient of the total potential energy. The force acting on a micromechanical node then consists of the contributions of each representation of each metastable state of each surrounding nanocell.

$$\begin{aligned} f_{klm} = -\nabla_{r_{klm}} U_{sys} &= \sum_{\substack{\kappa,\lambda,\mu \\ \in S_{klm}}} -\nabla_{r_{klm}} U_{\kappa\lambda\mu} \\ &= \sum_{\substack{\kappa,\lambda,\mu \\ \in S_{klm}}} f_{klm}|_{\kappa\lambda\mu} \\ &= \sum_{\substack{\kappa,\lambda,\mu \\ \in S_{klm}}} \left(w_{\kappa\lambda\mu}^{(I)} f_{klm}|_{\kappa\lambda\mu}^{(I)} + w_{\kappa\lambda\mu}^{(II)} f_{klm}|_{\kappa\lambda\mu}^{(II)} \right) \\ &= \sum_{\substack{\kappa,\lambda,\mu \\ \in S_{klm}}} \left(w_{\kappa\lambda\mu}^{(I)} \left(\frac{1}{8} \sum_{s=0}^7 f_{klm}|_{\kappa\lambda\mu}^{(I)(s)} \right) + w_{\kappa\lambda\mu}^{(II)} \left(\frac{1}{8} \sum_{s=0}^7 f_{klm}|_{\kappa\lambda\mu}^{(II)(s)} \right) \right) \end{aligned} \quad (3.40)$$

The force acting on a micromechanical node due to one of its bistable, surrounding nanocells, is a weighted average of contributions from both metastable states of the nanocell. The normalised thermodynamic weights $w_{\kappa\lambda\mu}^{(I)}$ and $w_{\kappa\lambda\mu}^{(II)}$ are easily determined by applying the chain rule to Eq. 3.37.

$$\begin{aligned} w_{\kappa\lambda\mu}^{(I)} &= \frac{\exp\left(-\frac{U_{\kappa\lambda\mu}^{(I)}}{k_B T_{\kappa\lambda\mu}^*}\right)}{\exp\left(-\frac{U_{\kappa\lambda\mu}^{(I)}}{k_B T_{\kappa\lambda\mu}^*}\right) + \exp\left(-\frac{U_{\kappa\lambda\mu}^{(II)} + \Delta F_{\kappa\lambda\mu}^{(I)\rightarrow(II)}}{k_B T_{\kappa\lambda\mu}^*}\right)} \\ w_{\kappa\lambda\mu}^{(II)} &= \frac{\exp\left(-\frac{U_{\kappa\lambda\mu}^{(II)} + \Delta F_{\kappa\lambda\mu}^{(I)\rightarrow(II)}}{k_B T_{\kappa\lambda\mu}^*}\right)}{\exp\left(-\frac{U_{\kappa\lambda\mu}^{(I)}}{k_B T_{\kappa\lambda\mu}^*}\right) + \exp\left(-\frac{U_{\kappa\lambda\mu}^{(II)} + \Delta F_{\kappa\lambda\mu}^{(I)\rightarrow(II)}}{k_B T_{\kappa\lambda\mu}^*}\right)} \end{aligned} \quad (3.41)$$

Although a bistable nanocell in the first metastable state can transition smoothly to the second metastable state and *vice versa*, one state typically dominates the behaviour of the nanocell. Near the equilibrium of the dominant state, the contribution of the other state to the forces acting on the micromechanical nodes is negligible, due to the exponential behaviour of the thermodynamic weights $w_{\kappa\lambda\mu}^{(I)}$ and $w_{\kappa\lambda\mu}^{(II)}$.

Finally, Newton's second law or Hamilton's equations are used to obtain the an equation of motion for each node.

$$\begin{aligned}\dot{\mathbf{p}}_{klm} &= \mathbf{f}_{klm} = \sum_{\substack{\kappa, \lambda, \mu \\ \in S_{klm}}} \mathbf{f}_{klm}|_{\kappa\lambda\mu} = \sum_{\substack{\kappa, \lambda, \mu \\ \in S_{klm}}} \left(w_{\kappa\lambda\mu}^{(I)} \mathbf{f}_{klm}|_{\kappa\lambda\mu}^{(I)} + w_{\kappa\lambda\mu}^{(II)} \mathbf{f}_{klm}|_{\kappa\lambda\mu}^{(II)} \right) \\ \dot{\mathbf{r}}_{klm} &= \frac{\mathbf{p}_{klm}}{m_{klm}} = \mathbf{v}_{klm}\end{aligned}\quad (3.42)$$

The mass of node (k, l, m) is, once again, calculated by summing one eighth of the mass of each surrounding nanocell.

4

Implementing and validating the micromechanical model

We have implemented the micromechanical model in a Python package named MicMec, which is publicly available [41]. With MicMec, we hope to prove the validity and consistency of the micromechanical model. In concrete terms, MicMec provides functionality to build micromechanical systems, to perform simulations and to analyse and visualise results. While it is possible in theory to perform Monte Carlo simulations with the micromechanical model as well, the current implementation only supports molecular dynamics simulations.

4.1 **MicMec**

4.1.1 **Preprocessing**

As we have previously explained, a micromechanical system can be edited and adapted easily. Any nanocell and its elastic properties are transferable to any other micromechanical system. The user of the micromechanical model is granted a high amount of freedom to choose the layout of the system and to determine which types of nanocells can accurately represent the heterogeneities and spatial disorder of a realistic MOF, as shown schematically in Figure 3.1.

In order to facilitate designing, building and storing such a micromechanical system, we have developed the Micromechanical Model Builder (Figure 4.1). This is a small Python application that allows its users to create a micromechanical system with only a few clicks. As demonstrated in Figure 4.1, users can select one nanocell type at a time from the dropdown menu, *e.g.*, the **fcu** topology of UiO-66. They can then mark every location in the grid where the selected type of nanocell is supposed to be located. Clicking the boxes is much less time-consuming than filling in a three-dimensional array manually. Furthermore, a unique colour is assigned to each type, *e.g.*, red to **fcu** and blue to **reo**. These colours are stored in the same location as the types such that they can be used later, for instance in the postprocessing stage, when comparing visualisations between **fcu** and **reo**.

Users can add a new nanocell type to the current session, or remove an existing type, by loading or removing its file from the application. A new type is easy to create, but requires some manual input outside of the application. Users have to create a file for each type they want to use. For each type, they have to specify an equilibrium cell matrix, an elasticity tensor, a free energy value (which defaults to zero) and an effective temperature (which defaults to 300 K). Specifying which MOF the type represents and to which topology it belongs, is recommended, but optional. The MicMec package provides some additional scripts to make the process of creating new types even easier.

The output of the application is a structure file containing all relevant information about the system: the initial positions of the micromechanical nodes, the parameters of each nanocell, a list of neighbours for each node, a list of neighbours for each nanocell and the vectors that span the simulation domain. These vectors are only specified when periodic boundary conditions apply. Most importantly, the entire structure file is generated automatically, requiring very little user input. An interesting aspect of the application is how it determines the initial positions of the micromechanical nodes. The application assumes that all of the nanocells in the simulation domain are equally large at this point. The most common type of nanocell in the grid, *e.g.*, **fcu**, determines the dimensions of every other nanocell. The micromechanical nodes are then located, as always, on the vertices of the nanocells. During a simulation or an optimisation run, the effect of choosing these initial positions should become negligible as the system equilibrates and relaxes into more favourable configurations.

4.1.2 Core routines

The core routines of MicMec are responsible for micromechanical simulations and optimisations. The architecture of these core routines is intentionally similar to the architecture of Yaff. Yaff (Yet Another Force Field) is a Python package developed at the Center for Molecular Modeling (CMM) for the purpose of performing simulations and optimisations with atomistic force fields [42]. As such, users of Yaff should be instantly familiar with the important features of MicMec.

First and foremost, there is a System object. A System can be created manually, but it can also be read from a structure file created by the Micromechanical Model Builder. In Yaff, a System usually represents

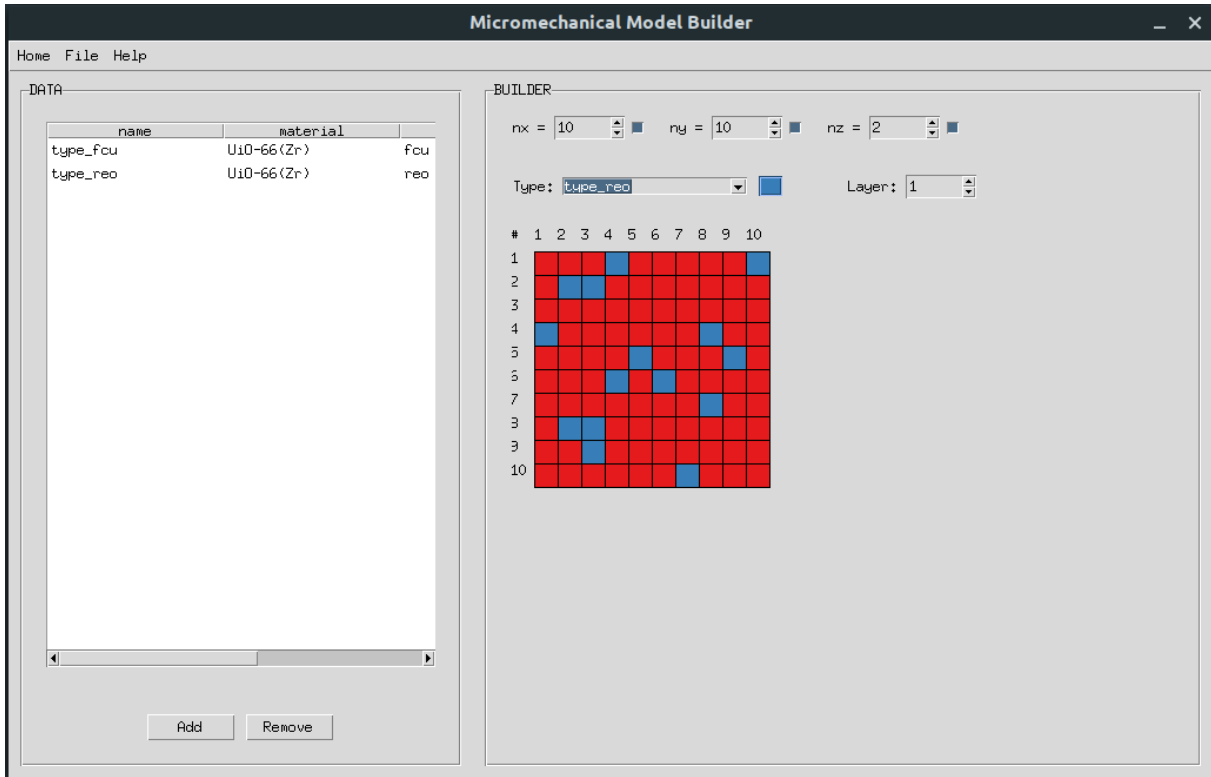


Figure 4.1: The Micromechanical Model Builder, a Python application to construct a micromechanical system from a collection of nanocell types. In the left-hand pane, nanocell types can be added to or removed from the current session. In the right-hand pane, a three-dimensional, rectangular grid represents the micromechanical system. The user can select appropriate dimensions for the grid and toggle periodic boundary conditions on or off. By selecting a nanocell type and subsequently clicking its intended locations in the grid, the user can build their own system. In this example, the red cells belong to the `fcu` type and the blue cells belong to the `reo` type.

a nanocell or a supercell. In MicMec, a System represents a network of coarse-grained nodes. Each three-dimensional nanocell in the System's grid has eight neighbouring nodes, one for each vertex of the nanocell, which is true for every micromechanical system. However, a micromechanical node does not necessarily have eight neighbouring nanocells. Nodes can be located on the surface of the grid, in a simulation domain with non-periodic boundary conditions. It is also allowed that some nanocells are missing from the grid to mimic mesoporosity. The nodes surrounding empty cells have fewer neighbors, a smaller mass and there will be fewer forces acting on them. Both of these edge cases have been taken into account in the code.

The System object contains the parameters of the micromechanical system as well. The storage and implementation of these parameters is generalised for any kind of micromechanical system. Each nanocell is equipped to deal with multiple metastable states, potentially even more than two, and its free energy

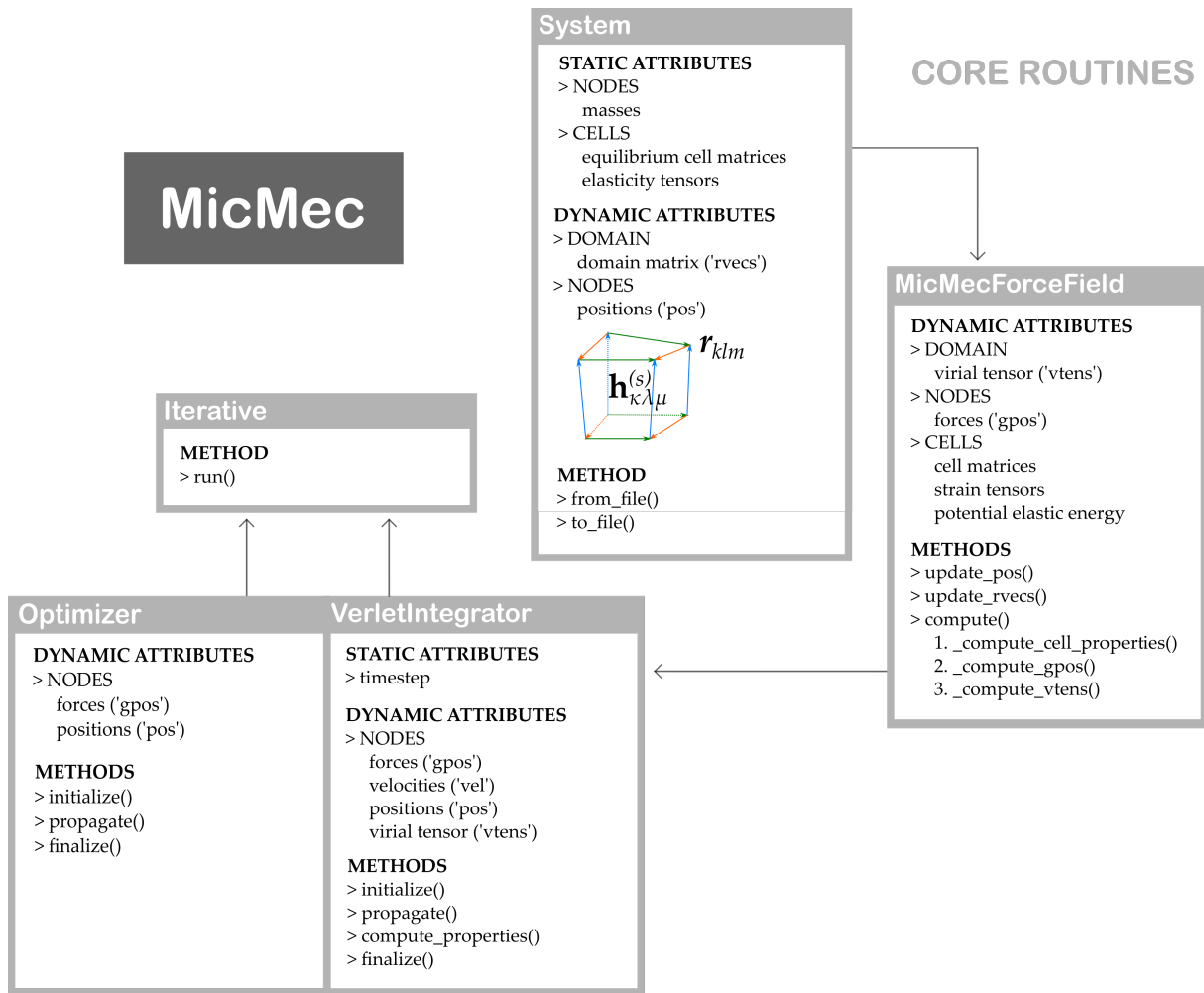


Figure 4.2: Overview of the core routines of MicMec, our implementation of the micromechanical model. These are inspired by Yaff, a Python package for the use of atomistic force fields, developed at the CMM [42].

surface, as a function of appropriately chosen collective variables, is fitted to an atomistic reference profile by means of an effective temperature.

Each metastable state of the nanocell corresponds to a type, with an equilibrium cell matrix, an elasticity tensor, and a free energy value. In the case of a unistable nanocell, its free energy value should be set to zero and its effective (atomic) temperature should assume an arbitrary, strictly positive real value.

Secondly, there is a `MicMecForceField` which represents the forces acting on the `System`. In Yaff, these are atomistic force fields. Atomistic force fields are usually split up into contributions, corresponding to different kinds of atomic interactions [27]. In MicMec, there is only one type of interaction, namely the micromechanical interaction between a node and its surrounding nanocells, which are all coupled to other nodes. In other words, the only contribution to the potential energy of the micromechanical

system, in the absence of external fields, is the elastic deformation energy of the nanocells. The partial derivatives of the total potential energy lead to an expression for the forces acting on the nodes, as has been explained in Section 3.5. In Figure 4.2, in the block titled ‘MicMecForceField’, the calculations to obtain the forces acting on the nodes and the virial tensor of the domain are listed as a sequence of methods. The first method, ‘_compute_cell_properties()’, iterates over each nanocell, calculating each nanocell representation, each strain tensor representation and each potential energy contribution. The second method, ‘_compute_gpos()’, then iterates over each node, summing up force contributions from each surrounding nanocell. The third method, ‘_compute_vtens()’, iterates over each nanocell again, to compute the virial tensor.

Thirdly, there is either a VerletIntegrator object to numerically integrate the equations of motion of the system, or an Optimizer object to find the optimal geometry of the system. The implementation of the velocity Verlet algorithm here is essentially identical to the implementation in Yaff. The Optimizer has inherited its conjugate gradient and quasi-newtonian optimisation algorithms from Yaff. The code has been adapted slightly to avoid some confusing nomenclature and conflicts. The term ‘cell’ is especially troublesome. In Yaff, ‘cell’ refers to the entire simulation domain, but in a micromechanical context it denotes only a single part of the system, a single nanocell. Hence, we prefer to use the term ‘domain’ when referring to the entire simulation domain of a micromechanical system.

The black arrows connecting the blocks in Figure 4.2 represent the order in which the objects are initialised at the start of a standard simulation or optimisation run. MicMecForceField, for instance, needs a System object, otherwise it does not know which forces to calculate or which elastic properties to use. Similarly, the VerletIntegrator and the Optimizer need the MicMecForceField. The final block in the pipeline is the Iterative block, which effectively starts the simulation.

In the velocity Verlet algorithm, the VerletIntegrator starts from the assumption that there are some forces acting on the micromechanical nodes. It proceeds to calculate the velocities of the nodes at half a timestep, as well as their positions at a complete timestep. Then, the VerletIntegrator inserts these new positions into a call to the MicMecForceField. The MicMecForceField, not the VerletIntegrator, updates the System’s positions, completely analogous to how, in real life, a force displaces an object. The VerletIntegrator calls the MicMecForceField again when it requires the forces acting on the nodes at their updated positions. The MicMecForceField responds by computing these new forces. The forces are updated in the MicMecForceField object and in the VerletIntegrator. Finally, the VerletIntegrator uses the forces to calculate the velocities of the nodes at a complete timestep. The forces are stored to be used in the next iteration.

4.1.3 Temperature and pressure control

The velocity Verlet algorithm numerically integrates the equations of motion specified in Section 3.5 and preserves the total energy of the micromechanical system, E . The number of micromechanical nodes, N ,

and the volume of the simulation domain, V , are fixed by default. Therefore, a default micromechanical simulation is performed in the (N, V, E) ensemble, also known as the microcanonical ensemble [25].

MicMec provides the option to add hooks to the Optimizer and the VerletIntegrator. These hooks are user-specified objects that may edit, process or store information from the System and the MicMecForceField while the optimisation or the MD simulation is running. Yaff and MicMec contain several thermostats and barostats as hooks to be used in an MD simulation. These thermostats and barostats allow the user to control the temperature and the pressure of a micromechanical system. During a simulation, the temperature and the pressure are still allowed to fluctuate, but the temperature distribution and the pressure distribution should converge to their intended values. The velocity Verlet algorithm is then no longer sampling the (N, V, E) ensemble [25]. If the volume and the shape of the simulation domain are fixed and the temperature of the system is controlled, then it is sampling the (N, V, T) ensemble, also known as the canonical or isochoric-isothermal ensemble. If the volume and shape of the simulation domain are allowed to fluctuate and the pressure and the temperature of the system are controlled, then it is sampling the (N, P, T) ensemble, also known as the isothermal-isobaric ensemble [25].

The thermostats of MicMec and Yaff can be deterministic, like the Nosé-Hoover chain thermostat, or stochastic, like the Langevin thermostat. Similarly, the barostats can be deterministic, like the Martyna-Tuckerman-Tobias-Klein barostat, or stochastic, like the Langevin barostat. All of the implemented barostats use the virial tensor of the simulation domain in their calculations. The virial tensor, which is calculated by the MicMecForceField, is therefore crucial to enable simulations in the (N, P, T) ensemble. It must be noted that the forces acting on the micromechanical nodes are many-body interactions, contrary to the usual pair potential interactions in an atomistic force field. The standard formula for the virial tensor, as it is implemented in Yaff, is therefore not sufficient.

Fortunately, a rigorous derivation of the virial tensor \mathbf{W} for many-body potentials does exist. In Ref. 43, the following expression is proposed.

$$\mathbf{W} = \sum_{\kappa, \lambda, \mu} \sum_{\substack{k, l, m \\ \in S_{\kappa \lambda \mu}}} \mathbf{r}_{klm} \otimes f_{klm}|_{\kappa \lambda \mu} \quad (4.1)$$

Here, \mathbf{r}_{klm} is the position vector of node (k, l, m) and $f_{klm}|_{\kappa \lambda \mu}$ is the contribution of nanocell (κ, λ, μ) to the force acting on node (k, l, m) . The symbol \otimes denotes the tensor product, defined as follows.

$$[\mathbf{r} \otimes \mathbf{f}]_{ij} = r_i f_j \quad (4.2)$$

Eq. 4.1 must be implemented carefully. The position vector of node (k, l, m) is evaluated with respect to the nanocell (κ, λ, μ) . The nodes of a nanocell near one of the periodic boundaries can lie outside of the simulation domain. The minimum image convention must not be applied to the position vectors

of these nodes. Let us consider the node at $(0, 0, 0)$, which has periodic images near each corner of the simulation domain. In the nanocell at the origin of the grid, this node must be represented by \mathbf{r}_{000} . In general, however, this node must be represented by

$$\mathbf{r}_{000} + \mathbf{h}^T \mathbf{n}, \quad (4.3)$$

where the rows of \mathbf{h} are the \mathbf{a} , \mathbf{b} and \mathbf{c} cell vectors of the simulation domain and \mathbf{n} is a column vector of integers that identifies one of the periodic images of the domain.

4.1.4 Postprocessing

Postprocessing in MicMec is focused on analysing the results of MD simulations. Yaff already contains a complete toolbox of useful methods to plot the trajectories of temperature, pressure, volume, parameters of the simulation domain and energy contributions. Perhaps most useful are the methods that produce histograms of the pressure and temperature values. These histograms are an important measure to decide whether the results of an MD simulation can be used to estimate ensemble averages.

There is one important addition to the Yaff toolbox in MicMec: a method to calculate the elasticity tensor and the equilibrium matrix of the simulation domain. The elasticity tensor of a homogeneous micromechanical system should converge to the elasticity tensor of its nanocells. A method to calculate the elasticity tensor of the simulation domain has already been described in Section 3.3, where it was intended for the atomic structure of a single nanocell. Here, the simulation domain is filled with micromechanical nodes instead of atoms, but the procedure has not changed and Eq. 3.19 remains valid.

4.2 Validation

4.2.1 Testing the micromechanical model

Compared to an atomistic force field model, the micromechanical model reduces the number of degrees of freedom of a single nanocell to an even higher degree than other coarse-grained force fields. Therefore, a certain loss of information is expected and inevitable. Determining whether the predictions made by the model are still useful despite the loss of information, is crucial for any coarse graining approach. However, before we can assess qualitative aspects of the model, such as its usefulness and its reliability, we must provide quantitative results that can be validated and checked for consistency.

First and foremost, the micromechanical equations of motions have to be derived correctly. In Section 3.5, an analytical expression has been proposed for the total force acting on a node due to its surrounding nanocells. This equation can be validated by using a simple $2 \times 2 \times 2$ test system with periodic boundary conditions, consisting of eight nanocells and eight nodes, as presented in Figure 4.3a.

The eight nanocells have identical elastic properties. The equilibrium cell matrix of each nanocell in the test system is defined as

$$\mathbf{h}_0(\text{test}) = \begin{bmatrix} 10.0 & 0.0 & 0.0 \\ 0.0 & 10.0 & 0.0 \\ 0.0 & 0.0 & 10.0 \end{bmatrix} \text{\AA}, \quad (4.4)$$

where the cell length of 10 Å has been chosen arbitrarily. Each node in the test system has the same mass, which is defined with respect to the mass of an electron, $m = 1.0 \cdot 10^7 m_e$.

The elasticity tensor of the nanocells in the test system slightly resembles the elasticity tensor of the fcu topology of the cubic UiO-66(Zr) material, but otherwise it does not stem from any kind of simulation or experiment.

$$\mathbf{C}_0(\text{test}) = \begin{bmatrix} 50.0 & 30.0 & 30.0 & 0 & 0 & 0 \\ 30.0 & 50.0 & 30.0 & 0 & 0 & 0 \\ 30.0 & 30.0 & 50.0 & 0 & 0 & 0 \\ 0 & 0 & 0 & 10.0 & 0 & 0 \\ 0 & 0 & 0 & 0 & 10.0 & 0 \\ 0 & 0 & 0 & 0 & 0 & 10.0 \end{bmatrix} \text{GPa} \quad (4.5)$$

The advantage of the test system is that its equilibrium state is known exactly before any calculations need to be performed. If the eight nodes of the test system lie on a cubic grid with a spacing of 10.0 Å, then none of the nanocells experience any mechanical stress. In other words, the potential energy of the test system in its equilibrium state is zero.

Furthermore, the test system enables us to investigate the behaviour of the total potential energy of the system as a function of the nodes. Consider the situation where seven of the eight nodes are kept fixed at their equilibrium positions and one node is shifted. A set of static calculations can provide the total potential energy of the system at each position of the shifted node. Such a procedure is also known as a *static scan*.

$$U_{\text{sys}} = U_{\text{sys}}(\mathbf{r}_1, \dots, \mathbf{r}_7, \mathbf{r}) \equiv U_{\text{sys}}(\mathbf{r}) \quad (4.6)$$

The test system has a high degree of symmetry. As a consequence, the potential well experienced by the shifted node, shown in Figure 4.3b, is spherically symmetric. The symmetry of the potential well can be broken by introducing different types of nanocells in the system or by terminating the system with non-periodic boundaries.

In Section 3.5, an analytical expression has been derived to describe the force acting on a node due to its surrounding nanocells. The derivation of this analytical expression is not trivial, so there can be some uncertainty about whether it is correct. With MicMec, we have been able to prove that it is indeed correct, by calculating both the analytical expression for the force acting on the shifted node and the numerical derivative of the total potential energy with respect to the coordinates of the shifted node.

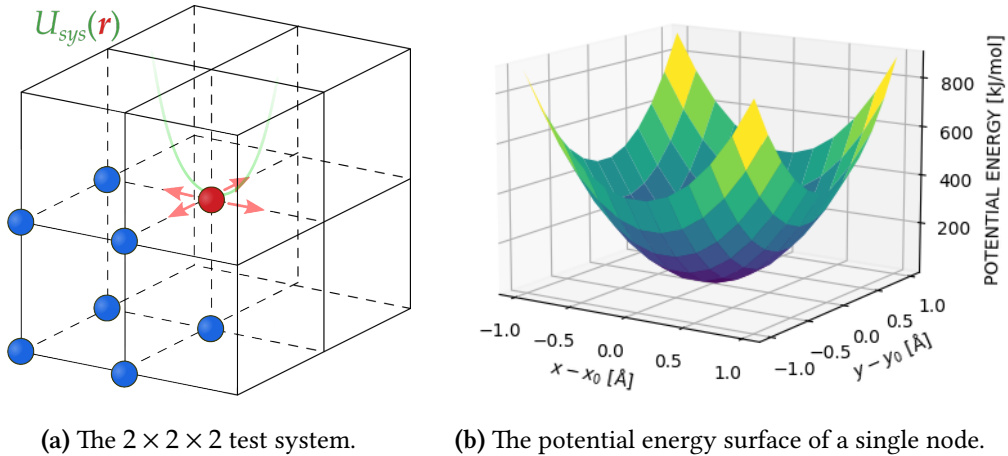


Figure 4.3: A $2 \times 2 \times 2$ test system, presented in (a), is used to validate the micromechanical equations of motion. Due to periodic boundary conditions, the model only tracks eight nodes. Seven of the eight nodes are kept fixed, while the eighth is being moved around in a broad scanning range. This static scan results in a potential energy surface ($U_{sys}(\mathbf{r})$), as shown in (b). At each location, the force acting on the node is recorded as well.

The negative numerical derivative must be the true force, otherwise the total potential energy is not correct. Then, the analytical expression simply needs to match the negative numerical derivative. In other words, the force needs to match the negative gradient of the total potential energy. Figure 4.4 proves that it indeed does.

In Section 3.3, a method to calculate the bulk modulus of an atomic structure was mentioned. The same procedure and the same formula can be applied to a micromechanical system. We have rewritten the formula in terms of the relative volume and the total energy density.

$$K = V_0 \frac{\partial^2 E}{\partial V^2} \Big|_{V_0} = \frac{\partial^2 (E/V_0)}{\partial (V/V_0)^2} \Big|_{V_0} \quad (4.7)$$

So, the bulk modulus is related to the curvature of the energy-versus-volume equation of state at 0 K, which can be constructed by performing a *relaxed scan*. In this relaxed scan, the volume of the test system is increased or decreased by small increments. At each increment, a full optimisation of the micromechanical nodes is performed and the total potential energy is recorded. The result is shown in Figure 4.5.

We can conclude from Figure 4.5 that the bulk modulus of the test system is reproduced exactly by these static calculations. As expected, the bulk modulus of a homogeneous $2 \times 2 \times 2$ or $3 \times 3 \times 3$ test system is equal to the bulk modulus of an individual nanocell.

$$K(\text{test}) = \frac{1}{3}(50.0 + 30.0 + 30.0) \text{ GPa} = 36.7 \text{ GPa} \quad (4.8)$$

$$K(2 \times 2 \times 2) = K(3 \times 3 \times 3) = 36.7 \text{ GPa}$$

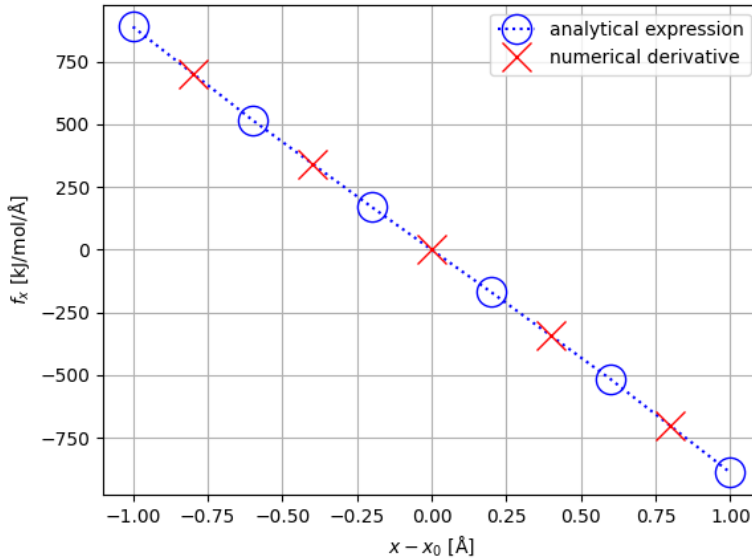


Figure 4.4: Comparing the negative numerical derivative of the total potential energy to the analytical expression for the force acting on a node. The result is Hooke’s law and a perfect match between the two, indicating that the analytical expression has been derived correctly.

However, Figure 4.5 reveals another important fact about the current implementation of the micromechanical model. When the $3 \times 3 \times 3$ test system is compressed to less than 90% of its initial volume, it is able to reach a lower potential energy density than the $2 \times 2 \times 2$ test system. The resulting configuration of nodes depends on the values of the elasticity tensor. For this particular choice of elasticity tensor, the $3 \times 3 \times 3$ system seems to *crumple* at less than 90% of its initial volume, breaking its own symmetry by settling into a configuration where a few of its nanocells are compressed to a larger extent than the other nanocells. The $2 \times 2 \times 2$ system has fewer degrees of freedom and cannot settle into the same configuration as the $3 \times 3 \times 3$ system. This, however, seems to contradict our physical intuition. The symmetry of the system should not spontaneously break.

The root cause of this issue lies at the very heart of the current implementation of the micromechanical model, in the calculation of the potential energy of a nanocell (Eq. 3.25) and in the subsequent calculation of the forces acting on a micromechanical node (Eq. 3.29). It is assumed in Eq. 3.25 that the potential energy of a nanocell, or at least the potential energy of one of its representations, depends on the instantaneous volume $V_{\kappa\lambda\mu}^{(s)}$ of its nanocell representation.

$$U_{\kappa\lambda\mu}^{(s)} = \frac{1}{2} V_{\kappa\lambda\mu}^{(s)} \left(\boldsymbol{\epsilon}_{\kappa\lambda\mu}^{(s)} \right)^T : \mathbf{C}_{\kappa\lambda\mu,0} : \left(\boldsymbol{\epsilon}_{\kappa\lambda\mu}^{(s)} \right) \quad (4.9)$$

The instantaneous volume of the nanocell representation is defined as the determinant of its cell matrix.

$$V_{\kappa\lambda\mu}^{(s)} = \det(\mathbf{h}_{\kappa\lambda\mu}^{(s)}) \quad (4.10)$$

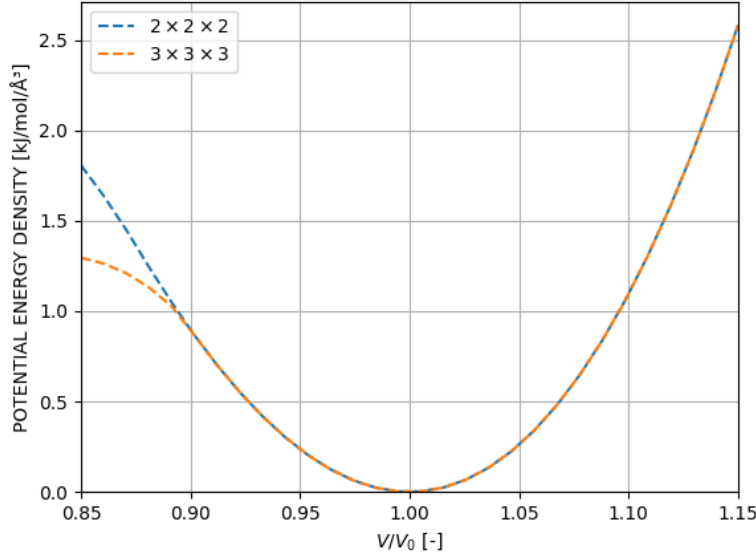


Figure 4.5: The potential energy density of a homogeneous $2 \times 2 \times 2$ test system and a homogeneous $3 \times 3 \times 3$ test system, at 0 K, as a function of the relative volume V/V_0 , where V_0 is the equilibrium volume. At equilibrium, the curvature of this profile is equal to the bulk modulus of the test system (36.7 GPa).

This is opposed to an alternative method, whereby the instantaneous volume of the representation is replaced by the equilibrium volume of the nanocell, $V_{\kappa\lambda\mu,0}$.

$$U_{\kappa\lambda\mu}^{(s)} = \frac{1}{2} V_{\kappa\lambda\mu,0} \left(\boldsymbol{\epsilon}_{\kappa\lambda\mu}^{(s)} \right)^T : \mathbf{C}_{\kappa\lambda\mu,0} : \left(\boldsymbol{\epsilon}_{\kappa\lambda\mu}^{(s)} \right), \quad (4.11)$$

The equilibrium volume of the nanocell is defined as the determinant of the equilibrium cell matrix.

$$V_{\kappa\lambda\mu,0} = \det(\mathbf{h}_{\kappa\lambda\mu,0}) \quad (4.12)$$

This detail has ramifications for the calculation of the forces acting on a node. As shown in Eq. 3.29, the first term of that expression is proportional to the gradient of the instantaneous volume of a representation. If the instantaneous volume is replaced by the equilibrium volume, then the prefactor of Eq. 3.29 changes to a constant value and the first term of the expression vanishes completely, leading to the following, alternative expression for the forces acting on a node.

$$\begin{aligned} f_{klm}\Big|_{\kappa\lambda\mu}^{(s)} = & -\frac{1}{2} \det(\mathbf{h}_{\kappa\lambda\mu,0}) \left[\left(\nabla_{r_{klm}} \boldsymbol{\epsilon}_{\kappa\lambda\mu}^{(s)} \right)^T : \mathbf{C}_{\kappa\lambda\mu,0} : \left(\boldsymbol{\epsilon}_{\kappa\lambda\mu}^{(s)} \right) \right. \\ & \left. + \left(\boldsymbol{\epsilon}_{\kappa\lambda\mu}^{(s)} \right)^T : \mathbf{C}_{\kappa\lambda\mu,0} : \left(\nabla_{r_{klm}} \boldsymbol{\epsilon}_{\kappa\lambda\mu}^{(s)} \right) \right] \end{aligned} \quad (4.13)$$

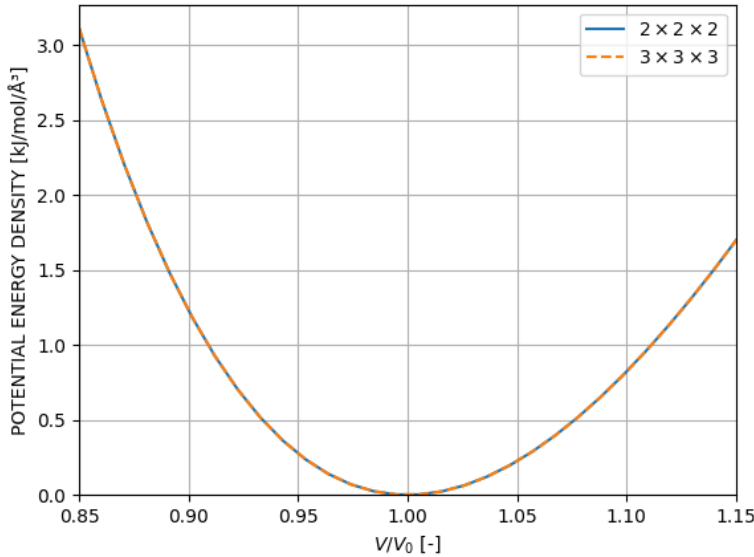


Figure 4.6: The potential energy density of a homogeneous $2 \times 2 \times 2$ test system and a homogeneous $3 \times 3 \times 3$ test system, at 0 K, as a function of the relative volume V/V_0 , where V_0 is the equilibrium volume. This is the result of using an alternative version of the micromechanical model, whereby the instantaneous volume of the nanocell representation is replaced by the equilibrium volume of the nanocell in Eq. 3.25, resulting in a different set of equations of motion. At equilibrium, the curvature of this profile is still equal to the bulk modulus of the test system (36.7 GPa).

The alternative method leads to an alternative energy-versus-volume equation of state, shown in Figure 4.6. This new equation of state is identical for the $2 \times 2 \times 2$ test system and the $3 \times 3 \times 3$ test system. Moreover, it still yields a correct prediction of the bulk modulus (36.7 GPa). The symmetry of the system is never broken.

Therefore, this alternative method is likely superior to the currently implemented method. The currently implemented method is part of the original version of the micromechanical model [29]. At the time of writing, it is no longer a realistic prospect to perform all simulations mentioned in this work again with the alternative method. Therefore, all simulations, figures and results mentioned in this work, except for Figure 4.6, have been obtained with the original method, which is currently part of MicMec. We only mention the alternative method as part of a future version of MicMec.

For small deviations from equilibrium we do not expect any problematic behaviour from the current version of MicMec. Like the $3 \times 3 \times 3$ test system, much larger systems will likely crumple during an optimisation. In theory, this could happen during an MD simulation as well, if the simulation domain is compressed to a significant degree by the action of a barostat. Further optimisations and MD

simulations in this work are restricted to $3 \times 3 \times 3$ systems, so it is not likely to happen.

4.2.2 Testing geometry optimisations

Besides performing molecular dynamics simulations, MicMec can optimise geometries. In other words, MicMec can find a configuration of micromechanical nodes and parameters of the simulation domain that results in at least a local minimum of the total potential energy. Sometimes, we refer to this minimum as the mechanical equilibrium.

The relaxed scan in the previous section has demonstrated that MicMec can, indeed, find an optimal geometry for the test system when its volume is perturbed. Our goal in this section is to validate a few optimised geometries qualitatively, by visualising the resulting configuration of nodes. Again, a test system can be used. We introduce a $3 \times 3 \times 3$ test system consisting of two nanocell types, a small and a large nanocell.

$$\mathbf{h}_0(\text{large}) = \begin{bmatrix} 10.0 & 0.0 & 0.0 \\ 0.0 & 10.0 & 0.0 \\ 0.0 & 0.0 & 10.0 \end{bmatrix} \text{\AA} \quad (4.14)$$

$$\mathbf{h}_0(\text{small}) = \begin{bmatrix} 5.0 & 0.0 & 0.0 \\ 0.0 & 5.0 & 0.0 \\ 0.0 & 0.0 & 5.0 \end{bmatrix} \text{\AA} \quad (4.15)$$

The elasticity tensors of these two types are identical. The smaller type is located at the centre of the $3 \times 3 \times 3$ grid. We have performed an optimisation of this structure by means of a quasi-Newton method, although a conjugate gradient method yields the same result. Additionally, we have performed the optimisation twice, once with periodic boundary conditions and once without.

The end results of both optimisations are shown in Figure 4.7. When periodic boundary conditions are disabled, the system contracts and curves slightly at its surface due to the smaller nanocell at the centre of the grid. Both results are in line with our qualitative expectations. The alternative version of the micromechanical model, as described in the previous section, remains an option to be explored in this context.

4.2.3 Testing molecular dynamics simulations

The Nyquist sampling theorem can be used to obtain an estimate of the maximal timestep in a micromechanical MD simulation. If only the elasticity tensors are known, then a characteristic length scale, such as the unit cell length of a nanocell, is still needed to calculate the highest frequency in the coarse-grained force field. As in the previous sections, a $3 \times 3 \times 3$ test system is being investigated. This homogeneous test system consists of 27 nanocells with identical elastic properties. In other words,

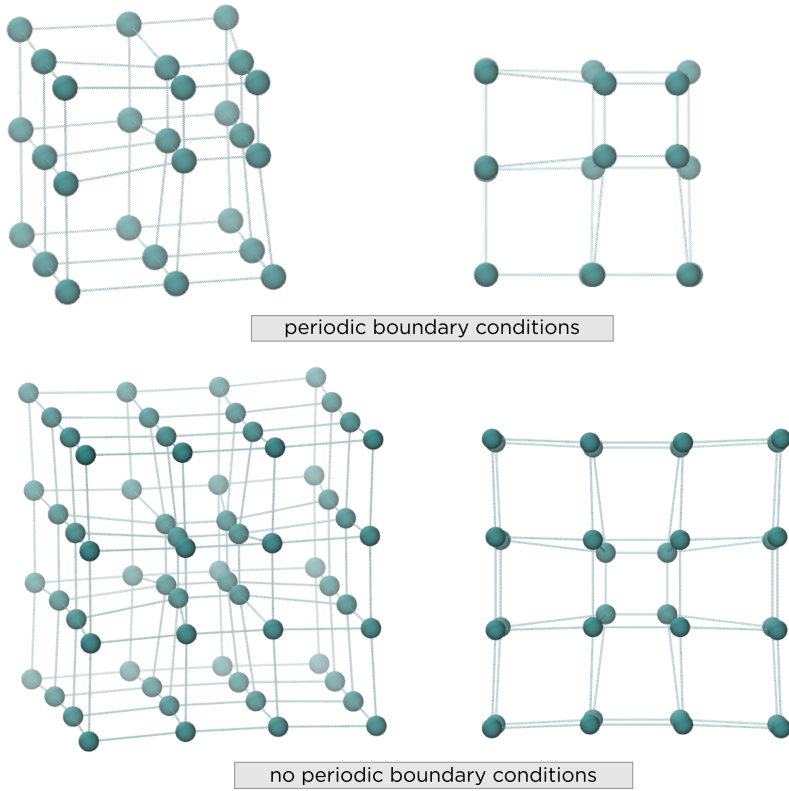


Figure 4.7: Optimised micromechanical structure of a \$3 \times 3 \times 3\$ test system. Two types of nanocells are present in this system: a small nanocell (Eq. 4.15) is located at the centre of grid and the rest of the grid is made up of large nanocells (Eq. 4.14). Depending on whether periodic boundary conditions are enabled or not, the end result of the optimisation differs. An orthographic view and a side view are shown.

these nanocells have the same elasticity tensor, defined in Voigt notation in Eq. 4.5, and the same equilibrium cell matrix, defined in Eq. 4.4. In the case of periodic boundaries, it contains 27 micromechanical nodes and therefore \$3 \times 27 - 3 = 78\$ Cartesian degrees of freedom. The initial positions of the nodes are also their mechanical equilibrium positions.

For this \$3 \times 3 \times 3\$ test system, the following estimate of the maximal timestep is obtained, by using the unit cell length (\$a = 10.0 \text{ \AA}\$), the mass of a node (\$m = 1.0 \cdot 10^7 \text{ m}_e\$) and the largest component of the elasticity tensor of Eq. 4.5 (\$C_{max} = 50.0 \text{ GPa}\$).

$$\Delta t_{max} = \pi \sqrt{\frac{m_{min}}{C_{max}a}} = 1.34 \text{ ps} \quad (4.16)$$

However, a force constant can also be calculated from Hooke's law, as Figure 4.4 suggests.

$$\Delta t_{max} = \pi \sqrt{\frac{m_{min}}{k_{max}}} = 0.79 \text{ ps} \quad (4.17)$$

The previous estimate and the current estimate share the same order of magnitude, which indicates that the unit cell length is indeed a good measure of the length scale. The actual upper bound for the timestep is lower than both of the estimates by a factor of three to four, which is a known phenomenon in molecular dynamics simulations, where the actual timestep is usually decreased by a safety factor of ten from the theoretical maximum predicted by the Nyquist theorem. Figure 4.8 demonstrates that the total energy of the system, which should be conserved in the (N, V, E) ensemble, starts to fluctuate and deviates severely from its supposed value when the timestep is increased to 0.4 ps and 0.5 ps. An even longer timestep of 0.6 ps immediately leads to a divergent energy.

Even a safe timestep, such as 0.1 ps, is still a factor of two hundred larger than the usual timestep of 0.5 fs for atomistic force field simulations, which highlights how useful our coarse graining procedure can be. In Figure 4.9, the separate contributions to the total energy are plotted as well. The potential energy cannot drop below zero, because that is the minimum both mathematically and physically for the micromechanical model. In an (N, V, E) simulation, the elastic potential energy of the nanocells increases at the cost of decreasing the kinetic energy of the nodes.

In conclusion, the (N, V, E) ensemble does indeed preserve the energy of the micromechanical test system. Now, more advanced molecular dynamics simulations can be investigated. We can employ the (N, P, T) ensemble to attempt to validate the micromechanical model even further.

Eq. 4.18 and Eq. 4.19 show the result of a calculation to obtain the equilibrium cell matrix and the elasticity tensor of the homogeneous $3 \times 3 \times 3$ test system. The elasticity tensor of the $3 \times 3 \times 3$ system should match the original elasticity tensor of the individual nanocells (Eq. 4.5).

$$\mathbf{h}_0(3 \times 3 \times 3) = \begin{bmatrix} 29.2 & 1.6 & 2.3 \\ -1.0 & 28.9 & -4.3 \\ -3.0 & 3.9 & 29.3 \end{bmatrix} \text{ Å} \quad (4.18)$$

$$\mathbf{C}_0(3 \times 3 \times 3) = \begin{bmatrix} 27.1 & 5.3 & -1.5 & 2.9 & -0.8 & -1.3 \\ 5.3 & 20.7 & 4.4 & -0.3 & -0.6 & -0.2 \\ -1.5 & 4.4 & 29.7 & -3.1 & -1.0 & -1.2 \\ 2.9 & -0.3 & -3.1 & 12.9 & -0.3 & -1.3 \\ -0.8 & -0.6 & -1.0 & -0.3 & 15.1 & 3.1 \\ -1.3 & -0.2 & -1.2 & -1.3 & 3.1 & 9.8 \end{bmatrix} \text{ GPa} \quad (4.19)$$

This calculation is based on a molecular dynamics simulation at 0.0 MPa and 300.0 K, using a Nosé-Hoover chain thermostat with three beads and a Martyna-Tuckerman-Tobias-Klein barostat. The timestep

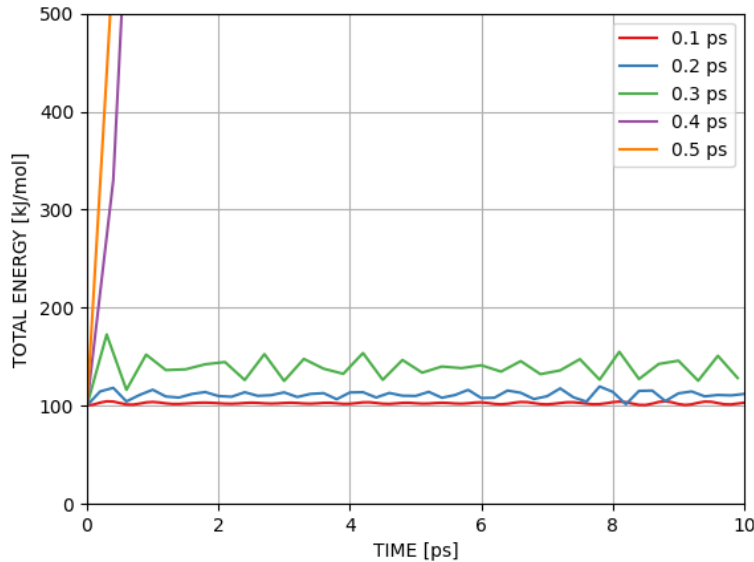


Figure 4.8: Sweeping the timestep of a molecular dynamics simulation in the (N, V, E) ensemble, using the micromechanical model. The initial velocities of the nodes of the $3 \times 3 \times 3$ test system are randomly picked from a Maxwellian distribution at 300 K. The same initial velocities are used in each run of the simulation. For a timestep of 0.4 ps and 0.5 ps, the energy deviates significantly from its intended value. For the stable timesteps, no energy drift is observed.

of the simulation was set to 70.0 fs, the time constant of the thermostat to 7.0 ps and the time constant of the barostat to 70.0 ps. We chose the timestep 70.0 fs with a broad safety margin, in order to avoid most sampling errors, even though larger timesteps are possible. One million Verlet steps were calculated, for a total simulation time of 70.0 ns. Figure 4.10 shows the result of the pressure and temperature control of this MD simulation. The calculation of the compliance tensor and, subsequently, the elasticity tensor, is based on Eq. 3.19.

Unfortunately, the homogeneous $3 \times 3 \times 3$ test system appears to have different elastic properties than its constituent nanocells. Indeed, there seems to be a large difference between the elasticity tensor of the system (the output of the model) and the elasticity tensor of an individual nanocell (the input of the model), as the elements of Eq. 4.19 clearly do not match the elements of Eq. 4.5.

A similar calculation has been performed, based on an MD simulation at 0.0 MPa and 300.0 K, using instead a Langevin thermostat and a Langevin barostat. This MD simulation appears to achieve a better control over the temperature distribution of the system than the previous MD simulation, as a comparison between Figure 4.11 and Figure 4.10 reveals. The resulting equilibrium cell matrix and elasticity

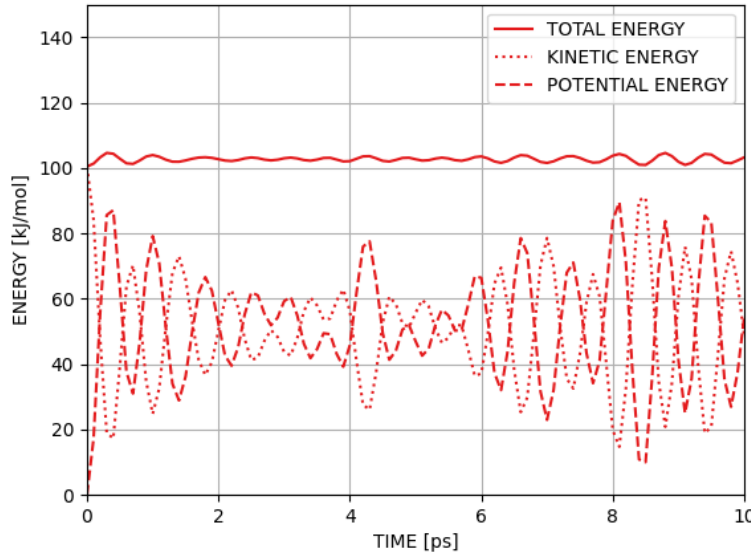


Figure 4.9: A molecular dynamics simulation of the $3 \times 3 \times 3$ test system in the (N, V, E) ensemble, using the micromechanical model and a timestep of 0.1 ps. The test system starts from its equilibrium configuration at zero potential energy. The initial velocities of the nodes are randomly picked from a Maxwellian distribution at 300 K. During the simulation, kinetic energy is exchanged for additional potential energy. The total energy shows short-term fluctuations due to the imperfect sampling of the fast movements in the system.

tensor are shown in Eq. 4.20 and Eq. 4.21.

$$\mathbf{h}_0(3 \times 3 \times 3) = \begin{bmatrix} 30.0 & 0.2 & 1.2 \\ -0.2 & 30.0 & -0.4 \\ -1.2 & 0.4 & 30.0 \end{bmatrix} \text{\AA} \quad (4.20)$$

$$\mathbf{C}_0(3 \times 3 \times 3) = \begin{bmatrix} 167.1 & 103.0 & 105.2 & -0.3 & 1.9 & 0.2 \\ 103.0 & 169.4 & 103.2 & -0.8 & -1.1 & 0.6 \\ 105.2 & 103.2 & 167.0 & 1.0 & -0.7 & -0.8 \\ -0.3 & -0.8 & 1.0 & 13.0 & 0.4 & -0.5 \\ 1.9 & -1.1 & -0.7 & 0.4 & 13.0 & -0.4 \\ 0.2 & -0.6 & -0.8 & -0.5 & -0.4 & 12.1 \end{bmatrix} \text{GPa} \quad (4.21)$$

Unfortunately, this elasticity tensor is inconsistent with the previous result and still deviates significantly from the elasticity tensor of a single nanocell, as the elements of Eq. 4.5 match neither Eq. 4.19 or Eq. 4.21. To put it simply, the elasticity tensor of the system does not converge properly.

There can be several reasons why the elasticity tensor of the homogeneous $3 \times 3 \times 3$ test system does not converge properly. In theory, the elasticity tensor of the system may change due to the finite tempera-

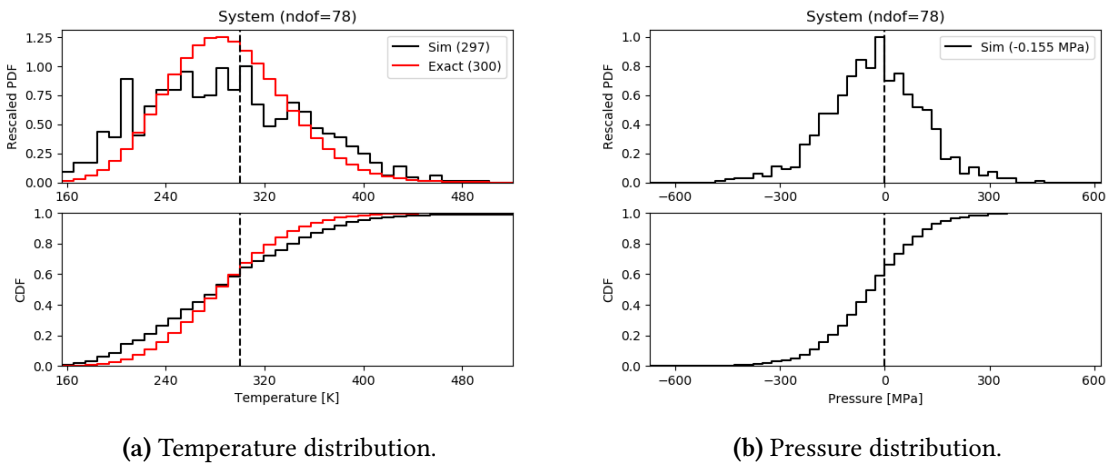


Figure 4.10: Histograms of pressure and temperature, resulting from a molecular dynamics simulation of a $3 \times 3 \times 3$ test system in the (N, P, T) ensemble, with a timestep of 70.0 fs and a simulation time of 70.0 ns. The temperature was set to 300.0 K and the pressure was set to 0.0 MPa. The Nosé-Hoover chain thermostat and the Martyna-Tuckerman-Tobias-Klein barostat were used, with time constants of 7.0 ps and 70.0 ps, respectively.

ture of the simulation (300 K). In atomistic force field simulations, there is often a difference between the static elastic constants, measured at 0 K, and the dynamic elastic constants, measured at a finite temperature. In a similar fashion, the elasticity tensor of an individual nanocell in a micromechanical system is a static (albeit state-dependent) property and the elasticity tensor of the system, calculated from a micromechanical MD simulation, is a dynamic property.

However, the simulation with a deterministic thermostat and barostat combination produces a different result than the simulation with a stochastic thermostat and barostat combination, hinting at a more complicated problem. Ideally, both thermostat and barostat combinations should produce the same elasticity tensor. A suboptimal sampling of the (N, P, T) ensemble could also cause a deteriorated convergence of the elasticity tensors, but the pressure and temperature distributions of Figure 4.10 and Figure 4.11 seem to indicate that the ensemble is being sampled adequately in both simulations.

Instead, the non-zero off-diagonal elements appearing in the equilibrium cell matrices in Eq. 4.18 and Eq. 4.20 might be symptoms of the same convergence issue that plagues the elasticity tensors. In our initial experiments, rotations of the simulation domain were observed. Due to these rotations, the equilibrium cell matrix of the system (Eq. 4.18 and Eq. 4.20) did not converge to its intended value. Afterwards, we have avoided these rotations of the simulation domain by removing any non-zero angular momentum from the initial velocity distribution of the micromechanical nodes.

So, the simulation domain no longer rotates, but the convergence issue of the elasticity tensor has not been solved or explained. Either Eq. 3.19, which is being used to calculate the elasticity tensors, is

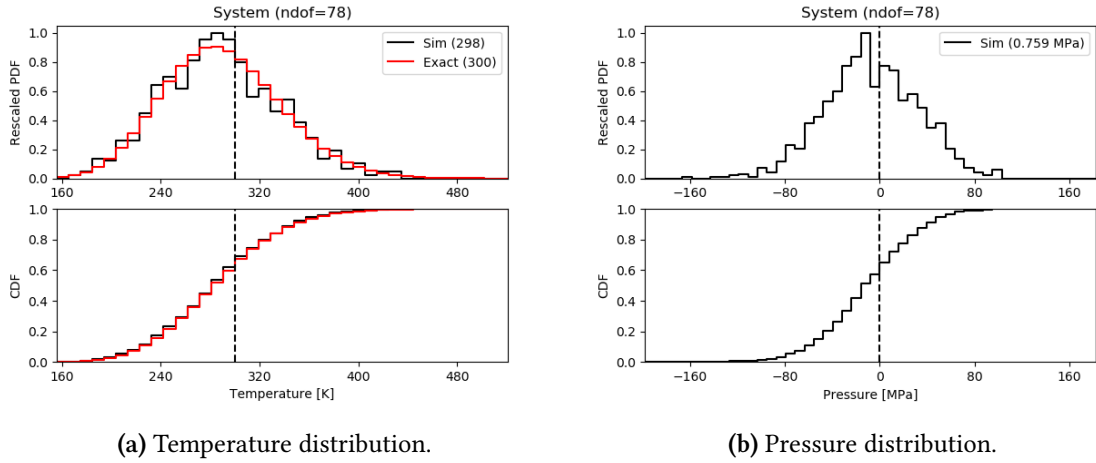


Figure 4.11: Histograms of pressure and temperature, resulting from a molecular dynamics simulation of a $3 \times 3 \times 3$ test system in the (N, P, T) ensemble, with a timestep of 70.0 fs and a simulation time of 70.0 ns. The temperature was set to 300.0 K and the pressure was set to 0.0 MPa. The Langevin thermostat and the Langevin barostat were used, with time constants of 7.0 ps and 70.0 ps, respectively.

inherently slow to converge, or some part of the micromechanical model, likely related to pressure control, is producing inconsistent results.

4.3 Conclusions

The implementation of the micromechanical model, MicMec, has been validated and tested, but there are a few remaining concerns. Firstly, the virial tensor is calculated differently in MicMec than in Yaff, according to a formula in Ref. 43. Fortunately, the pressure distribution of a micromechanical MD simulation, performed in the (N, P, T) ensemble with MicMec, converges to its intended value. This likely indicates that the virial tensor has been implemented correctly in MicMec and is appropriate for the micromechanical model. Secondly, we have proposed an alternative, potentially superior method to calculate the forces acting on a node, based on a different potential energy. It remains to be seen whether this alternative method should provide more accurate results than the currently implemented method. Thirdly, a micromechanical MD simulation does not produce a consistent elasticity tensor. The elasticity tensor of a homogeneous $3 \times 3 \times 3$ test system, which is calculated from the trajectory of the cell matrix of the simulation domain, does not match the elasticity tensor of an individual nanocell. We have not been able to pinpoint the cause of this convergence issue. We have been able to determine, however, that a relaxed potential energy scan of a micromechanical system produces a consistent and accurate value for the bulk modulus.

5

Correlated defects in UiO-66

Having validated a test system, we proceed to investigate a practical micromechanical system, based on an atomistic reference of UiO-66. The rigid MOF UiO-66 is modelled as a solid mixture of defect-free nanocells that adopt the **fcu** topology and cluster-defective nanocells that adopt the **reo** topology. Eight different configurations of cluster-defective nanocells, surrounded by defect-free nanocells, are simulated with MicMec and compared to a completely homogeneous, defect-free system. The aim of these experiments is to qualitatively, or semi-quantitatively, predict the mechanical behaviour of UiO-66.

5.1 Introduction

First, we provide a brief recap of relevant information about UiO-66, a rigid, exceptionally stable MOF. This information has been detailed in Section 1.2.1. It has been established that synthesised UiO-66 crystals may contain vacancy defects, specifically missing cluster defects and missing linker defects. The ideal, defect-free nanocell type of UiO-66 belongs to the **fcu** topology. As a result of vacancy defects, the symmetry of the ideal, defect-free nanocell is not preserved. The defective nanocell types of UiO-66 belong to the **bcu**, **reo** or **scu** topology, among others, and have been observed experimentally. Each nanocell type of UiO-66 has different elastic properties, *i.e.*, different parameters in the micromechanical model.

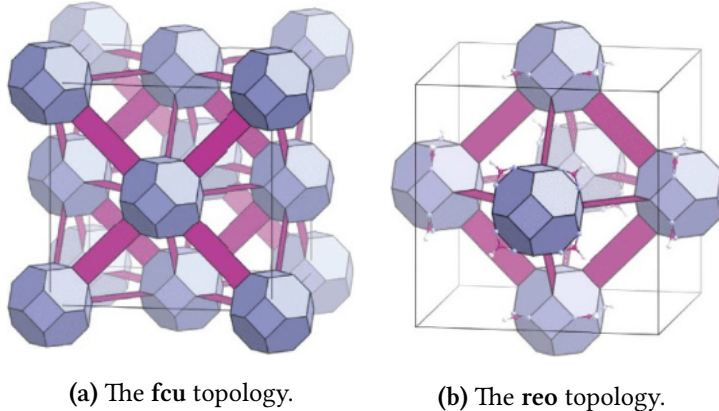


Figure 5.1: Simplified atomic structures of the defect-free nanocell type of UiO-66, the **fcu** topology, and a defective nanocell type, the **reo** topology. Figure reproduced from Ref. 3.

In this work, we will only discuss the **fcu** topology, as the ideal, defect-free nanocell type, and the **reo** topology, as an example of a defective nanocell type. The simplified atomic structures of these nanocell types are shown in Figure 5.1. By restricting the number of nanocell types, we hope to reduce the complexity of analysing and validating the results of our simulations. Unlike the **bcu** topology, which only contains missing linker defects, the **reo** topology has a large pore, a vacancy left by a missing inorganic cluster. As a consequence, the **reo** topology is known to significantly improve the gas adsorption performance of UiO-66 and is likely of greater value to MOF research than the **bcu** topology. Furthermore, the **reo** topology appears in non-negligible concentrations in synthesised UiO-66 crystals, unlike the **scu** topology, which is mechanically less stable and appears much less frequently.

5.2 Methods

The elastic properties of the **fcu** nanocell of UiO-66(Zr) have been calculated from the trajectory of its cell matrix during an atomistic force field simulation in the (N, P, T) ensemble. The exact procedure has been described in Section 3.3. The same procedure was performed to calculate the elastic properties of the **reo** nanocell. Both atomistic MD simulations were performed with Yaff. The LAMMPS engine was used to simulate all non-covalent interactions. The timestep of the simulation was set to 0.5 fs and the total simulation time reached 5.0 ns. Periodic boundary conditions were used. The thermostat, a Nosé-Hoover chain thermostat with three beads, was set to 300 K and the barostat, a Martyna-Tuckerman-Tobias-Klein barostat, was set to 0 MPa. Both simulations were allowed to equilibrate during 1.0 ns.

The equilibrium cell matrix of the (atomistic) **fcu** nanocell was found to be

$$\mathbf{h}_0(\text{fcu}) = \begin{bmatrix} 21.0 & -0.4 & 0.6 \\ 0.4 & 21.0 & -0.0 \\ -0.6 & 0.0 & 21.0 \end{bmatrix} \text{\AA}, \quad (5.1)$$

and the calculation of the elasticity tensor resulted in

$$\mathbf{C}_0(\text{fcu}) = \begin{bmatrix} 44.5 & 17.8 & 17.5 & 0.2 & -0.3 & 0.1 \\ 17.8 & 42.7 & 19.2 & 0.2 & -0.3 & 0.0 \\ 17.5 & 19.2 & 43.1 & 0.1 & 0.2 & 0.0 \\ 0.2 & 0.2 & 0.1 & 16.7 & -0.2 & 0.5 \\ -0.3 & -0.3 & 0.2 & -0.2 & 16.9 & 0.1 \\ 0.1 & 0.0 & 0.0 & 0.5 & 0.1 & 15.8 \end{bmatrix} \text{GPa}, \quad (5.2)$$

giving rise to the elastic constants tabulated in Table 5.1. The bulk modulus of the **fcu** nanocell can be derived from its elasticity tensor, according to Eq. 3.15, which yields $K(\text{fcu}) = 26.6 \text{ GPa}$.

The equilibrium cell matrix of the (atomistic) **reo** nanocell was found to be

$$\mathbf{h}_0(\text{reo}) = \begin{bmatrix} 21.0 & 0.2 & -0.1 \\ -0.2 & 21.0 & -0.3 \\ 0.1 & 0.3 & 21.0 \end{bmatrix} \text{\AA}, \quad (5.3)$$

and the calculation of the elasticity tensor resulted in

$$\mathbf{C}_0(\text{reo}) = \begin{bmatrix} 22.3 & 8.8 & 8.7 & -0.1 & 0.0 & -0.1 \\ 8.8 & 22.1 & 8.8 & 0.0 & -0.1 & 0.0 \\ 8.7 & 8.8 & 22.1 & 0.0 & 0.0 & 0.0 \\ -0.1 & 0.0 & 0.0 & 8.2 & 0.0 & -0.1 \\ 0.0 & -0.1 & 0.0 & 0.0 & 8.1 & 0.1 \\ -0.1 & 0.0 & 0.0 & -0.1 & 0.1 & 8.4 \end{bmatrix} \text{GPa}, \quad (5.4)$$

giving rise to the elastic constants tabulated in Table 5.2. Like before, the bulk modulus of the **reo** nanocell can be derived from its elasticity tensor, which yields $K(\text{reo}) = 13.2 \text{ GPa}$.

Ideally, for cubic crystal systems such as UiO-66(Zr), the elasticity tensor should only contain three independent elastic constants, represented by C_{11} , C_{12} and C_{44} in Voigt notation. This is approximately true for the results obtained here. To account for the remaining variability, the C_{11} , C_{12} and C_{44} elastic constants reported in Table 5.1 do not represent single elements of the elasticity tensor. Instead, they each represent the mean value of a group of corresponding elements.

The C_{11} , C_{12} and C_{44} constants have been compared with values from literature in an effort to validate the results. The agreement between the simulated values and the values from literature is adequate, though not perfect. Ref. 13 has reported a notably higher C_{44} constant than Ref. 3, likely due to the application of an alternative force field in Ref. 13. The derivation of this alternative force field is explained in detail in Ref. 14.

Component	Simulated	Ref. 3	Ref. 13
C_{11} [GPa]	43.4	59.9	35.0
C_{12} [GPa]	18.2	29.3	14.9
C_{44} [GPa]	16.5	19.9	56.2

Table 5.1: Elastic constants of the **fcu** nanocell, at 300 K and 0 MPa.

Component	Simulated	Ref. 3
C_{11} [GPa]	22.2	28.6
C_{12} [GPa]	8.8	13.1
C_{44} [GPa]	8.2	10.0

Table 5.2: Elastic constants of the **reo** nanocell, at 300 K and 0 MPa

At this point, the parameters of our coarse-grained, micromechanical force field for UiO-66 have been determined: $\mathbf{h}_0(\text{fcu})$, $\mathbf{C}_0(\text{fcu})$, $\mathbf{h}_0(\text{reo})$ and $\mathbf{C}_0(\text{reo})$. The micromechanical force field can now be applied to a micromechanical system, where we specify the exact configuration of **fcu** and **reo** nanocells.

In the context of correlated defects, it is interesting to study how the elastic behaviour of a micromechanical system changes as the concentration and the connectivity of defective nanocells are varied. With the express goal of comparing such configurations, we have performed nine different micromechanical MD simulations. The first simulation handles a homogeneous system, Configuration 0, containing only **fcu** nanocells with identical elastic properties. The other eight simulations are performed with an increasing number of **reo** nanocells, starting from one, over three, to eight and eventually nine, as shown in Figure 5.2. These configurations also have varying degrees of connectivity and correlation. Some create line defects, others defect clusters or defect planes. In fact, it is more difficult to avoid correlation in a periodic $3 \times 3 \times 3$ system than it is to induce correlation.

To perform a micromechanical MD simulation with the newly acquired **fcu** and **reo** nanocell types, one final step remains: the maximal timestep of the simulation must be calculated. The maximal timestep can be obtained by means of a static scan, as described in Section 4.2.1. This results in a maximal timestep of 0.6 ps, but as usual this value was divided by an additional safety factor of ten, to avoid large sampling errors, leading to a final value of 60 fs. For each configuration of Figure 5.2, one million Verlet steps were simulated, reaching a simulation time of 60 ns.

5.3 Results

For each different configuration, the elasticity tensor of the entire micromechanical system was calculated. Unfortunately, the calculation of the elasticity tensors suffers from the same convergence issue

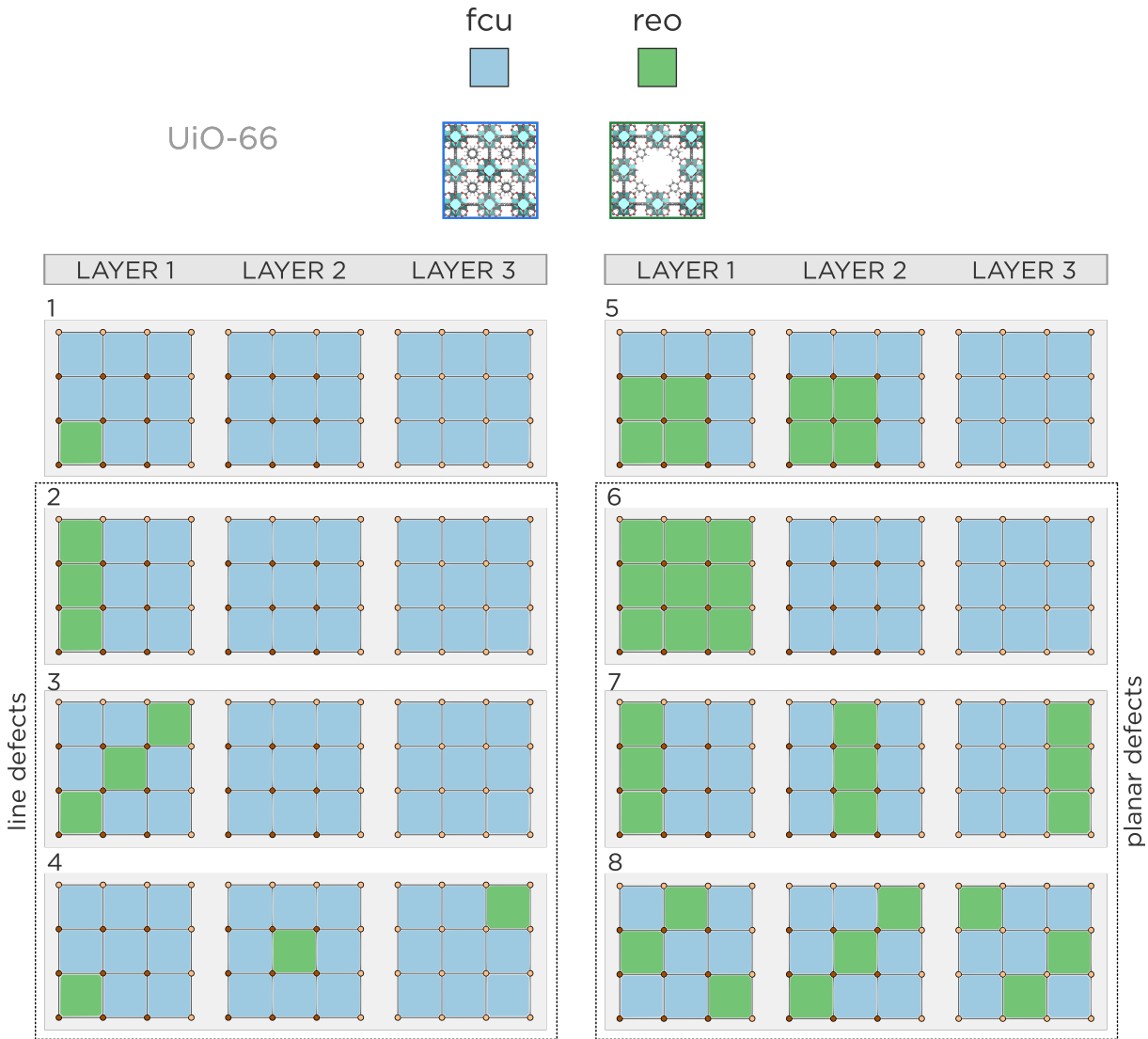


Figure 5.2: Schematic overview of eight different configurations of defective **reo** nanocells surrounded by defect-free **fcu** nanocells. Each configuration is a $3 \times 3 \times 3$ system with periodic boundary conditions. The first, second and third layers of each configuration are spread out next to each other in order of increasing height.

reported in Section 4.2.3. With these results, we cannot expect to provide a semi-quantitative prediction of the mechanical behaviour of a micromechanical system. At best, we can hope to provide a qualitative analysis of the results and to prove their consistency. Configurations 2 to 4, for instance, each represent a differently oriented line defect. Configurations 6 to 8 each represent a differently oriented planar defect. Within these configurations, some similarities should appear.

In order to reduce the complexity of the analysis, the eigenvalues and the bulk moduli of the elasticity tensors have been collected in Table 5.3. The eigenvalues and eigenvectors of the elasticity tensor

represent the strength and orientation of its deformation modes. In Table 5.3, the six eigenvalues of the elasticity tensor have been grouped according to the three deformation modes of a cubic crystal. Note, however, that the distribution of **re_o** nanocells in the **fcu** nanocells breaks the cubic symmetry of the system. The deformation modes of the system still resemble the deformation modes of a cubic crystal, but only approximately. The first eigenvalue, λ_1 , corresponds, approximately, to an isotropic deformation. The following two eigenvalues, λ_{2a} and λ_{2b} , are no longer degenerate, but still correspond, approximately, to tensile deformations. The last three eigenvalues, λ_{3a} , λ_{3b} and λ_{3c} , are no longer degenerate, but still correspond, approximately, to shear deformations.

	K_{scan} [GPa]	K_{MD} [GPa]	λ_1 [GPa]	λ_{2a} [GPa]	λ_{2b} [GPa]	λ_{3a} [GPa]	λ_{3b} [GPa]	λ_{3c} [GPa]
Conf. 0	26.6	62.3	186.9	83.8	83.4	27.0	26.4	26.0
Conf. 1	25.9	63.0	189.0	83.9	74.6	29.0	27.8	26.6
Conf. 2	24.6	62.3	186.9	85.1	75.9	26.7	24.8	23.9
Conf. 3	24.8	62.2	186.7	88.6	73.5	27.7	27.6	24.3
Conf. 4	24.9	60.8	182.3	90.1	79.1	27.7	25.3	23.3
Conf. 5	21.8	53.2	159.6	75.6	73.1	22.3	21.6	21.4
Conf. 6	20.7	50.9	154.9	76.0	63.3	22.3	19.0	18.1
Conf. 7	21.7	54.1	162.3	74.7	72.6	23.3	22.9	21.2
Conf. 8	21.9	53.8	161.5	82.1	71.3	24.6	22.7	21.7

Table 5.3: Derived elastic properties of the homogeneous system (Configuration 0) and of the eight configurations of Figure 5.2 (Configurations 1-8). The (static) bulk modulus K_{scan} was calculated from a relaxed potential energy scan of the micromechanical system. The other elastic properties, including the (dynamic) bulk modulus K_{MD} , were calculated from a micromechanical MD simulation at 300 K and 0 MPa, using a combination of a Langevin thermostat and barostat.

The results listed in Table 5.3 are consistent if we ignore the large discrepancy between the static bulk modulus, calculated by means of a relaxed potential energy scan, and the dynamic bulk modulus, calculated from a micromechanical MD simulation. While some discrepancy between the static bulk modulus and the dynamic bulk modulus is expected, the difference is too large to be ignored. This is a known convergence issue, which has been discussed in Section 4.2.3. Obviously, the static bulk modulus is a more accurate, more reliable estimate. For Configuration 0, it matches the bulk modulus of the **fcu** nanocell exactly.

Otherwise, the results seem to follow logical patterns and trends. For Configurations 2 to 4, corresponding to line defects, the static bulk modulus and the dynamic bulk modulus are nearly constant. Their eigenvalues are also qualitatively similar. Figure 5.2 implies that these line defects are mutually equivalent up to a rotation, as expected. The remaining numerical discrepancy can be explained by

poor convergence in the case of the dynamic bulk modulus and by poor numerical accuracy in the case of the static bulk modulus. However, the discrepancy could also be partially attributed to the cubic nature of the grid of nanocells. In Configuration 2, two neighbouring **reo** nanocells share four nodes. In Configuration 3, they share two nodes. In Configuration 4, they only share one node. These configurations are, as such, not entirely equivalent, due to the discretisation of the grid. For Configurations 6 to 8, corresponding to planar defects, similar conclusions apply.

The eigenvectors of the elasticity tensor, when they are not written in Voigt notation, are 3×3 strain tensors. When the eigenvectors are multiplied with their eigenvalues, they become stress tensors. A strain or stress tensor can be decomposed into its own eigenvalues. The eigenvalues of the stress tensor are also known as the principal stresses and its eigenvectors are known as (the normal vectors of) the principal planes [39]. We have performed such a decomposition into principal stresses for the first deformation mode of the elasticity tensor, which is, approximately, an isotropic deformation mode. In mathematical terms, we have performed the following eigenvalue decompositions,

$$\begin{aligned} \text{STEP 1} \quad & \mathbf{C}_0(\text{system}) : \boldsymbol{\varepsilon}_1 = \lambda_1 \boldsymbol{\varepsilon}_1 (= \boldsymbol{\sigma}_1) \\ \text{STEP 2} \quad & \boldsymbol{\sigma}_1 \mathbf{n} = s \mathbf{n}, \end{aligned} \tag{5.5}$$

where the 3×3 strain tensor $\boldsymbol{\varepsilon}_1$ represents the first deformation mode, s is one of the principal stresses of the 3×3 stress tensor $\boldsymbol{\sigma}_1$ and \mathbf{n} is the corresponding principal plane. To put it simply, we have investigated which spatial directions experience the highest amount of stress when the system is being, approximately, isotropically compressed or expanded.

Configuration 6 is an example for which this procedure results in a simple, qualitative conclusion.

Configuration 6

$$\begin{aligned} s_1 = 100.9 \text{ GPa} \quad & \mathbf{n}_1 \approx \begin{bmatrix} 1 \\ 0 \\ 0 \end{bmatrix} \\ s_2 = 69.1 \text{ GPa} \quad & \mathbf{n}_2 \approx \begin{bmatrix} 0 \\ 0 \\ 1 \end{bmatrix} \\ s_3 = 95.0 \text{ GPa} \quad & \mathbf{n}_3 \approx \begin{bmatrix} 0 \\ 1 \\ 0 \end{bmatrix} \end{aligned} \tag{5.6}$$

In Configuration 6, the weakest principal stress, s_2 , is applied along the z -axis. This result is in line with our expectations, because the z -axis is perpendicular to the plane of **reo** nanocells in Configuration 6. The bottom layer of **reo** nanocells creates a flexible link when the material is being stretched along the z -axis, reducing the amount of stress in that direction.

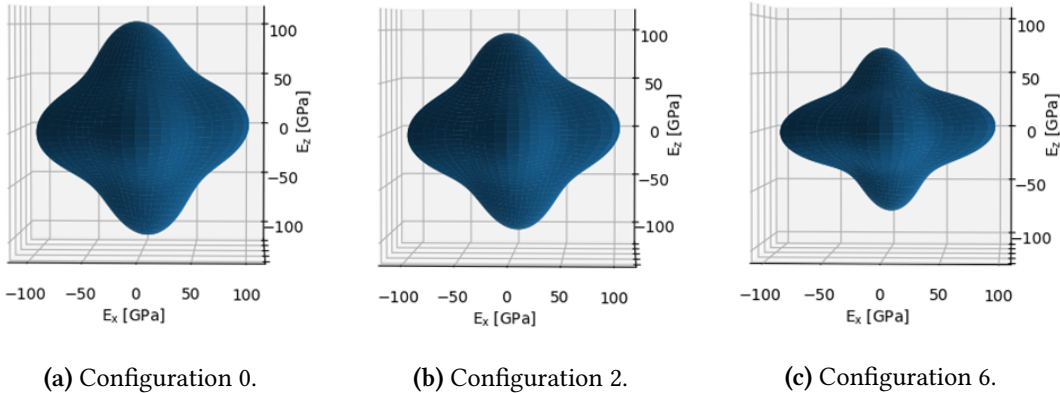


Figure 5.3: Directional Young moduli for three different configurations of Figure 5.2.

Configuration 2 is another example that yields a simple conclusion.

$$\begin{aligned}
 \text{Configuration 2} \\
 s_1 = 111.2 \text{ GPa} & \quad \mathbf{n}_1 \approx \begin{bmatrix} 1 \\ 0 \\ 0 \end{bmatrix} \\
 s_2 = 105.8 \text{ GPa} & \quad \mathbf{n}_2 \approx \frac{\sqrt{2}}{2} \begin{bmatrix} 0 \\ -1 \\ 1 \end{bmatrix} \\
 s_3 = 106.6 \text{ GPa} & \quad \mathbf{n}_3 \approx \frac{\sqrt{2}}{2} \begin{bmatrix} 0 \\ 1 \\ 1 \end{bmatrix}
 \end{aligned} \tag{5.7}$$

The strongest principal stress, s_1 , is applied along the x -axis, parallel to the line of **reo** nanocells in Configuration 2. The other principal stress is approximately twofold degenerate and slightly weaker. The effect is clearly not as strong for a line of defects (Configuration 2) as for a plane of defects (Configuration 6).

The directional Young modulus, which has been introduced in Section 3.3, can be derived from the elasticity tensor according to Eq. 3.16. A three-dimensional visualisation of the directional Young modulus reveals the directions for which a nanocell is most flexible and most rigid under a tensile deformation. In Figure 5.3, the directional Young moduli of Configuration 0, Configuration 2 and Configuration 6 have been plotted. For all three configurations, a deformation along the x -axis yields a similar result. Along the z -axis, Configuration 2 is slightly more flexible than Configuration 0, due to the line defect. Configuration 6 is the most flexible of the three configurations along the z -axis, due to the planar defect.

5.4 Conclusions

A micromechanical MD simulation of a $3 \times 3 \times 3$ UiO-66 system in the (N, P, T) ensemble does not yield an accurate elasticity tensor. The elasticity tensor of a homogeneous system of exclusively **fcu** nanocells, for instance, does not match the elasticity tensor of the **fcu** nanocell type. This issue has been previously reported in Section 4.2.3. Nevertheless, the bulk modulus and the eigenvalues and eigenvectors derived from the elasticity tensor provide useful, albeit qualitative, information. The eigenvectors of the elasticity tensor are the elastic deformation modes of the micromechanical system. The stress tensors of these deformation modes can be further decomposed into their own eigenvalues, the principal stresses, and their own eigenvectors, the principal planes.

The bulk modulus of a micromechanical system can also be calculated by means of a relaxed scan, which does yield accurate and consistent results. For quantitative conclusions about UiO-66, we turn to these results, as they lie closer to the bulk modulus of the atomistic **fcu** nanocell. Firstly, a significant concentration of **reo** nanocells, e.g., one third of the total amount of nanocells, can lower the bulk modulus of the system by more than 20%. Secondly, the orientation of a line defect or a planar defect has an effect on the bulk modulus, due to the discretisation of the nanocell grid and the varying connectivity between **reo** nanocells, although the effect is observed to be rather small.

6

Conclusions and outlook

We conclude this work with a discussion of the obtained results and a few suggestions for future research. These suggestions include improvements of and additions to the micromechanical model, as well as simulations that were proposed, but have not been performed. In order tie our conclusions to the larger context of this work, we have provided short summaries of the previous chapters.

Chapter 1 began with a general introduction to MOFs and their applications. UiO-66, HKUST-1 and MIL-53 were highlighted as examples of MOFs containing correlated spatial disorder. Additionally, the concept of molecular modelling and its most popular computational methods were briefly explained. Chapter 2 provided an overview of coarse-grained force fields and two examples of a MOF being coarse-grained. A few general properties of coarse-grained force fields were revealed. In Chapter 3, the micromechanical model was explained in detail. The reader was familiarised with the concept of nanocell types, with the parameters of the model, with the advantages and limitations of the model and with the micromechanical equations of motion. Chapter 4 began with a description of MicMec, our implementation of the micromechanical model. The remainder of Chapter 4 was dedicated to validating the micromechanical model by means of a test system. Chapter 5 centred around the case study of correlated defects in UiO-66. A qualitatively analysis of eight different configurations of defective **re**o nanocells, surrounded by **fcu** nanocells, was performed.

We can summarise the four milestones of this work as follows.

1. The micromechanical model has been implemented and is available as a Python package named MicMec. The micromechanical equations of motion were modified from their original formulation in Ref. 29 and have been derived correctly. The analytically derived forces match the negative numerical derivatives of the total potential energy.
2. A micromechanical MD simulation in the (N, V, E) ensemble conserves the total energy of the system, as it should. In the (N, V, T) ensemble, temperature is controlled adequately. In the (N, P, T) ensemble, both pressure and temperature are controlled adequately.
3. A relaxed scan of a homogeneous system, *i.e.*, containing only a single nanocell type, is able to produce the static bulk modulus of the system. Independently of the size of the system, the obtained bulk modulus matches the bulk modulus of its constituent nanocells, within the numerical accuracy of the relaxed scan. Therefore, a relaxed scan of a heterogeneous system, *i.e.*, containing different nanocell types, should produce an accurate estimate of the bulk modulus of the entire system as well. The validity of this result depends on (i) the atomic structure of the heterogeneous system and (ii) the validity of the elastic properties of the nanocells. Like other coarse-grained force fields, the results of the micromechanical model can only be as accurate as its parameters, which have been obtained from a higher level of theory.
4. Semi-quantitative and qualitative results of the micromechanical model have been reported for a case study of defective nanocells in UiO-66. The static and dynamic bulk modulus, the directional Young modulus and the principal stresses of the first deformation mode of a micromechanical UiO-66 system were all observed to vary as a function of defect concentration and correlation.

Despite these milestones, several improvements can be made to the current implementation of the micromechanical model.

First and foremost, a consistent validation strategy dictates that the elasticity tensor of a homogeneous micromechanical system should converge to the elasticity tensor of its constituent nanocells. In Section 4.2.3, we have attempted to demonstrate this convergence by performing an MD simulation of a homogeneous test system in the (N, P, T) ensemble, without success. In Section 5.3, we have tried this again, by performing an MD simulation of a homogeneous UiO-66 system, also in the (N, P, T) ensemble, again without success. A thorough investigation should be conducted to determine the cause of this convergence issue. To be precise, it must be explained (i) why a combination of a stochastic thermostat and barostat yields a different elasticity tensor than a combination of a deterministic thermostat and barostat (Section 4.2.3) and (ii) why the elasticity tensor of the system, in both cases, does not converge to its intended value (Section 4.2.3 and Section 5.3). This issue is likely related to either the calculation of the virial tensor of the simulation domain or to the implementation of the barostats.

Secondly, The alternative method to calculate the forces acting on a node, proposed at the end of Section 4.2.1, should be implemented. It is likely superior to the currently implemented method. It should be noted that this alternative method does not solve the aforementioned convergence issue.

Thirdly, the analytical expressions for the forces acting on a micromechanical node are not trivial to derive. While it is possible to extend the micromechanical model with anharmonic contributions, the implementation of the model grows more cumbersome with each extension of the model. Calculating, analytically, the gradient of the total potential energy is an especially difficult step. The gradient, however, can also be calculated by means of automatic differentiation. Automatic differentiation is mainly used in machine learning research and is implemented in, for instance, the Python package JAX. For us, it could make the process of defining a new potential energy much easier, as the gradient of the new potential energy can be calculated automatically. For the time being, we have decided against using automatic differentiation, to avoid creating a black box and in order to maintain control over the finer details of the implementation. Future versions of MicMec could use JAX for automatic differentiation.

Fourthly, the calculation of the forces acting on the micromechanical nodes is parallelisable. Parallel computation on a CPU or GPU could massively improve the time spent on a micromechanical MD simulation. In the current version of MicMec, one Verlet step of an MD simulation in the (N, P, T) ensemble takes approximately 4.20 ms per micromechanical node.

Lastly, many more experiments can be performed with the micromechanical model.

1. A simulation of a MOF with bistable nanocells, *e.g.*, MIL-53, can be performed. It is possible to construct an arbitrary phase boundary as part of the initial state of the micromechanical system, or to let the system evolve spontaneously from one phase. MicMec supports the inclusion of unistable and bistable nanocells, as well as the inclusion of nanocells with more than two metastable states.
2. It is also possible to perform a simulation of a MOF with mesopores, *e.g.*, HKUST-1. Mesoporosity can be mimicked by the inclusion of empty nanocells in the grid of the micromechanical system. MicMec supports the inclusion of empty nanocells.
3. Aside from the mechanical properties of a micromechanical system, its thermal properties can be investigated as well. The heat capacity and the thermal expansion coefficient, for instance, can be extracted from MD simulations.

We hope that these future experiments will prove the effectiveness of the micromechanical model and its broad applicability. It must be emphasised that the model, as a qualitative or semi-quantitative method to simulate MOFs, has been tested and validated. Unfortunately, the current implementation of the model is plagued by a well-documented convergence issue, which we have not been able to solve. Future research is needed to validate the model more thoroughly, even beyond fixing this convergence issue. Eventually, the model should be compared directly to other coarse-grained force fields, as those are the only methods, besides experiments on synthesised MOFs, that reach the same length scales as the micromechanical model.

References

- [1] H.-C. Zhou, J. R. Long, and O. M. Yaghi, “Introduction to metal–organic frameworks,” *Chem. Rev.*, vol. 112, pp. 673–674, 2012.
- [2] V. Van Speybroeck, S. Vandenhaute, A. E. Hoffman, and S. M. J. Rogge, “Towards modeling spatiotemporal processes in metal–organic frameworks,” *Trends Chem.*, vol. 3, pp. 605–619, 2021.
- [3] M. J. Cliffe, W. Wan, X. Zou, P. A. Chater, A. K. Kleppe, M. G. Tucker, H. Wilhelm, N. P. Funnell, F.-X. Coudert, and A. L. Goodwin, “Correlated defect nano-regions in a metal–organic framework,” *Nat. Commun.*, vol. 5, p. 4176, 2014.
- [4] A. S. Rosen, S. M. Iyer, D. Ray, Z. Yao, A. Aspuru-Guzik, L. Gagliardi, J. M. Notestein, and R. Q. Snurr, “Machine learning the quantum-chemical properties of metal–organic frameworks for accelerated materials discovery,” *Matter*, vol. 4, pp. 1578–1597, 2021.
- [5] L. Öhrström, “Let’s talk about MOFs – topology and terminology of metal-organic frameworks and why we need them,” *Crystals*, vol. 5, pp. 154–162, 2015.
- [6] S. M. J. Rogge, A. Bavykina, J. Hajek, H. Garcia, A. I. Olivos-Suarez, A. Sepúlveda-Escribano, A. Vimont, G. Clet, P. Bazin, F. Kapteijn, M. Daturi, E. V. Ramos-Fernandez, F. X. Llabrés i Xamena, V. Van Speybroeck, and J. Gascon, “Metal–organic and covalent organic frameworks as single-site catalysts,” *Chem. Soc. Rev.*, vol. 46, pp. 3134–3184, 2017.
- [7] K. Sumida, D. L. Rogow, J. A. Mason, T. M. McDonald, E. D. Bloch, Z. R. Herm, T.-H. Bae, and J. R. Long, “Carbon dioxide capture in metal–organic frameworks,” *Chem. Rev.*, vol. 112, pp. 724–781, 2012.
- [8] L. Guo, J. Du, C. Li, G. He, and Y. Xiao, “Facile synthesis of hierarchical micro-mesoporous HKUST-1 by a mixed-linker defect strategy for enhanced adsorptive removal of benzothiophene from fuel,” *Fuel*, vol. 300, p. 120955, 2021.
- [9] V. Bakuru, S. R., S. Maradur, and S. Kalidindi, “Exploring the brønsted acidity of UiO-66 (Zr, Ce, Hf) metal-organic frameworks for efficient solketal synthesis from glycerol acetalization,” *Dalton Trans.*, vol. 48, 2018.

- [10] H. Wu, Y. S. Chua, V. Krungleviciute, M. Tyagi, P. Chen, T. Yildirim, and W. Zhou, “Unusual and highly tunable missing-linker defects in zirconium metal–organic framework UiO-66 and their important effects on gas adsorption,” *J. Am. Chem. Soc.*, vol. 135, no. 28, pp. 10 525–10 532, 2013.
- [11] J. Dürholt, R. Galvelis, and R. Schmid, “Coarse graining of force fields for metal–organic frameworks,” *Dalton Trans.*, vol. 45, p. 4370–4379, 2015.
- [12] C. Wang, D. Liu, and W. Lin, “Metal–organic frameworks as a tunable platform for designing functional molecular materials,” *J. Am. Chem. Soc.*, vol. 135, pp. 13 222–13 234, 2013.
- [13] S. M. J. Rogge, M. Waroquier, and V. Van Speybroeck, “Reliably modeling the mechanical stability of rigid and flexible metal–organic frameworks,” *Acc. Chem. Res.*, vol. 51, pp. 138–148, 2018.
- [14] S. M. J. Rogge, J. Wieme, L. Vanduyfhuys, S. Vandenbrande, G. Maurin, T. Verstraelen, M. Waroquier, and V. Van Speybroeck, “Thermodynamic insight in the high-pressure behavior of UiO-66: Effect of linker defects and linker expansion,” *Chem. Mater.*, vol. 28, pp. 5721–5732, 2016.
- [15] Z. Fang, B. Bueken, D. De Vos, and R. Fischer, “Defect-engineered metal–organic frameworks,” *Angew. Chem. Int. Ed.*, vol. 54, p. 7234 –7254, 2015.
- [16] D. Johnstone, F. Firth, C. Grey, P. Midgley, M. Cliffe, and S. Collins, “Direct imaging of correlated defect nanodomains in a metal–organic framework,” *J. Am. Chem. Soc.*, vol. 142, p. 13081–13089, 2020.
- [17] A. Ortiz, A. Boutin, A. Fuchs, and F.-X. Coudert, “Anisotropic elastic properties of flexible metal–organic frameworks: How soft are soft porous crystals?” *Phys. Rev. Lett.*, vol. 109, p. 195502, 2012.
- [18] L. Liu, Z. Chen, J. Wang, D. Zhang, Y. Zhu, S. Ling, K.-W. Huang, Y. Belmabkhout, K. Adil, Y. Zhang, B. Slater, M. Eddaoudi, and Y. Han, “Imaging defects and their evolution in a metal–organic framework at sub-unit-cell resolution,” *Nat. Chem.*, vol. 11, p. 1, 2019.
- [19] E. Meekel and A. Goodwin, “Correlated disorder in metal–organic frameworks,” *CrystEngComm*, vol. 23, p. 2915–2922, 2021.
- [20] L. Liu, D. Zhang, Y. Zhu, and Y. Han, “Bulk and local structures of metal–organic frameworks unravelled by high-resolution electron microscopy,” *Commun. Chem.*, vol. 3, pp. 1–14, 2020.
- [21] R. Ameloot, F. Vermoortele, J. Hofkens, F. De Schryver, D. De Vos, and M. Roeffaers, “Three-dimensional visualization of defects formed during the synthesis of metal–organic frameworks: A fluorescence microscopy study,” *Angew. Chem. Int. Ed.*, vol. 52, 2013.
- [22] S. M. J. Rogge, M. Waroquier, and V. Van Speybroeck, “Unraveling the thermodynamic criteria for size-dependent spontaneous phase separation in soft porous crystals,” *Nat. Commun.*, vol. 10, p. 4842, 2019.

- [23] Y. Liu, J.-H. Her, A. Dailly, A. J. Ramirez-Cuesta, D. A. Neumann, and C. M. Brown, “Reversible structural transition in MIL-53 with large temperature hysteresis,” *J. Am. Chem. Soc.*, vol. 130, pp. 11 813–11 818, 2008.
- [24] R. Iftimie, P. Minary, and M. E. Tuckerman, “Ab initio molecular dynamics: Concepts, recent developments, and future trends,” *Proc. Natl. Acad. Sci.*, vol. 102, pp. 6654–6659, 2005.
- [25] D. Frenkel and B. Smit, *Understanding Molecular Simulation: From algorithms to applications*, 2nd ed. San Diego: Academic Press, 2002.
- [26] X. He and K. M. Merz, “Divide and conquer Hartree–Fock calculations on proteins,” *J. Chem. Theory Comput.*, vol. 6, pp. 405–411, 2010.
- [27] L. Vanduyfhuys, S. Vandenbrande, T. Verstraelen, R. Schmid, M. Waroquier, and V. Van Speybroeck, “QuickFF: A program for a quick and easy derivation of force fields for metal-organic frameworks from *Ab Initio* input,” *J. Comput. Chem.*, vol. 36, p. 1015– 1027, 2015.
- [28] J. Heinen, N. C. Burtch, K. S. Walton, and D. Dubbeldam, “Flexible force field parameterization through fitting on the ab initio-derived elastic tensor,” *J. Chem. Theory Comput.*, vol. 13, pp. 3722–3730, 2017.
- [29] S. M. J. Rogge, “The micromechanical model to computationally investigate cooperative and correlated phenomena in metal-organic frameworks,” *Faraday Discuss.*, vol. 225, pp. 271–285, 2020.
- [30] S. Cranford and M. Buehler, “Coarse-graining parameterization and multiscale simulation of hierarchical systems,” in *Multiscale modeling: From atoms to devices*, 1st ed., P. Derosa and T. Cagin, Eds. Boca Raton: CRC Press, 2010, ch. 2, pp. 13–34.
- [31] W. Noid, J.-W. Chu, G. Ayton, S. Izvekov, G. Voth, A. Das, and H. Andersen, “The multiscale coarse-graining method. I. A rigorous bridge between atomistic and coarse-grained models,” *J. Chem. Phys.*, vol. 128, p. 244114, 2008.
- [32] S. J. Marrink, H. J. Risselada, S. Yefimov, D. P. Tieleman, and A. H. de Vries, “The MARTINI force field: Coarse grained model for biomolecular simulations,” *J. Phys. Chem. B*, vol. 111, pp. 7812–7824, 2007.
- [33] S. Kmiecik, D. Gront, M. Kolinski, L. Wieteska, A. E. Dawid, and A. Kolinski, “Coarse-grained protein models and their applications,” *Chem. Rev.*, vol. 116, pp. 7898–7936, 2016.
- [34] A. Lyubartsev and A. Laaksonen, “Calculation of effective interaction potentials from radial-distribution functions - a reverse Monte-Carlo approach,” *Phys. Rev. E*, vol. 52, pp. 3730–3737, 1995.
- [35] T. Moore, C. Iacovella, and C. Mccabe, “Derivation of coarse-grained potentials via multistate iterative Boltzmann inversion,” *J. Chem. Phys.*, vol. 140, p. 224104, 2014.

- [36] L. Lu, J. Dama, and G. Voth, “Fitting coarse-grained distribution functions through an iterative force-matching method,” *J. Chem. Phys.*, vol. 139, p. 121906, 2013.
- [37] M. Shell, “The relative entropy is fundamental to multiscale and inverse thermodynamic problems,” *J. Chem. Phys.*, vol. 129, p. 144108, 2008.
- [38] R. Semino, J. Dürholt, R. Schmid, and G. Maurin, “Multiscale modeling of the HKUST-1/poly(vinyl alcohol) interface: From an atomistic to a coarse graining approach,” *J. Phys. Chem.*, vol. 121, pp. 21 491–21 496, 2017.
- [39] M. Kachanov and I. Sevostianov, *Background Results on Elasticity and Conductivity*. Springer International Publishing, 2018, pp. 1–88.
- [40] C. D. Christ and W. F. van Gunsteren, “Enveloping distribution sampling: A method to calculate free energy differences from a single simulation,” *J. Chem. Phys.*, vol. 126, p. 184110, 2007.
- [41] J. Vandewalle, “MicMec, the micromechanical model.” [Online]. Available: <https://github.com/Jlvdwall/micmec>
- [42] T. Verstraelen, L. Vanduyfhuys, S. Vandenbrande, and S. M. J. Rogge, “Yaff, yet another force field.” [Online]. Available: <http://molmod.ugent.be/software/>
- [43] A. Thompson, S. Plimpton, and W. Mattson, “General formulation of pressure and stress tensor for arbitrary many-body interaction potentials under periodic boundary conditions,” *J. Chem. Phys.*, vol. 131, p. 154107, 2009.